

# UC Berkeley

## UC Berkeley Electronic Theses and Dissertations

**Title**

Two-Dimensional Electronic-Vibrational Spectroscopy

**Permalink**

<https://escholarship.org/uc/item/3np6394x>

**Author**

Lewis, Nicholas Henry Cohen

**Publication Date**

2016

Peer reviewed|Thesis/dissertation

# Two-Dimensional Electronic-Vibrational Spectroscopy

by

Nicholas Henry Cohen Lewis

A dissertation submitted in partial satisfaction of the

requirements for the degree of

Doctor of Philosophy

in

Chemistry

in the

Graduate Division

of the

University of California, Berkeley

Committee in charge:

Professor Graham R. Fleming, Chair

Professor Stephen R. Leone

Professor Krishna K. Niyogi

Fall 2016

# **Two-Dimensional Electronic-Vibrational Spectroscopy**

Copyright 2016  
by  
Nicholas Henry Cohen Lewis

## Abstract

### Two-Dimensional Electronic-Vibrational Spectroscopy

by

Nicholas Henry Cohen Lewis

Doctor of Philosophy in Chemistry

University of California, Berkeley

Professor Graham R. Fleming, Chair

This dissertation describes the development and initial applications of Two-Dimensional Electronic-Vibrational spectroscopy (2DEV), a multidimensional ultrafast spectroscopic technique that is capable of directly probing the coupling between electronic and vibrational transitions in molecular species.

This thesis first provides the necessary background and motivation driving the development of this spectroscopy, discussing the role of electronic-vibrational coupling in small molecule photophysics and the ways we can take advantage of these physics to study electronic excitation transfer in photosynthetic light harvesting systems. It then discusses the details of the apparatus constructed to perform the 2DEV experiments, as well as some of the important aspects of the signal processing and extraction of the desired signal, using phase cycling techniques. It goes on to describe the development of a simple model to be used in understanding the new information content accessible with 2DEV, and presents experimental results from the laser dye DTTCl. The basic predictions of the model, such as the dynamics of the spectral lineshape, are shown to hold in these experimental results, and we provide an experimental measurement for the difference in the strength of the vibration-bath coupling between the electronic ground and excited states.

In chapter 4, the model is extended to the case of an electronically coupled dimer, and a method is proposed by which 2DEV could potentially be used to study the movement of electronic excitations through a molecular aggregate, such as a photosynthetic light harvesting complex. It is shown how it might be possible to measure the electronic excited state populations directly in the site basis, without the need for an accompanying model. To demonstrate an experimental implementation of this method, the 2DEV spectra of Chlorophyll *a* and *b* in solution are then presented, assigning the important spectral features and demonstrating conclusively the connection between spectral shifts along the electronic and vibrational axes due to changes in the axial coordination state of the central Mg. This is a first step which is then expanded upon with the demonstration of the experimental application of 2DEV to the major light harvesting complex in plants, LHCII, and an illustration that the technique proposed in chapter 4 is technically sound. Indications are observed of long lived population



of Chl *b* which contradicts the predictions of current models for the excitonic structure of this system, and calls into question our current understanding of the initial energy transfer dynamics in plant photosynthesis.

Finally, a discussion is provided of some of the promising directions for 2DEV to be further developed in the future.

For my family.

# Contents

<b>Contents</b>	<b>ii</b>
<b>List of Figures</b>	<b>iv</b>
<b>List of Tables</b>	<b>xi</b>
<b>1 Introduction</b>	<b>1</b>
<b>2 Two-Dimensional Electronic-Vibrational Spectrometer</b>	<b>9</b>
2.1 Introduction . . . . .	9
2.2 Experimental Design . . . . .	9
2.3 Visible Pulse Generation . . . . .	11
2.4 Signal Extraction . . . . .	14
<b>3 Measuring Correlated Electronic and Vibrational Spectral Dynamics Using Line Shapes</b>	<b>18</b>
3.1 Introduction . . . . .	18
3.2 Theoretical . . . . .	20
3.3 Experimental . . . . .	29
3.4 Conclusion . . . . .	35
<b>4 A Method for the Direct Measurement of Electronic Site Populations in a Molecular Aggregate</b>	<b>36</b>
4.1 Introduction . . . . .	36
4.2 Model . . . . .	38
4.3 Simulation Results . . . . .	46
4.4 Measurement of Electronic Site Populations . . . . .	48
4.5 Conclusion . . . . .	52
4.6 Derivation of the Dimer Response Functions . . . . .	54
4.7 Equivalence with Secular Redfield . . . . .	57
<b>5 Two-Dimensional Electronic-Vibrational Spectroscopy of Chlorophyll <i>a</i> and <i>b</i></b>	<b>59</b>

5.1	Introduction . . . . .	59
5.2	Results and Discussion . . . . .	61
5.3	Conclusion . . . . .	67
5.4	Methods . . . . .	68
<b>6</b>	<b>Spatio-Energetic Dynamics in Light Harvesting Complex II</b>	<b>72</b>
6.1	Introduction . . . . .	72
6.2	Results and Discussion . . . . .	75
6.3	Conclusion . . . . .	84
6.4	Experimental Methods . . . . .	85
<b>7</b>	<b>Future Directions for Two-Dimensional Electronic-Vibrational Spectroscopy</b>	<b>86</b>
7.1	Introduction . . . . .	86
7.2	Wavepacket Dynamics and Conical Intersections . . . . .	86
7.3	Coherent Excitation Transfer . . . . .	97
	<b>Bibliography</b>	<b>100</b>

# List of Figures

1.1	Schematic representations of the typical physical pictures of electronic-vibrational coupling mechanisms. A) A single coordinate picture depicting the strongest mechanisms of coupling, the displacement of the equilibrium coordinate $\Delta Q$ and the change in the vibrational frequency $\Delta\omega$ between the ground and excited electronic states. B) An extension of this picture to multiple coordinates, where anharmonic coupling $\Delta_{12}$ between vibrational modes can induce a coupling to the electronic transition in an otherwise inactive mode. . . . .	2
1.2	Structure for the dye molecule DCM used in the initial demonstration of 2DEV (top) together with the two models for the initial excited state evolution for this molecule (bottom). . . . .	4
1.3	A series of 2DEV spectra of DCM in DMSO at different waiting times $t_2$ . The positive (yellow-red) bands are due to vibrational modes on the electronic ground state, while the negative (green-blue) bands are due to vibrational modes on the electronic excited state. The dashed box marks the initial position of the main band of interest, illustrating the simultaneous blue shift of the vibrational frequency with the red shift of the electronic excitation frequency. . . . .	5
2.1	Schematic of the 2DEV experimental setup. The visible pump beam is shown in red, and the IR probe beam is shown in purple. The $t_1$ time delay and $\phi_{12}$ relative phase difference between the pump pulse pair is generated and controlled by the pulse shaper (Dazzler), while the $t_2$ time delay between the pump and the probe is controlled with the delay stage. A reference beam (dashed purple line) follows next to the probe beam through the sample and is imaged onto a second array in the detector. The signal is self heterodyned by the collinear probe beam. The relative polarization between the pump and the probe are determined by the half wave plate in the pump beam before the focusing OAP. . . . .	10

2.2	Schematic of the NOPA with pulse-front-tilt matching between the pump and the seed. $\lambda/2$ : half wave plate, BS: 2% reflective beam splitter, BBO1: $\beta$ -BBO for 800 SHG, $\theta = 29.2^\circ$ , $\phi = 90^\circ$ , 1mm thick, DM: dichroic mirror, reflect 400nm, transmit 800nm, P: $90^\circ$ fused silica prism, LP: fused silica lens $f = 20\text{cm}$ , 400nm AR coating, VND: variable neutral density filter, Iris: adjustable aperture, LS: BK7 lens $f = 15\text{cm}$ , 650 – 1050nm AR coating, Saph: 3mm thick sapphire plate, uncoated, OAP: silver coated $90^\circ$ off axis parabolic mirror, $f = 2.5\text{cm}$ , SM: silver coated spherical mirror, $f = 25\text{cm}$ , BBO2: $\beta$ -BBO for amplification, $\theta = 29.2^\circ$ , $\phi = 90^\circ$ , 2mm thick. . . . .	11
2.3	Typical spectrum of the NOPA signal optimized for the center of the tuning range.	12
2.4	Two photon absorption strength as a function of second order dispersion applied by the pulse shaper (top) and the accurately measured temporal profile and the FTL for the visible pulse using SRSI (bottom). The measured FWHM is 15.3 fs, as compared to the FTL 14.3 fs. . . . .	13
2.5	Comparison between theoretical (left) and experimental (right) interference patterns between the pump pulse pair as a function of delay time for relative phases $\Delta\phi = 0, \pi/2, \pi$ and $3\pi/2$ . . . . .	16
3.1	a) A schematic representation of the energy level structure of the hamiltonian. The states are labeled with the electronic state and the number of quanta in the vibration (here we will only allow $v = 0$ or $1$ ). The double-headed arrows represent the bath induced fluctuations and are labeled with the line shape functions that describe how the states fluctuate relative to $ g0\rangle$ due to system-bath interactions. b) Double sided Feynman diagrams for the pathways considered in this work. The red arrows represent interactions resonant with visible photons and the black arrows represent interactions with infrared photons. The labels represent the rephasing ( $R^R$ ) and nonrephasing ( $R^{NR}$ ) pathways, evolving on the ground ( $R_g$ ) or excited ( $R_e$ ) electronic state during $t_2$ . . . . .	21
3.2	Simulated purely absorptive 2DEV spectra using the exact response functions in equation (3.3) with the center lines superimposed. The positive-going (red) features correspond to the vibration on the electronic ground state and the negative-going (blue) features correspond to the vibration on the electronic excited state. The details of this simulation are given in the text. . . . .	23
3.3	The center-line slope of the ground state feature for the model shown in Figure (3.2). The solid blue line shows the analytical result from equation (3.15), the green crosses show the result for the calculation with the short-time approximation without the further approximation in equation (3.9) and the red circles show the result for the calculation using the exact response functions in equation (3.3). The small discrepancy between the exact result and the analytical result comes from the relatively long vibrational dephasing and the short-time approximation. The discrepancy decreases as $\lambda_v$ is increased. . . . .	28

- 3.4 (a-b) The linear absorption of DTTCl dissolved in  $\text{CDCl}_3$  at the concentration used in the present experiment is shown in blue. The electronic absorption is shown in a) and the vibrational absorption, with the solvent signal subtracted, is shown in b). In each case the normalized laser spectrum used to excite the relevant transition superimposed in black. c) Stick spectra of the calculated normal mode frequencies and infrared intensities within the probed region calculated for the  $S_0$  (blue) and  $S_1$  (red) electronic states. Note the axes for the two sets of data differ by a factor of 50. In each case the frequencies have been scaled by a factor of 0.98.[4] The details of the calculation are given in the text. . . . . 30
- 3.5 a) A purely absorptive 2DEV spectrum of DTTCl at  $t_2 = 0$  ps. The dotted line indicates the slice through the spectrum shown as a function of  $t_2$  in b). For  $t_2 > 0$  the signal at  $\omega_3 = 1400 \text{ cm}^{-1}$  decays with a time constant of  $\sim 250$  ps. For  $t_2 < 0$  it decays with a time constant of 1.5 ps. . . . . 31
- 3.6 a) Purely absorptive 2DEV spectra of the  $1400 \text{ cm}^{-1}$  mode of DTTCl in  $\text{CDCl}_3$  at waiting times  $t_2 = 0, 1$  and 5 ps. The center line with respect to  $\omega_3$  is indicated by the solid lines and the center line with respect to  $\omega_1$  is indicated with dashed lines. b) The center line slope with respect to  $\omega_3$ ,  $k_g(t_2)$ , as a function of the waiting time  $t_2$ . The solid red line is the fit of the data to a single exponential, with a lifetime of  $\tau = 1.8$  ps. c) The center line slope with respect to  $\omega_1$ ,  $k'_g(t_2)$ , as a function of the waiting time  $t_2$ . The solid red line is the fit of the data to a single exponential, with a lifetime of  $\tau = 1.6$  ps and an amplitude of  $k'_g(0) = 1.5$ . 33
- 4.1 A schematic illustration of the model used in this work (energies are not drawn to scale). The electronic ground state is indicated by green for monomer  $A$  and yellow for monomer  $B$ , whereas the electronic excited state is indicated by blue and red, respectively. Solid lines indicate the vibration is on the ground state, while dashed lines indicate the vibration is excited. Note that when one of the excitons is populated, a vibrational excitation can occur with that monomer on either the ground or excited electronic state. . . . . 39

4.2	The rephasing Liouville pathways considered in this work (right), and a schematic representation of the resulting spectrum (left). The pathways that evolve on the electronic ground state are labelled as $R_{\alpha M}$ to indicate that exciton $ \alpha\rangle$ is excited, and the vibration on site $M$ is probed, while those on the electronic excited state are labelled as $R_{\alpha\beta M'}$ , to indicate the population is transferred from exciton $ \alpha\rangle$ to exciton $ \beta\rangle$ during $t_2$ and that the vibration on site $M$ is probed. The interactions with the visible laser are indicated by red arrows while the interactions with the infrared laser are indicated by black arrows, and the emission of the infrared signals are indicated by the black dashed arrows. Within the current approximations, the pathways that evolve on the electronic ground state during $t_2$ have positive contributions (solid red lines), while the pathways that evolve on an electronic excited state make negative contributions (dashed blue lines). The plus and minus signs are present to emphasize the sign of each contribution to the total response. The time variables $\{\tau_i\}$ are used to describe the details of the trajectory on the electronic excited state. . . . .	43
4.3	2DEV spectra for an electronic coupling of $J = -50 \text{ cm}^{-1}$ at a) $t_2 = 0 \text{ ps}$ , b) $t_2 = 1 \text{ ps}$ and c) $t_2 = 5 \text{ ps}$ , and for an electronic coupling of $J = -150 \text{ cm}^{-1}$ at d) $t_2 = 0 \text{ ps}$ , e) $t_2 = 0.4 \text{ ps}$ and f) $t_2 = 5 \text{ ps}$ . The excitons and vibrations are labelled for clarity. The rest of the parameters used in this simulation are provided in the text. . . . .	46
4.4	The site populations extracted from the simulated spectra (circles), compared against the populations calculated by integrating the Redfield master equation (lines). The parameters are for the same as figure 4.3. Panel a) shows results for $J = -50 \text{ cm}^{-1}$ , and panel b) shows results for $J = -150 \text{ cm}^{-1}$ . The blue and red curves show the populations on sites $A$ and $B$ following initial excitation to the higher energy exciton, while for the cyan and magenta curves the initial excitation was to the lower energy exciton. For this figure, the values from the spectral simulations were taken from the electronic excited state features. It makes no difference if the ground state features are used instead. . . . .	49
4.5	A schematic overview of the proposed method for measuring the electronic site populations for a dimer. Either the ground or excited electronic state features are chosen for the analysis. The ratio of transition dipole moments for the vibrations on the relevant electronic state can be measured with any method, though some suggestions that rely only on linear absorption and the 2DEV spectrum are described in the text. . . . .	52
4.6	Generic Feynman diagrams for the type of exciton dynamics considered in this work. During $t_2$ we allow $k$ transitions between the population states in the one exciton manifold obeying some rate equation, with no coupling into coherences. . . . .	54
5.1	Structure of Chlorophyll molecule with IUPAC numbering and ring labels, and labelling of the distinct types of carbons on the porphyrin macrocycle ( $C_a$ and $C_b$ on the pyrrole groups and $C_m$ methine groups). . . . .	60



5.2	Isotropic transient IR absorption spectra of Chl <i>a</i> (a, b) and Chl <i>b</i> (c, d). Panels a) and c) show the transient spectra at waiting time $t_2 = 250$ fs, and panels b) and d) show the full time resolved spectra. The positive (yellow/red) features indicate vibrations on the electronic ground state, and the negative (blue) features indicate vibrations on an electronic excited state. The * in panel c) indicates an artifact introduced by atmospheric water. . . . .	62
5.3	Polarization sensitive 2DEV spectra of the carbonyl stretch region of Chl <i>a</i> (a, b, c) and Chl <i>b</i> (d, e, f) at waiting time $t_2 = 250$ fs. Solid contours indicate positive values for the spectrum, whereas dashed contours indicate negative values. The isotropic response $S_{iso}$ is shown in panels a) and d), the anisotropic response $S_{aniso}$ in panels b) and e), and the anisotropy parameter $r$ is panels c) and f). The anisotropy values are overlaid by the contour plot of the isotropic spectra for the same waiting time. The value of $r$ can diverge in the vicinity of nodes in the isotropic spectrum, so the color bars in panels c) and f) are truncated to $[-0.2, 0.4]$ , the allowed range for an isolated transition. . . . .	64
5.4	Electronic (a, b) and solvent-subtracted vibrational (c) linear absorption of Chl <i>a</i> and Chl <i>b</i> . Superimposed in red (a, b) and green (c) are the laser spectra (normalized) used to excite these electronic transitions. The IR laser spectrum in (c) is normalized to 0.1. . . . .	69
5.5	Ground state equilibrium geometries of Chl <i>a</i> with 0 ethanol molecules (a, b), with 1 ethanol molecule bound to the face <i>E</i> to the phytyl chain (c, d), on the face <i>Z</i> to the phytyl chain (e, f) and with 2 ethanol molecules (g, h). . . . .	70
6.1	(a) Structure of LHCII trimer viewed from the stromal surface, from the 2.72 Å x-ray crystal structure.[113, 86] The Chl <i>a</i> and <i>b</i> are represented by their Mg (red spheres) and N (Chl <i>a</i> green, Chl <i>b</i> cyan). The carotenoids and lipids are omitted for clarity. The Chl ligands in monomer II are labelled with the crystal structure numbers. The Chl ligands in monomer III are marked with colored orbs, where the color indicates the 14 exciton states. The size of each orb indicates the degree to which that site contributes to the exciton, according to the Novoderezhkin Hamiltonian.[124] (b) The electronic absorption spectrum of LHCII at 77 K, together with the normalized excitation laser spectrum. . . . .	73
6.2	2DEV spectra of Chl <i>a</i> (a), Chl <i>b</i> (b) and LHCII (c) at $t_2 = 250$ fs. The positive features shown in yellow-red and solid contours indicate the bleach of the vibrational modes on the ground excited state, and the negative features shown in blue and dashed contours indicate absorptions by vibrations on the electronic excited states. Each spectrum is normalized relative to its own absolute maximum. The dashed lines at $\omega_1 = 14800 \text{ cm}^{-1}$ and $15400 \text{ cm}^{-1}$ mark the location of the slices shown in (d) and (e). The assignments of the bands of the LHCII spectrum (c) have been labeled. . . . .	76

6.3	2DEV spectra of LHCII at $t_2 = 0$ ps (a), 1 ps (b), 5 ps (c) and 15 ps (d). Slices through these spectra at $\omega_1 = 14800 \text{ cm}^{-1}$ and $15400 \text{ cm}^{-1}$ , the positions marked by vertical dashed lines on (a-d), are shown in (e) and (f) normalized to their absolute maxima at $t_2 = 0$ , where the dynamics have been normalized by the fit to the first right singular vector $V_1$ to facilitate visualization of the excited state dynamics, with the overall relaxation removed. . . . .	79
6.4	Singular value decomposition of the LHCII 2DEV spectrum. The first four left singular vectors (spectral component) are shown in (a-d), normalized to their individual absolute maxima. The corresponding right singular vectors (dynamics component) are shown in (e), with fits to biexponential decays from $t_2 = 0$ onwards. The fit parameters are given in table 6.1. . . . .	82
7.1	2DEV spectra calculated for $t_2 = 0$ ps for two different situations of vibronic excitation. The lineshape functions were calculated using a short time approximation. The top row shows the case where the mode being probed is itself Franck-Condon (FC) active, for the fully harmonic case and the case with small anharmonicity $\Delta_v$ . The bottom row shows the case where the mode being probed is anharmonically coupled to a lower frequency FC active mode, for two different values of the anharmonic coupling $\Delta_{12}$ . For both cases the FC active mode has a frequency of $1000 \text{ cm}^{-1}$ on the ground electronic state, $950 \text{ cm}^{-1}$ on the excited electronic state and a Huang-Rhys factor of 0.45. The FC inactive mode being probed in the spectra in the bottom row has a frequency of $1500 \text{ cm}^{-1}$ on the electronic ground state and $1450 \text{ cm}^{-1}$ on the ground electronic state. The excitation axes are referenced to the energy of the zero-phonon transition and the laser pulses are taken to be delta functions. . . . .	88
7.2	Transient IR absorption for the high frequency vibration on the electronic ground state (top), the electronic excited state (middle) and spectral densities (bottom) for the correlated bath model with two different values for the Huang-Rhys factor $S$ for the underdamped bath mode. The signatures of the wavepacket dynamics only show up in the TA for the excited state band. The detection (probe) frequency is referenced to that of the high frequency vibration on the ground electronic state prior to renormalization by the bath. . . . .	91
7.3	2DEV spectra of the vibration on the electronic excited state for a series of waiting times roughly every half period for the underdamped mode for the correlated bath model with the same parameters as in figure 7.2. The excitation axis is referenced to the frequency of the zero-phonon transition and the detection axis is referenced to the frequency of the high frequency vibration on the ground electronic state, each prior to the renormalization by the bath. . . . .	92

7.4	2DEV spectra of the vibration on the electronic ground state for a series of waiting times roughly every half period for the underdamped mode for the correlated bath model with the same parameters as in figure 7.2. The excitation axis is referenced to the frequency of the zero-phonon transition and the detection axis is referenced to the frequency of the high frequency vibration on the ground electronic state, each prior to the renormalization by the bath. . . . .	93
7.5	Center lines with respect to the excitation energy of the excited state band for a series of waiting times $t_2$ for the excited state band of the correlated bath model with the same parameters as in figure 7.2. The excitation axis is referenced to the frequency of the zero-phonon transition and the detection axis is referenced to the frequency of the high frequency vibration on the ground electronic state, each prior to the renormalization by the bath. . . . .	94
7.6	Center lines with respect to the excitation energy of the ground state band for a series of waiting times $t_2$ for the excited state band of the correlated bath model with the same parameters as in figure 7.2. The excitation axis is referenced to the frequency of the zero-phonon transition and the detection axis is referenced to the frequency of the high frequency vibration on the ground electronic state, each prior to the renormalization by the bath. . . . .	95

# List of Tables

5.1	Chl $S_1 \leftarrow S_0$ excitation energies ( $\text{cm}^{-1}$ ) . . . . .	66
6.1	Fits to the significant right singular vectors following the biexponential form $A_1 \exp(-t/\tau_1) + A_2 \exp(-t/\tau_2) + A_3$ . . . . .	83

## **Acknowledgments**

I want to thank my advisor for advising me and my colleagues for putting up with me.

# Chapter 1

## Introduction

The most fundamental meaning of coupling between electronic and vibrational transitions is the changes in the shape of the potential energy surface along a particular nuclear coordinate between different electronic states. For very small molecules like  $I_2$ , these surfaces and their basic parameters, such as vibrational frequency, equilibrium position, anharmonicity and dissociation energy, can be determined with high accuracy, using a combination of spectroscopy and theoretical calculations.[121] For larger molecules, and for molecules in solution, the dimensionality of the problem becomes too large to determine these surfaces in their complete detail, and we can at best consider only a few degrees of freedom at a time, and to introduce additional parameters to describe the coupling of the system to a bath.

The basic picture is that of the Frank-Condon approximation, where the nuclear degrees of freedom are considered fixed on the timescale of the electronic transition. The excited state dynamics are then launched from a distribution of nuclear coordinates determined by the equilibrium populations on the ground electronic state. If we consider the potential energy surfaces to be approximately harmonic, the electronic-vibrational coupling can then be described by the shift in the equilibrium positions and the changes in the vibrational frequencies between the ground and excited electronic states. A schematic illustration of these effects is shown in figure 1.1 for the one dimensional and two dimensional case.

For simple systems like gas phase  $I_2$ , there is very little information that can be obtained with, for example, 2D electronic spectroscopy (2DES) or transient absorption (TA) over just the linear electronic absorption, as there is only a single nuclear coordinate that can produce the electronic absorption lineshape. For more complicated systems, the transient spectroscopy can reveal much more about the excited state evolution by providing a direct measure of the dynamics which take place following the excitation. 2DES can provide further information, by directly reporting on the couplings that exist between the different degrees of freedom important for driving those dynamics.

Two dimensional spectroscopy has been well developed both in the visible regime, where it probes electronic transitions and excited state dynamics and in the infrared, where the ground state vibrational structure and dynamics are interrogated. By resolving the excitation frequency as well as the detection frequency, it improves over TA in several ways. On

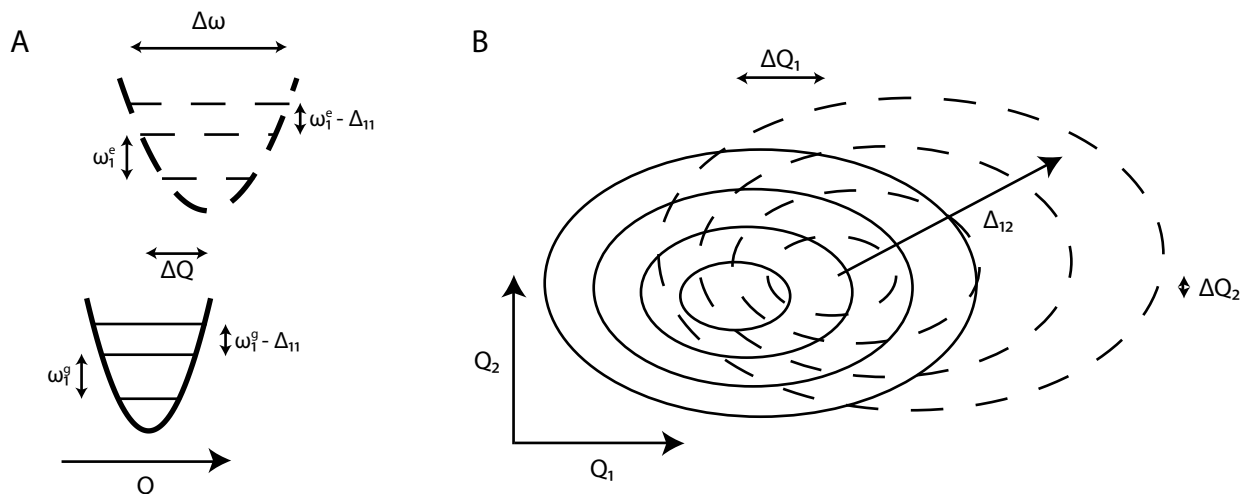


Figure 1.1: Schematic representations of the typical physical pictures of electronic-vibrational coupling mechanisms. A) A single coordinate picture depicting the strongest mechanisms of coupling, the displacement of the equilibrium coordinate  $\Delta Q$  and the change in the vibrational frequency  $\Delta\omega$  between the ground and excited electronic states. B) An extension of this picture to multiple coordinates, where anharmonic coupling  $\Delta_{12}$  between vibrational modes can induce a coupling to the electronic transition in an otherwise inactive mode.

the margins, the Fourier transform techniques remove the usual trade off between time resolution and frequency resolution. Excitation pulses with large bandwidth and short duration can be used to excite many transition in the system, which are then resolved in frequency by using interferometric techniques. Furthermore, there is inherently new information contained in the two dimensional spectroscopies that can, at best, only be inferred from one dimensional techniques. This includes the separation of the diagonal and antidiagonal linewidths for a transition, together with their dynamics, which are capable of providing information about the structure of the coupling between the system and its bath, separating different components by the timescales with which they are able to relax.

The more dramatic improvement of 2D spectroscopy over TA is the capability of directly resolving crosspeaks between different transitions. These cross peaks provide direct information about the coupling between different states, and can be used to follow the flow of energy through a complicated system. For 2D infrared spectroscopy (2DIR), this might mean distinguishing different secondary structures in a protein by the distinct patterns of the crosspeaks in the peptide amide region,[143] or tracking the rate of complexation in a chemical exchange reaction.[182] For 2DES it might mean following the motion of a vibrational wavepacket as it oscillates on the ground or excited potential energy surface,[22] or the transfer of excitation energy between different pigments in a molecular aggregate, such as a photosynthetic antenna complex.[18]

These methods certainly have their limitations. 2DIR is capable of providing a great deal

of information about a molecule’s structure and structural dynamics, but it is very difficult to extend it to transient species like electronic excited states without dramatically increasing the experimental complexity.[15, 32, 115] Purely electronic spectroscopies like 2DES have proven to be very useful tools for studying the electronic excited state dynamics and the energetic flow of excitations, but they are relatively lacking in structural information, except what can be determined from wavepacket analysis and comparison to model calculations. It would potentially be of substantial interest for certain classes of problems to experimentally obtain the link between the electronic and structural degrees of freedom more directly. There are several 1D transient techniques that begin to fill this gap between these different tools, such as transient infrared spectroscopy and femtosecond stimulated Raman, but there has not been a successful 2D extension of these techniques, which could take their advantages but mitigate the deficiencies that come with 1D transient techniques. To address this gap, we have set forth to develop 2D electronic-vibrational spectroscopy (2DEV), which would directly measure the crosspeak between the electronic and vibrational degrees of freedom, and would resolve both the electronic excitation frequency axis as well as the infrared detection frequency axis.

In chapter 2 we discuss the practical tools and instrumentation necessary to implement and develop 2DEV spectroscopy in our lab. This includes the design and construction of a broadband short pulse visible noncolinear optical parametric amplifier (NOPA) to generate the visible excitation pulses for the experiment. The experimental design is based on earlier methods for performing multidimensional optical spectroscopic measurements in the partially colinear pump-probe geometry and takes advantage of an optical pulse shaper to perform the interferometric measurements and to extract the desired signal using phase cycling,[154, 122] with the details chosen for the particular situation of exciting the sample with visible laser pulses and probing it with the infrared. The experimental setup is described in detail in section 2.2. To fully take advantage of the potential promise of 2DEV, it was necessary for the NOPA to be optimized for this application. This meant, for example, that particular focus had to be paid to the quality of the spatial mode of the NOPA signal and in particular its spectral homogeneity, a common issue in typical NOPA designs, as well as to ensure that the excitation pulse could be fully compressed to its Fourier transform limit at the position of the sample with the broadest possible bandwidth using the equipment and the pulse shaper available at this time, with sufficient power to drive the experiment. These constraints together resulted in the NOPA design discussed in section 2.3. The extreme difference in the colors used in the experiment, together with the experimental geometry described in section 2.2, means that it is impossible to extract the desired signal using traditional phase matching techniques. Instead, we utilize the control afforded to us by the pulse shaper to extract the signal with phase cycling. The mathematical and practical details of the phase cycling method we used are discussed in section 2.4.

We described the initial demonstration of 2DEV in reference [127] where we demonstrated that the correlated electronic and vibrational dynamics in a model charge transfer system, the laser dye DCM, could be measured. The structure of DCM is shown in figure 1.2, together with two possible schema for the essential excited state dynamics following the excitation.



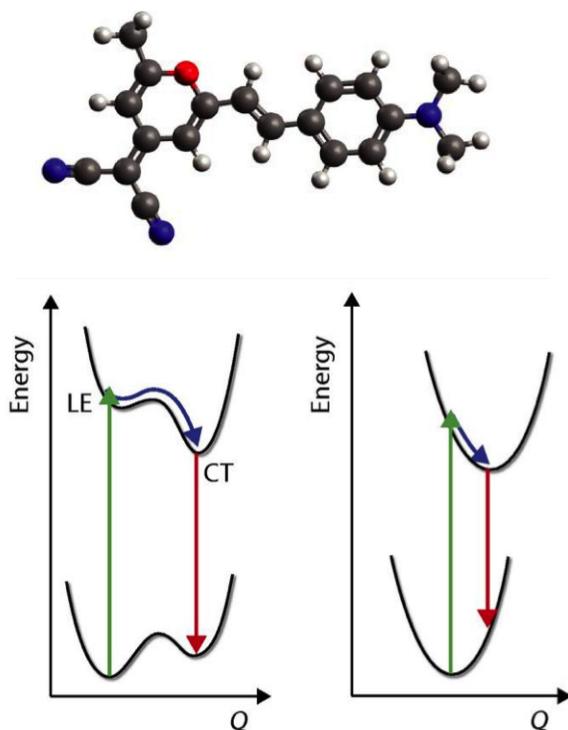


Figure 1.2: Structure for the dye molecule DCM used in the initial demonstration of 2DEV (top) together with the two models for the initial excited state evolution for this molecule (bottom).

DCM can be considered as a type of ‘push-pull’ chromophore, containing both an electron donating dimethylamino group as well as a pair of electron accepting cyanomethylene groups. The result of this is a fast charge transfer from the donating side to the accepting side upon electronic excitation. This causes the electronic transition to be very strongly coupled to the bath, and generates a very broad, strongly solvatochromic absorption band, together with a very large Stokes shift.[170] Two different models have been proposed for the dynamics of the charge transfer process in this molecule, illustrated in figure 1.2. In one situation, there would be a barrier to the charge separation, separating the locally excited state (LE) from the charge transfer state (CT), while in the other case this process would be barrierless and could not be described as two distinct states. The 2DEV spectra of this molecule, shown in figure 1.3, definitively answer which of these processes is occurring. By tracking the evolution of an important vibrational mode localized primarily on the acceptor side as it shifts in central frequency along the vibrational detection axis, as well as along the electronic excitation axis, we are able to show that the dynamics are well correlated so long as the wavepacket remains near the Franck-Condon region. There is no evidence of two distinct configurations separated by a substantial barrier, as the changes in the vibrational

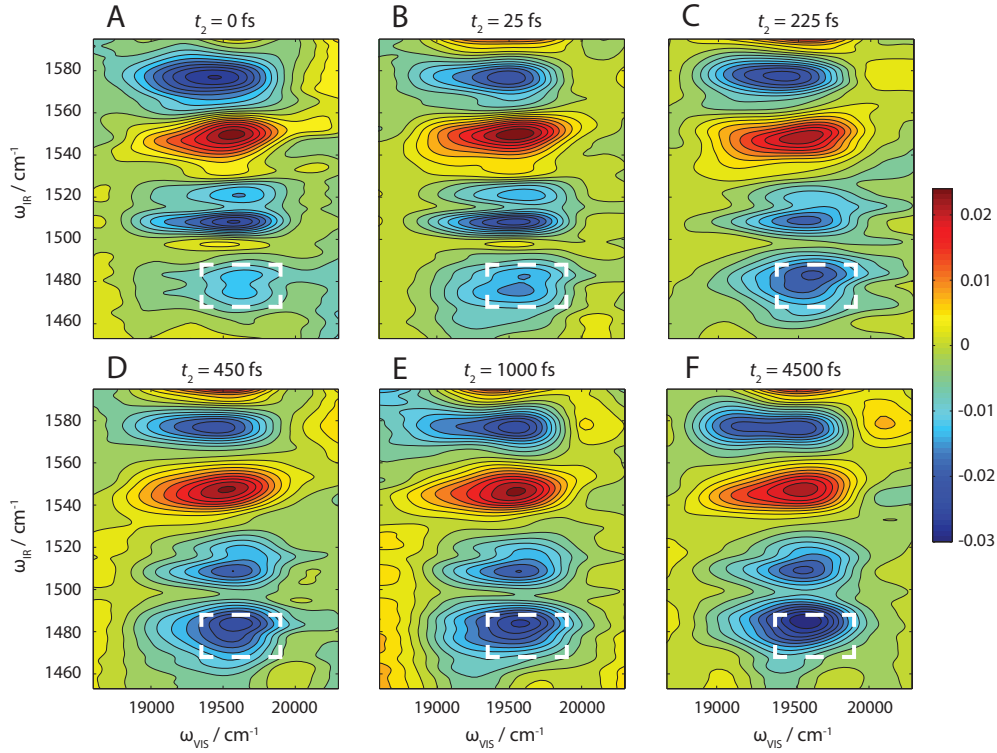


Figure 1.3: A series of 2DEV spectra of DCM in DMSO at different waiting times  $t_2$ . The positive (yellow-red) bands are due to vibrational modes on the electronic ground state, while the negative (green-blue) bands are due to vibrational modes on the electronic excited state. The dashed box marks the initial position of the main band of interest, illustrating the simultaneous blue shift of the vibrational frequency with the red shift of the electronic excitation frequency.

spectrum are all continuous, and restricted to the high frequency modes which are coupled to the solvation coordinate. Subsequent simulations calculating the 2DEV spectra arising from these two possible models demonstrate conclusively that this interpretation is correct.[166]

While demonstrating an important proof of principle that the experiment was not only feasible but could also report on the types of dynamics not readily captured by other spectroscopic techniques, the analysis of the experimental results we were capable of providing in this work was quite limited. Together with reference [43], the work described in chapter 3, which is also described in reference [108], presents the initial quantitative analysis of the type of information content that is unique to 2DEV over other techniques. In this chapter we discuss a simple physical model capable of reproducing many of the features observed in the experimental 2DEV spectra of isolated chromophores. We use a short time approximation to the third order lineshape function to derive an analytical expression for the centerline slope of a transition in the 2DEV spectrum, and show that this is proportional

to fluctuations induced by the coupling of the vibration to the bath. The proportionality constant, which we term  $\alpha_0$ , is of significant interest, as it describes the degree to which the reorganization energy for the vibrational transition changes between the ground and excited electronic states. We are unaware of a different technique capable of easily measuring this quantity. We demonstrate the major features predicted by this simple model with experimental results from the laser dye DTTCl. The dynamics of the centerline slope for the band arising from exciting the  $S_1$  electronic state and probing the C=C backbone stretching mode follows exactly the prediction made by the model, and we were able to measure  $\alpha_0 \simeq 1.5$ , a value which is commensurate with the change in the magnitude of the electronic permanent dipole moment between the  $S_0$  and  $S_1$  electronic states for this molecule. This work provides a theoretical basis with which we can understand the 2DEV spectra of simple systems, and supports this theoretical basis with experimental results.

In chapter 4 we extend the theoretical model developed in reference [43] and chapter 3 to the case of an electronically coupled dimer. The purpose of this work is to consider the potential application of 2DEV to studying the dynamics of excitation energy transfer in extended systems like photosynthetic light harvesting complexes. The essential idea is to try to use discrete localized vibrational motions as a proxy for position in a nanoscopic system, and to use them to track the flow of electronic excitation energy through the complex. In this discussion, we develop an approximate model for calculating the 2DEV spectra for a dimer system using standard approximations for response functions of dimer systems, with the population dynamics added back in an *ad hoc* manner consistent with Redfield theory under the secular approximation. Using this model, we are able to show how 2DEV could potentially be used to follow the motion of excitation energy through a complex. Furthermore, we were able to derive a method by which, in principle, it would be possible to use the 2DEV results to measure the electronic populations directly in the site basis. This is not possible with standard electronic spectroscopies, as these interact with the system only in the natural basis for the electronic excitations, the so-called exciton basis. The transformation to the site basis can only be made in this situation by fitting to complicated underdetermined models to determine the Hamiltonian in the site basis. This process is generally highly inexact, as it is often very difficult to reliably distinguish between the effect on the electronic spectrum of coupling interactions versus shifts in the electronic site energies. 2DEV has the potential to provide the link between these two physically important bases in a very direct way, which provides significant promise in the study of electronic energy transfer in photosynthetic light harvesting.

Before we could attempt to apply the methods proposed in chapter 4 to an actual photosynthetic light harvesting complex, it was of course necessary to understand the 2DEV spectra of the isolated chromophores. Our ultimate target was the major photosynthetic light harvesting complex for photosystem II in higher plants, known as LHCII, which binds a combination of chlorophyll (Chl) *a* and *b*, as well as several carotenoids. Therefore, in chapter 5, we discuss the 2DEV spectra for these Chls in isolation, in ethanol solution. The spectra are somewhat complex due to the variety of carbonyl and chlorin ring stretching modes that are IR active in the spectral region near  $1600\text{ cm}^{-1}$ , which will each have some

degree of shift between the ground and excited states. Furthermore, the spectra contain contributions from both the  $Q_y$  and  $Q_x$  absorption bands, introducing some complex structure along the excitation axis. Additional complexities arise from the effects on the spectrum of different axial coordination states of the central Chl Mg. In solvents with varying nucleophilicity, Chl may axially coordinate to 0, 1 or 2 solvent molecules, which produces shifts in the spectral absorptions for both the electronic and vibrational degrees of freedom. These shifts were identified separately for the electronic absorption and the vibrational frequencies, and assigned to the same effect.[35, 61] In ethanol, both the states where 1 or 2 solvent molecules are bound to the Mg are stable, and in the 2DEV spectra we are able to separately resolve the peaks corresponding to each of these coordination states along both the electronic excitation axis as well as the vibrational detection axis. By directly measuring the crosspeak between these two degrees of freedom, we are able to definitively demonstrate that the features identified in the linear spectra of the two separate domains do indeed arise from the same state. These results are also presented in reference [106].

Once we were able to describe and assign the major features of the 2DEV spectra of isolated Chl *a* and *b*, we were able to apply this in an attempt study the excitation energy transfer dynamics among the Chls in LHCII isolated from Spinach. This work is presented in chapter 6, and is also described in reference [109]. We demonstrate that it is feasible to measure the 2DEV response of these complicated pigment protein complexes at cryogenic temperatures, and by following the dynamics for the vibrational bands which we can definitively assign to either Chl *a* or Chl *b* we are able to show that we can indeed observe the effects of electronic excitation transfer using this technique. Using spectral decomposition methods, we can furthermore identify spectral features associated with three different timescales of excitation energy transfer – a fast timescale that primarily arises from the Chl *b* to Chl *a* energy transfer, a slower relaxation associated with equilibration within the Chl *a* moieties and transfer to the exit sites, and the distinct signatures of transient intermediates, which are presumably due to the higher energy Chl *a* states and lower energy Chl *b* states which are important in the pathways of energy transfer through the complex to the low energy Chl *a* exit sites. The spectra are very rich in their spectral and dynamical features, and while we are able to clearly separate features associated with the different types of Chl, it is very difficult to make assignments of bands to specific sites, as we would ultimately like to do. This is because of limitations in current techniques from predicting the effects on the shifting of the vibrational frequencies on the electronically excited states induced by the complex environment of the protein. These shifts can be induced by a variety of mechanisms, such as different hydrogen bonding patterns, different coordination states and axial ligands and differences in the local electrostatic environments of the individual pigments. Our experimental results demonstrate that the desired information is present in the data and in principle it could be extracted, but we require improvements in the current state of theoretical and computational techniques before it will be possible to quantitatively assign the bands and extract this information in a meaningful and useful way.

Finally, in chapter 7 we discuss possible future directions of study for further development and application of 2DEV spectroscopy. This comes in two major parts, the development of its

usefulness for studying small molecule photophysics such as a study of the spectral signatures and physical quantities which might arise from conical intersections in the topology of the potential energy surfaces, and in the further understanding of how electronic energy transfer could be studied using this experimental method. There remains a significant number of gaps in our understanding of the spectral structures which might arise in these situations, and it may be that the true usefulness of 2DEV as an experimental technique has yet to be revealed.

# Chapter 2

## Two-Dimensional Electronic-Vibrational Spectrometer

### 2.1 Introduction

In 2DEV spectroscopy, the colors involved differ in wavelength by an order of magnitude. This, in addition to the difficulties involved with using mid-IR laser sources, provides a number of constraints on the experimental design of the spectrometer. In particular, it is practically very difficult to implement a 2DEV spectrometer which takes advantage of phase matching to generate a background-free heterodyne detected signal, although it is in principle possible to design such a setup.[17, 42] Because of this, the design of the 2DEV spectrometer is based on previously demonstrated 2D coherent spectrometers in the partially collinear pump-probe geometry based on pulse shaping and phase cycling.[122, 154] The details of the experimental design are provided in this chapter.

### 2.2 Experimental Design

A schematic of the experimental setup, which is essentially a high time resolution transient IR absorption spectrometer with the addition of a pulse shaper into the visible pump beam, is shown in figure 2.1. The excitation laser is derived either directly from a Ti:Sapphire (Ti:Saph) regenerative amplifier (Coherent Legend Elite) seeded by a Ti:Saph oscillator (Coherent Micra), or from a home-build non-collinear optical parametric amplifier (NOPA), the details of which are provided in section 2.3. The IR probe pulse is derived from a home-built near-IR OPA equipped with difference frequency generation between the signal and idler to convert the laser to the mid-IR.[73] The details of this OPA can be found in the dissertation of Aaron J. Van Tassle.[169]

After the pump beam passes through the prism compressor immediately following the NOPA, it is rotated by a half wave plate to the polarization required for the pulse shaper (Fastlite Dazzler). The pulse shaper is used to compress the pulse to nearly the Fourier

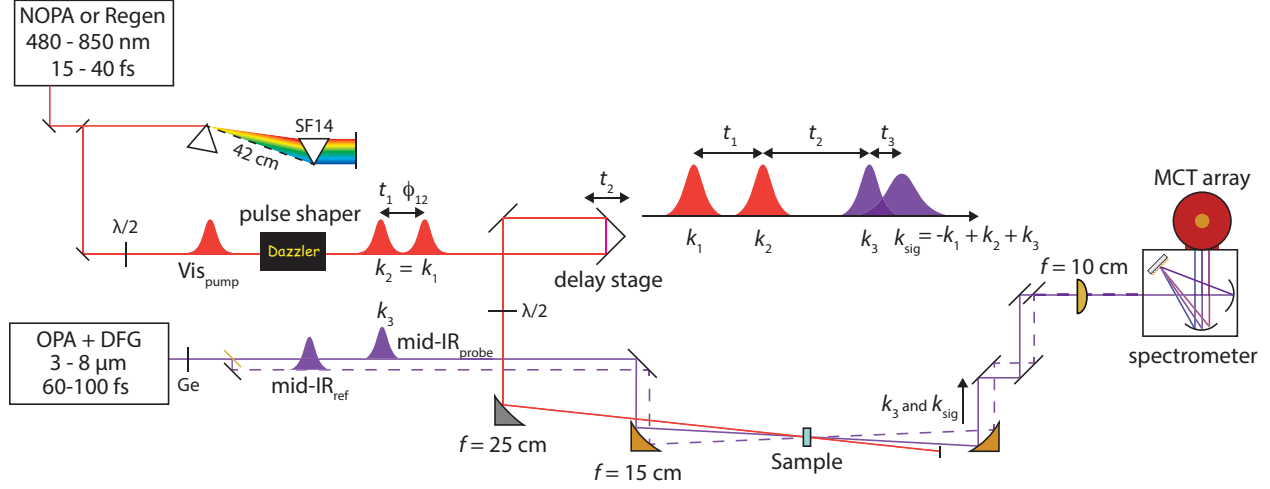


Figure 2.1: Schematic of the 2DEV experimental setup. The visible pump beam is shown in red, and the IR probe beam is shown in purple. The  $t_1$  time delay and  $\phi_{12}$  relative phase difference between the pump pulse pair is generated and controlled by the pulse shaper (Dazzler), while the  $t_2$  time delay between the pump and the probe is controlled with the delay stage. A reference beam (dashed purple line) follows next to the probe beam through the sample and is imaged onto a second array in the detector. The signal is self heterodyned by the collinear probe beam. The relative polarization between the pump and the probe are determined by the half wave plate in the pump beam before the focusing OAP.

transform limit (FTL), and to split the pulse into two identical pulse pairs with a controlled time delay  $t_1$ , as well as a controlled relative phase  $\phi_{12}$ . The details of the phase cycling used to isolate the 2DEV signal is described in section 2.4. This pump pulse pair is then reflected from a retroreflector mounted on a computer-controllable delay stage (Newport) which is used to control the relative delay between the visible pump pulse and the IR probe pulse  $t_2$ . The beam is then passed through another half wave plate mounted in a computer controllable rotation stage (Thorlabs) to control the relative polarization between the pump and probe beams, allowing for the measurement of the anisotropy response of the transient signal. The pump beam is then focused into the sample by a silver coated  $f = 25$  cm  $90^\circ$  off-axis parabolic mirror (OAP) to a spot of  $\sim 250$   $\mu\text{m}$ , where it is spatially overlapped with the IR probe beam.

The IR beam, which, for alignment purposes, is combined with a mode-matched He-Ne on the mid-IR long-pass filter in the OPA, first passes through a series of Ge plates (removed during alignment with the HeNe). These are used to compress the pulse by compensating for the other materials in the probe line, such as the ZnSe beam splitter, the  $\text{CaF}_2$  sample windows and, if the experiment is performed at cryogenic temperatures, the ZnS and  $\text{CaF}_2$  cryostat windows.[40] The reference beam is then split from the probe beam with a ZnSe beamsplitter ( $\sim 40\%$  R). The probe and reference beams are focused through the sample

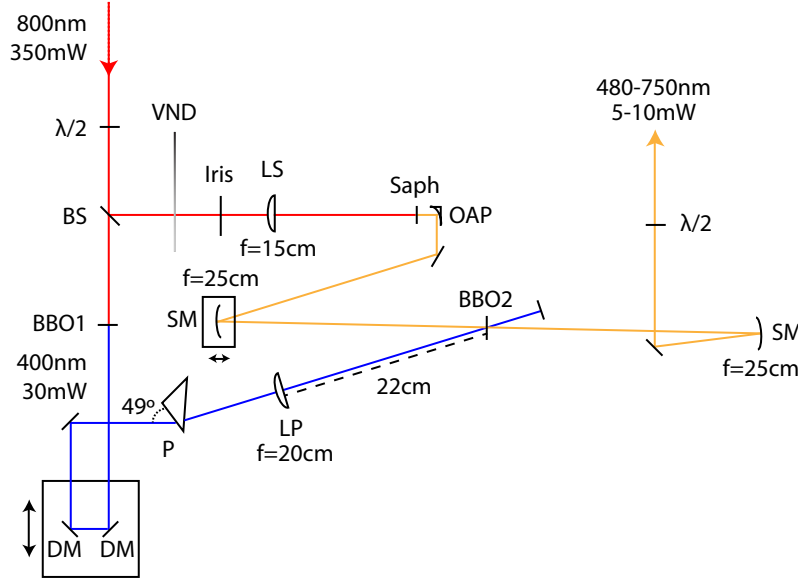


Figure 2.2: Schematic of the NOPA with pulse-front-tilt matching between the pump and the seed.  $\lambda/2$ : half wave plate, BS: 2% reflective beam splitter, BBO1:  $\beta$ -BBO for 800 SHG,  $\theta = 29.2^\circ$ ,  $\phi = 90^\circ$ , 1mm thick, DM: dichroic mirror, reflect 400nm, transmit 800nm, P:  $90^\circ$  fused silica prism, LP: fused silica lens  $f = 20\text{cm}$ , 400nm AR coating, VND: variable neutral density filter, Iris: adjustable aperture, LS: BK7 lens  $f = 15\text{cm}$ , 650 – 1050nm AR coating, Saph: 3mm thick sapphire plate, uncoated, OAP: silver coated  $90^\circ$  off axis parabolic mirror,  $f = 2.5\text{cm}$ , SM: silver coated spherical mirror,  $f = 25\text{cm}$ , BBO2:  $\beta$ -BBO for amplification,  $\theta = 29.2^\circ$ ,  $\phi = 90^\circ$ , 2mm thick.

by a  $f = 15\text{ cm}$   $90^\circ$  gold coated OAP to a spot size of  $\sim 160\text{ }\mu\text{m}$ , such that the focal spots of the probe and reference are displaced and only the probe is overlapped with the pump beam. The beams are then recollimated by a matched OAP, and focused onto the slit of a spectrometer (HORIBA TRIAX 190) with a  $f = 10\text{ cm}$  ZnSe lens, such that the probe and reference beams are imaged onto the two 64 element HgCdTe photodiode arrays of the detector (Infrared Associates). The signal is then passed through a 128 channel boxcar integrator (Infrared Systems Development) balanced to match the responses of the individual HgCdTe elements. The probe spectrum is then normalized by the reference spectrum on a pulse-to-pulse basis to mitigate the fluctuations in the IR laser power.

## 2.3 Visible Pulse Generation

The NOPA, a schematic of which is shown in figure 2.3, was built incorporating several optimization elements based on earlier designs,[156, 13] together with some simplifications allowed by the needs of our application. In particular, we use a partially reflected seed



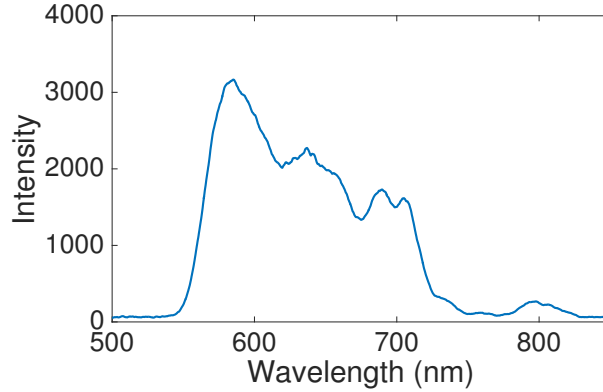


Figure 2.3: Typical spectrum of the NOPA signal optimized for the center of the tuning range.

generation line, which reduces the chirp of the seed, and implement pulse-front matching between the pump and the seed, which significantly improves the spectral homogeneity of the beam. A single amplification stage was found to be capable of producing sufficient power for the experiment, so a second stage was not incorporated.

In detail, 350 mW of the output from the amplifier is passed through a half wave plate to rotate the polarization, then split into the two lines of the NOPA, with 2% being split off to the seed generation line while the remaining 98% is used for the pump line. To generate the seed, the beam is passed through a variable neutral density filter and an iris to control both the power and the mode of the beam, then focused into a 3 mm sapphire plate with a  $f = 15$  cm lens to generate a white light continuum. The white light is then collimated with a  $f = 2.5$  cm silver coated  $90^\circ$  OAP. A mirror is used instead of a lens so as to reduce the amount of chirp imparted to the white light prior to the amplification stage, which allows for a greater portion of the seed bandwidth to be temporally overlapped with the pump in the amplification crystal, and hence for a larger bandwidth in the output of the NOPA. An OAP is used instead of a spherical mirror to avoid the introduction of significant astigmatism to the seed beam, which can be a problem when using short focal length spherical mirrors. The seed is then focused by a  $f = 25$  cm silver coated spherical mirror towards the amplification crystal, a 2 mm thick type II  $\beta$ -BBO crystal ( $\theta = 29.2^\circ$ ,  $\phi = 90^\circ$ ), from a distance of  $\sim 30$  cm. The distance from the focusing mirror to the crystal is adjusted to optimally match the mode of the seed beam to that of the pump beam.

The remaining 98% of the input beam is passed through a 1 mm thick type II  $\beta$ -BBO crystal ( $\theta = 29.2^\circ$ ,  $\phi = 90^\circ$ ) to generate  $\sim 30$  mW of the second harmonic at 400 nm. The remainder of the 800 nm fundamental beam is removed by two dichroic mirrors (R 400 nm, T 800 nm) placed on an adjustable delay stage to control the timing of the pump relative to the seed. The beam is then passed through a fused silica prism with apex angle  $\theta_{\text{apex}} = 45^\circ$  at a  $49^\circ$  angle of incidence, as close to the apex as possible. It is then focused with an

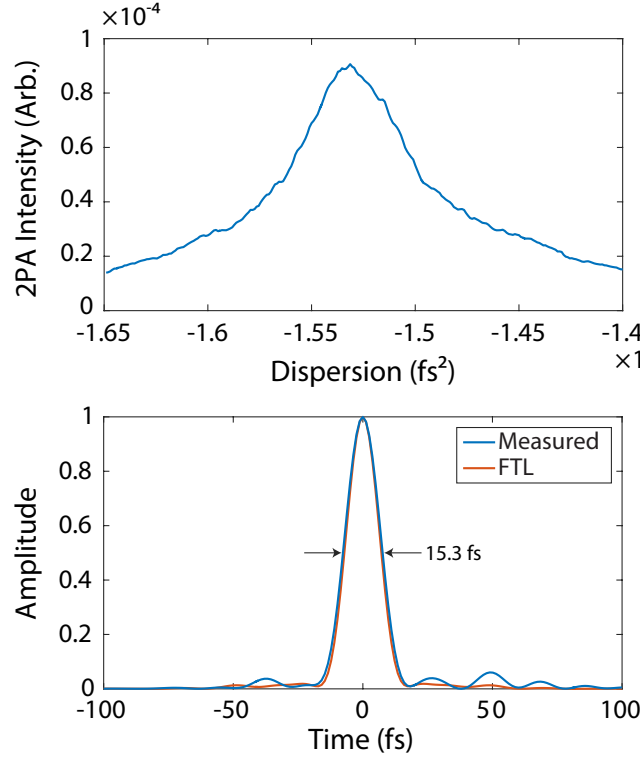


Figure 2.4: Two photon absorption strength as a function of second order dispersion applied by the pulse shaper (top) and the accurately measured temporal profile and the FTL for the visible pulse using SRSI (bottom). The measured FWHM is 15.3 fs, as compared to the FTL 14.3 fs.

$f = 20$  cm fused silica lens towards the amplification crystal from a distance of 22 cm. The purpose of this prism is to tilt the wavefront of the pump pulse relative to the direction of propagation. The angles of the prism's geometry, the angle of incidence of the laser on the prism, and the ratio of the focal length of the lens and the distance from the crystal, are chosen to optimize the match between the wavefronts of the pump and seed pulses inside of the crystal,[13] while also maintaining a small enough pump spot to have sufficient pump fluence for efficient amplification. The wavefront matching of the pulses aids the generation of a spectrally homogeneous signal, compromised by the non-collinear crossing of the pump and seed beams at the amplification crystal in the NOPA. When the wavefront tilt is not corrected, the result is an angular dependence of the amplification frequency and a tilted pulse-front in the signal, which can make it impossible to compress the pulse to the Fourier transform limit.

After generation, the signal is collimated with a second  $f = 25$  cm silver coated spherical mirror, and passed through another half wave plate before being routed to a prism compressor and the experimental setup. Immediately subsequent to the amplification stage, the NOPA signal is  $\sim 5 - 10$  mW, tunable from 480 – 750 nm with  $\sim 100 - 150$  nm bandwidth. An

example spectrum of the signal at the center of the tuning range before the prism compressor is shown in figure 2.3. After the signal is passed through another half wave plate to minimize reflection losses on the prisms, it is sent to the prism compressor, shown in figure 2.1, which is composed of two equilateral SF14 prisms spaced 42 cm apart apex-to-apex. The purpose of this prism compressor is not to fine tune the pulse duration, but to impart as much negative second order dispersion as possible, without severely truncating the spectrum, to compensate for the dispersion induced by the 2.5 cm long TeO<sub>2</sub> crystal of the pulse shaper. This allows the pulse shaper to be able to shape a larger bandwidth for the fine-tuning of the compression and generation of the pump pulse pair. In this configuration, the prism compressor imparts  $\sim -7000 \text{ fs}^2$ , compared to the  $\sim 12500 \text{ fs}^2$  imparted by the material dispersion of the pulse shaper crystal.[171] The use of prisms made from highly dispersive glass for this application has the limitation of imparting significant third order dispersion, limiting the size of the prisms that can be used and therefore the distance between the prisms, and the amount of negative second order dispersion that can be imparted. This limitation could be addressed by replacing the prisms with a combined grating-prism compressor,[56] which would potentially allow for the use of pulses as short as 10 fs, without additional major changes.

A two-step approach was used to optimally compress the visible pulse. For the rough compression it is focused onto a SiC photodiode, which, with an optical bandgap  $\simeq 400 \text{ nm}$ , is sensitive to the two-photon absorption (2PA), but not the one-photon absorption. The pulse shaper is used to scan the phase parameters and to maximize the 2PA signal, which will correspond to the optimally compressed pulse. An example of the results of a scan of the second order dispersion is shown in figure 2.4. Once the pulse has been roughly compressed in this way its duration can be precisely measured using self referenced spectral interferometry (SRSI) using a Wizzler (Fastlite).[125] Feedback between the precise spectral phase measured from the SRSI and the pulse shaper can be used to compress the pulse to nearly the FTL. An example of a 15.3 fs pulse measured using SRSI is shown in figure 2.4, together with the corresponding 14.3 fs FTL. The cross-correlation time between the visible and IR pulses can then be estimated from the step-like transient absorption response of a  $50 \text{ } \mu\text{m}$  Ge plate.

## 2.4 Signal Extraction

The 2DEV signal can be considered as arising from a time dependent third-order polarization, which can be calculated using standard perturbation theory approaches[120] as the triple convolution of the third-order response function  $S^{(3)}(t_1, t_2, t_3)$  with the electric field of the laser pulses  $E(t)$  given by

$$\begin{aligned} P^{(3)}(t) &= S^{(3)} \otimes E \otimes E \otimes E \\ &= \int_0^\infty \int_0^\infty \int_0^\infty S^{(3)}(\tau_1, \tau_2, \tau_3) E(t - \tau_1 - \tau_2 - \tau_3) E(t - \tau_2 - \tau_3) E(t - \tau_3) d\tau_1 d\tau_2 d\tau_3. \end{aligned} \quad (2.1)$$

For a sequence of three short laser pulses, the electric field at the sample can be described as  $E(t) = \sum_{i=1}^3 E_i(t)$  with

$$E_i(t) = A_i(t - t_1) \exp [-i\omega_i^0(t - t_i) - i\phi_i + i\mathbf{k}_i \cdot \mathbf{r}] \quad (2.2)$$

where  $A_i(t)$  is the envelope of the  $i$ th pulse, considered to be centered at  $t_i$ ,  $\omega_i^0$  its carrier frequency,  $\phi_i$  its absolute phase relative to some common reference and  $\mathbf{k}_i$  its wavevector. The total third-order polarization for such an electric field is rather complicated, including many different signal pathways, and can be expanded in these signals as

$$P^{(3)}(t) = \sum_s P_s^{(3)}(t) \exp [-i\omega_s t + i\mathbf{k}_s \cdot \mathbf{r}] \quad (2.3)$$

where  $\omega_s = \pm\omega_1 \pm \omega_2 \pm \omega_3$  and  $\mathbf{k}_s = \pm\mathbf{k}_1 \pm \mathbf{k}_2 \pm \mathbf{k}_3$  is a linear combination of the frequency and wavevector of the three interactions between the sample and the laser pulses. This time dependent polarization will then radiate a signal with frequency  $\omega_s$  in a direction parallel to  $\mathbf{k}_s$ . [120]

Traditional degenerate or near-degenerate 2D spectroscopic techniques can take advantage of these phase matching conditions to generate the desired signal spatially separated from the other undesired signals by arranging the three beams in useful geometries, such as the square so-called boxcar geometry.[17] For highly non-degenerate experiments like 2DEV, however, the geometries necessary, while not impossible,[42] become difficult and impractical. This is due to the nearly order of magnitude difference between the wavelengths of the visible pump pulses and the IR probe pulse, which affects the phase matching direction by the relation between the magnitude of the wavevector and the wavelength of the light  $|\mathbf{k}| = 2\pi/\lambda$ . Because of the practical difficulties of implementing the experimental geometries necessary for the background-free 2DEV signal, especially when accounting for the necessity of accurate and stable sub-wavelength delay control of the visible pulses for the interferometric measurement of the photon echo signal, it is highly advantageous to instead use the partially collinear pump-probe geometry  $\mathbf{k}_1 = \mathbf{k}_2 \neq \mathbf{k}_3$  with phase cycling methods to isolate the desired signal from the background.

In the pump-probe geometry, the signal that is detected will include the desired 2DEV signal together with the transient absorption arising from two interactions with either of the visible pump pulses and the static background of the probe beam. The total measured amplitude to third order is given by

$$\begin{aligned} \left| \tilde{S}_T^{(3)}(t_1, t_2, \omega_3; \Delta\phi_{12}) \right|^2 &= \left| \left( \tilde{S}_{123}^{(3)}(t_1, t_2, \omega_3) + \tilde{S}_{113}^{(3)}(t_1, t_2, \omega_3) + \tilde{S}_{223}^{(3)}(t_1, t_2, \omega_3) + 1 \right) E_3(\omega_3) \right|^2 \\ &= \left| \tilde{S}_{123}^{(3)}(t_1, t_2, \omega_3) E_3(\omega_3) \right|^2 + \left| \left( \tilde{S}_{113}^{(3)}(t_1, t_2, \omega_3) + \tilde{S}_{223}^{(3)}(t_1, t_2, \omega_3) + 1 \right) E_3(\omega_3) \right|^2 \\ &\quad + 2 \operatorname{Re} \left[ e^{i\Delta\phi_{12}} \tilde{S}_{123}^{(3)}(t_1, t_2, \omega_3) \left( \tilde{S}_{113}^{(3)}(t_1, t_2, \omega_3) + \tilde{S}_{223}^{(3)}(t_1, t_2, \omega_3) + 1 \right)^* \right] \left| E_k(t_3) \right|^2 \end{aligned} \quad (2.4)$$

where

$$\tilde{S}_{ij3}^{(3)}(t_1, t_2, \omega_3) E_k(\omega_3) = \int dt_3 e^{-i\omega_3 t_3} S^{(3)}(t_1, t_2, t_3) \otimes_{t_1} E_i^*(t_1) \otimes_{t_2} E_j(t_2) \otimes_{t_3} E_k(t_3) \quad (2.5)$$

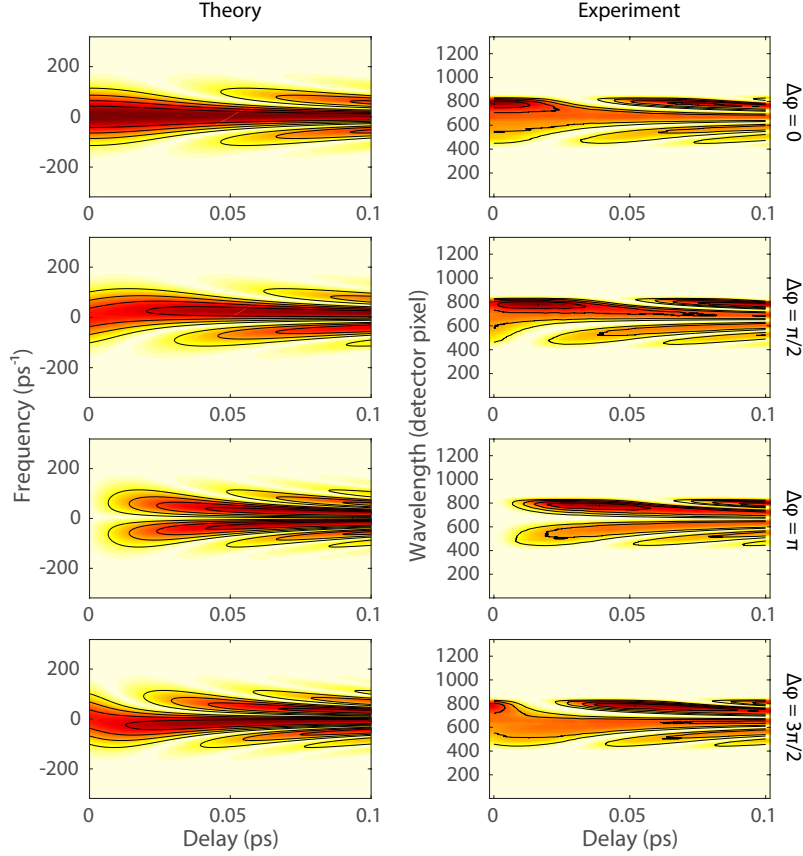


Figure 2.5: Comparison between theoretical (left) and experimental (right) interference patterns between the pump pulse pair as a function of delay time for relative phases  $\Delta\phi = 0, \pi/2, \pi$  and  $3\pi/2$ .

is the Fourier transform over  $t_3$  of the signal convolved with the laser fields. The total field amplitude is measured because of the use of a square-law detector. The key to extracting the desired signal,  $\tilde{S}_{123}^{(3)}(t_1, t_2, \omega_3)$ , comes from the difference in how this term and the various background terms depend on the relative phases of the electric fields. The major background terms can be removed by modulating  $\Delta\phi_{12} = \phi_1 - \phi_2$ , the relative phase between the two pump pulses. The signal term acquires an overall prefactor that depends on this phase as  $e^{i\Delta\phi_{12}}$ , while the major background terms are unaffected. Therefore, the signal can be effectively isolated by repeating the measurement  $n$  times with  $n$  different values of  $\Delta\phi_{12}$  evenly spaced around the unit circle, demodulating the measured signal by the acquired

phase factor and summing the results to give

$$\begin{aligned} & \frac{1}{n} \sum_{k=0}^{n-1} e^{-2\pi k i/n} \left| \tilde{S}_T^{(3)}(t_1, t_2, t_3; \Delta\phi_{12} = 2\pi k/n) \right|^2 \\ &= 2\tilde{S}_{123}^{(3)}(t_1, t_2, \omega_3) \operatorname{Re} \left[ \tilde{S}_{113}^{(3)}(t_1, t_2, \omega_3) + \tilde{S}_{223}^{(3)}(t_1, t_2, \omega_3) + 1 \right] \left| E_k(t_3) \right|^2 \\ &\simeq 2\tilde{S}_{123}^{(3)}(t_1, t_2, \omega_3) \left| E_k(t_3) \right|^2. \quad (2.6) \end{aligned}$$

The cross-terms between the 2DEV signal and the transient absorptions terms cannot be completely removed, but because they scale as the square of a third-order field they will be negligible compared to the desired signal, which is linear in the third-order field. When the probe spectrum is removed in the division by the reference spectrum, we have then effectively isolated the desired 2DEV signal. To convert this to the purely absorptive 2DEV spectrum, this signal can be Fourier transformed about  $t_1$ , though it is typically beneficial to process the data further to improve the quality of the signal.

If it is desired to separate the rephasing pathways from the nonrephasing pathways, a time domain windowing method can be used. The separation will rely on the difference in the relative sign of the phase evolution for these pathways during  $t_1$  and  $t_3$ , which means that they can only be separated if the number of relative phases used in the phase cycling  $n \geq 3$ , so that both the real and imaginary parts of the signal have been obtained. Once the phase cycling has been applied, the signal must be Fourier transformed along  $\omega_3$  to the pure time domain response. Because only the positive values of  $t_1$  have been measured, this places the rephasing signal in the quadrant with  $t_3 \leq 0$ , because of the opposite signs of the phase evolution during these time periods for these pathways, while the nonrephasing signal, which evolves with the same sign during these time periods, will be constrained to the  $t_3 \geq 0$  quadrant. The separate rephasing and nonrephasing spectra can then be obtained by using an appropriate windowing function to select one or the other of these regions, then converting the signal back into the frequency domain using the Fourier transform about both  $t_1$  and  $t_3$ . It is important to note that both rephasing and nonrephasing must contain  $t_3 = 0$  when performing this apodization, otherwise the projection-slice theorem will cause a dramatic distortion of the spectrum.

A demonstration of the phase control capabilities with the pulse shaper is shown in figure 2.5. The interferogram generated by dispersing the pulse pair on a spectrometer is shown as a function of the delay between the pulses for a series of different relative phases between the pulses. The comparison between the measured interferograms and the interferograms calculated from a simple model shows strong agreement, which confirms that the pulse pair is being generated and controlled correctly.

## Chapter 3

# Measuring Correlated Electronic and Vibrational Spectral Dynamics Using Line Shapes

### 3.1 Introduction

Ultrafast multi-dimensional spectroscopies have been developed into highly effective techniques for studying the dynamics of molecules in condensed phases. The most prevalent of these techniques, two-dimensional electronic spectroscopy (2DES) and two-dimensional infrared spectroscopy (2DIR), are capable of characterizing the transition frequency fluctuations of electronic or vibrational degrees of freedom.[87, 17, 95, 75, 182] In particular, certain parameters of the lineshapes of the resulting correlation spectra, such as the ellipticity of a feature or the slope of the center line, have been shown to be directly related to the frequency-frequency correlation function for the relevant degrees of freedom.[99, 145, 101, 100] Recently we have developed a two color spectroscopic technique that combines the advantages of electronic and vibrational spectroscopies and provides new information by correlating these disparate degrees of freedom, an experiment that we have termed 2D electronic-vibrational spectroscopy (2DEV).[127] This technique directly measures the cross peak that would occur between the 2DES and 2DIR spectra, which provides information about the coupling between the electronic and vibrational degrees of freedom.

As was discussed in chapter 2, the 2DEV experiment utilizes a sequence of three laser pulses, with controlled time delays between each interaction. The first two pulses are resonant with an electronic transition, while the third pulse is resonant with a fundamental vibrational transition. Following the first pulse the system evolves for the time period  $t_1$  according to an electronic coherence, which encodes the initial electronic transition frequency of the system. The second pulse then causes the system to evolve according to a population, either on the excited or ground electronic state, for the waiting time  $t_2$ . During this period the system undergoes spectral diffusion by interacting with the bath and due to microscopic

changes in specific solvent-solute interactions. The third pulse subsequently probes the changes that have occurred during  $t_2$  by causing the system to once again evolve according to a coherence, which radiates the third-order signal as a function of the third time delay  $t_3$ . Because the third pulse is resonant with a vibrational transition, however, the changes that are probed are those that are directly correlated to this vibration, isolating only these components of the frequency-frequency correlation function. The signal field is measured by interfering it with a local oscillator on a spectrometer, which provides the transition frequency of the final vibrational state that results from the evolution during  $t_2$ . In typical 2DES and 2DIR experiments all three laser pulses are degenerate, and therefore they primarily interrogate diagonal features, for which the same correlation function describes the coherence dephasing during  $t_1$  and  $t_3$  and the spectral diffusion during  $t_2$ , and cross peaks between nearby transitions, which typically have similar interactions with the bath. For the 2DEV experiment, the dynamics instead report on the correlation between these disparate aspects of the system.

2DEV is still a new technique, and, as discussed in chapter 1, it has shown promise by revealing simultaneous dynamics of the electronic and vibrational states following an electronic excitation, showing the dynamic Stokes shifts for both these degrees of freedom in the laser dye 4-(di-cyanomethylene)-2-methyl-6-p-(dimethylamino)styryl-4H-pyran (DCM).[127] The physical quantities that 2DEV is particularly suited for measuring have not yet been fully determined, nor how these effects manifest in the spectra. In a separate work we discuss in general terms what types of correlations in both the homogeneous and the inhomogeneous line broadening mechanisms are expected to contribute to the spectra, and show that the slope of the nodal line between the features corresponding to  $t_2$  evolution on the electronic ground and excited states is sensitive to these correlations.[43] In this chapter we focus on extracting quantitative information about the solvation correlation function and the strength of the coupling between the system and its bath. In this case the system is the laser dye 3,3'-diethylthiatricarbocyanine iodide (DTTCI) dissolved in deuterated chloroform ( $\text{CDCl}_3$ ).

Specifically, we investigate the properties of a model composed of a two-level electronic system, with the ground and first excited levels of a single vibration treated explicitly on both the ground and excited electronic states. The level diagram for the model is illustrated in Figure (3.1.a). The electronic and vibrational degrees of freedom are allowed to interact with separate baths, each described by its own spectral density. Within this simple four-level model we will show how the component of the frequency fluctuations that is correlated between the electronic and vibrational degrees of freedom is directly related to the correlation function for the vibrational degree of freedom. This is due to the effect that fluctuations in the vibrational zero point energy on the electronic excited state has on the electronic transition. We will demonstrate that this can be directly measured via the dynamics in the center line slope of a feature in the 2DEV spectrum. Indeed, the center line slope is sensitive to both the dynamical homogeneous component of the correlations (i.e. correlations in the bath-induced fluctuations) as well as any static inhomogeneous distribution in the transition frequencies that is correlated between the electronic and vibrational degrees of freedom.

Finally, we present experimental results that demonstrate these dynamical correlations



via the relaxation of the center line slope. Furthermore, we corroborate our model by showing the dynamics are the same as the vibrational dephasing time, as directly measured from the perturbed free induction decay of the vibrational coherence. The center line slope is also used to extract the strength of the coupling to the bath of the vibration on the excited electronic state relative to that of the vibration on the ground electronic state. This is a parameter that 2DEV is particularly suited to measure, and represents the unique strength of this technique in studying the coupling between electronic and vibrational degrees of freedom.

## 3.2 Theoretical

### 3.2.1 Model

We consider a simple model for a dye molecule in solution composed of two electronic levels and one explicit vibrational degree of freedom, with these electronic and nuclear degrees of freedom each coupled to their own bath. The system will interact first with two visible fields, where we assume the visible fields excite the red edge of the electronic transition, and subsequently with an infrared field resonant with the vibrational transition. This allows us to consider only the ground and first excited vibrational levels on each electronic state. The Hamiltonian for our system, written in units such that  $\hbar = 1$ , is

$$H = H_{g0} |g0\rangle \langle g0| + H_{g1} |g1\rangle \langle g1| + H_{e0'} |e0'\rangle \langle e0'| + H_{e1'} |e1'\rangle \langle e1'| \quad (3.1)$$

where the terms in the Hamiltonian are

$$\begin{aligned} H_{g0} &= \sum_{\xi} \omega_{\xi} a_{\xi}^{\dagger} a_{\xi} + \sum_j \nu_j b_j^{\dagger} b_j, \\ H_{g1} &= \omega_g + \sum_{\xi} \omega_{\xi} a_{\xi}^{\dagger} a_{\xi} \\ &\quad + \sum_j \nu_j \left[ b_j^{\dagger} b_j + h_j (b_j^{\dagger} + b_j) \right], \\ H_{e0'} &= \epsilon_{eg} + \sum_{\xi} \omega_{\xi} \left[ a_{\xi}^{\dagger} a_{\xi} + d_{\xi} (a_{\xi}^{\dagger} + a_{\xi}) \right] \\ &\quad + \sum_j \nu_j \left[ b_j^{\dagger} b_j + \alpha_0 h_j (b_j^{\dagger} + b_j) \right], \\ H_{e1'} &= \epsilon_{eg} + \omega_e + \sum_{\xi} \omega_{\xi} \left[ a_{\xi}^{\dagger} a_{\xi} + d_{\xi} (a_{\xi}^{\dagger} + a_{\xi}) \right] \\ &\quad + \sum_j \nu_j \left[ b_j^{\dagger} b_j + \alpha_1 h_j (b_j^{\dagger} + b_j) \right]. \end{aligned} \quad (3.2)$$

Here,  $a_{\xi}^{\dagger}$  and  $b_j^{\dagger}$  ( $a_{\xi}$  and  $b_j$ ) are the creation (annihilation) operators for the bath degrees of freedom for the electronic and vibrational modes, respectively. The constants  $\epsilon_{eg}$ ,  $\omega_g$

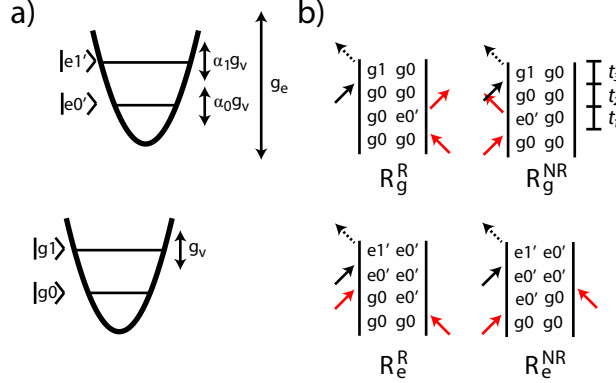


Figure 3.1: a) A schematic representation of the energy level structure of the hamiltonian. The states are labeled with the electronic state and the number of quanta in the vibration (here we will only allow  $v = 0$  or  $1$ ). The double-headed arrows represent the bath induced fluctuations and are labeled with the line shape functions that describe how the states fluctuate relative to  $|g0\rangle$  due to system-bath interactions. b) Double sided Feynman diagrams for the pathways considered in this work. The red arrows represent interactions resonant with visible photons and the black arrows represent interactions with infrared photons. The labels represent the rephasing ( $R^R$ ) and nonrephasing ( $R^{NR}$ ) pathways, evolving on the ground ( $R_g$ ) or excited ( $R_e$ ) electronic state during  $t_2$ .

and  $\omega_e$  represent the transition frequencies for the electronic transition and for the 0-1 vibrational transitions on the ground and excited electronic states. The system-bath coupling is described by  $d_\xi$  for the electronic states and  $h_j$  for the vibration, for the  $\xi$ th or  $j$ th bath modes. The parameters  $\alpha_0$  and  $\alpha_1$  characterize the strength with which the ground and first excited vibrational levels on the electronic excited state couple to the bath, scaled relative to the strength of the coupling to the bath for the vibration on the ground electronic state.

It is important to note that neither electronic nor vibrational relaxation is included. We assume that the visible field will only excite the electronic transition between the  $v = 0$  vibrational levels of the probed vibration, and so the only contribution of the finite vibrational lifetime will be in its effects on the line width for the vibrational transition. If such lifetime broadening is not a major component of the vibrational line width, as expected for high frequency modes, then this approximation should not significantly affect the results. The effect of electronic relaxation will be to cause the signal to decay with waiting time  $t_2$ , which has no significant effect on the properties of the spectra that are the focus of this work.

Typically, it is convenient to reframe the system-bath coupling in terms of the spectral density, which here is given as  $\mathcal{J}_e(\omega) = \sum_\xi d_\xi^2 \omega_\xi^2 \delta(\omega - \omega_\xi)$  for the electronic transition, and likewise  $\mathcal{J}_v(\omega) = \sum_j h_j^2 \nu_j^2 \delta(\omega - \nu_j)$  for the vibration. The parameters  $\alpha_0$  and  $\alpha_1$  are used to denote how the vibration-bath coupling, i.e. the spectral density  $\mathcal{J}_v(\omega)$ , is rescaled on the electronic excited state. Within the current model this is independent of the bath mode, and so it corresponds to a rescaling of the reorganization energy by a factor of  $\alpha_0^2$  and  $\alpha_1^2$  for the

0 and 1 vibrational levels on the electronic excited state. In general, these parameters are complicated to determine, and they likely depend on a large number of molecular parameters, such as the electronic dipole moment, the polarizability of the environment and the transition dipole of the vibration.[104, 123]

In the current model we neglect explicit correlation between the fluctuations of the electronic and vibrational levels. In other words, we assume completely independent baths for these different kinds of states. In general we expect this to be a reasonable approximation, as the electronic transition will typically couple more strongly to fluctuations on a shorter time scale than vibrational transitions. A detailed consideration of explicit correlation between these degrees of freedom is beyond the scope of this work.

The response functions for this model can be derived using typical cumulant expansion methods.[43, 120, 28, 74] The four Liouville pathways that are considered in this work are illustrated in Figure (3.1.b). The rephasing pathways are denoted  $R_g^R(t_1, t_2, t_3)$ ,  $R_e^R(t_1, t_2, t_3)$  where the subscript indicates the electronic state populated during  $t_2$ . Likewise, the non-rephasing pathways are given as  $R_g^{NR}(t_1, t_2, t_3)$ ,  $R_e^{NR}(t_1, t_2, t_3)$ , and the total response is given by the sum of all four terms. They are as follows:

$$\begin{aligned}
 R_g^R(t_1, t_2, t_3) &= \langle \mu_{eg}^2 \mu_{10}^2 \rangle \exp [i\epsilon_{eg}t_1 - i\omega_g t_3] \\
 &\quad \times \exp \left[ -g_e^*(t_1) - \alpha_0^2 g_v^*(t_1) - g_v(t_3) \right. \\
 &\quad \left. + \alpha_0 f_v^{-*}(t_1, t_2, t_3) \right], \\
 R_e^R(t_1, t_2, t_3) &= -\langle \mu_{eg}^2 \mu_{1'0'}^2 \rangle \exp [i\epsilon_{eg}t_1 - i\omega_e t_3] \\
 &\quad \times \exp \left[ -g_e^*(t_1) - \alpha_0^2 g_v^*(t_1) - (\alpha_1 - \alpha_0)^2 g_v(t_3) \right. \\
 &\quad \left. + \alpha_0(\alpha_1 - \alpha_0) f_v^{+*}(t_1, t_2, t_3) \right], \\
 R_g^{NR}(t_1, t_2, t_3) &= \langle \mu_{eg}^2 \mu_{10}^2 \rangle \exp [-i\epsilon_{eg}t_1 - i\omega_g t_3] \\
 &\quad \times \exp \left[ -g_e(t_1) - \alpha_0^2 g_v(t_1) - g_v(t_3) \right. \\
 &\quad \left. - \alpha_0 f_v^-(t_1, t_2, t_3) \right], \\
 R_e^{NR}(t_1, t_2, t_3) &= -\langle \mu_{eg}^2 \mu_{1'0'}^2 \rangle \exp [-i\epsilon_{eg}t_1 - i\omega_e t_3] \\
 &\quad \times \exp \left[ -g_e(t_1) - \alpha_0^2 g_v(t_1) - (\alpha_1 - \alpha_0)^2 g_v(t_3) \right. \\
 &\quad \left. - \alpha_0(\alpha_1 - \alpha_0) f_v^+(t_1, t_2, t_3) \right],
 \end{aligned} \tag{3.3}$$

where the auxiliary functions are defined as

$$\begin{aligned}
 f^+(t_1, t_2, t_3) &= g^*(t_2) - g^*(t_2 + t_3) \\
 &\quad - g(t_1 + t_2) + g(t_1 + t_2 + t_3), \\
 f^-(t_1, t_2, t_3) &= g(t_2) - g(t_2 + t_3) \\
 &\quad - g(t_1 + t_2) + g(t_1 + t_2 + t_3).
 \end{aligned} \tag{3.4}$$

The subscripts  $e$  and  $v$  on the line shape functions indicate whether it corresponds to the electronic or vibrational degrees of freedom. The pre-factors depend on the transition dipole

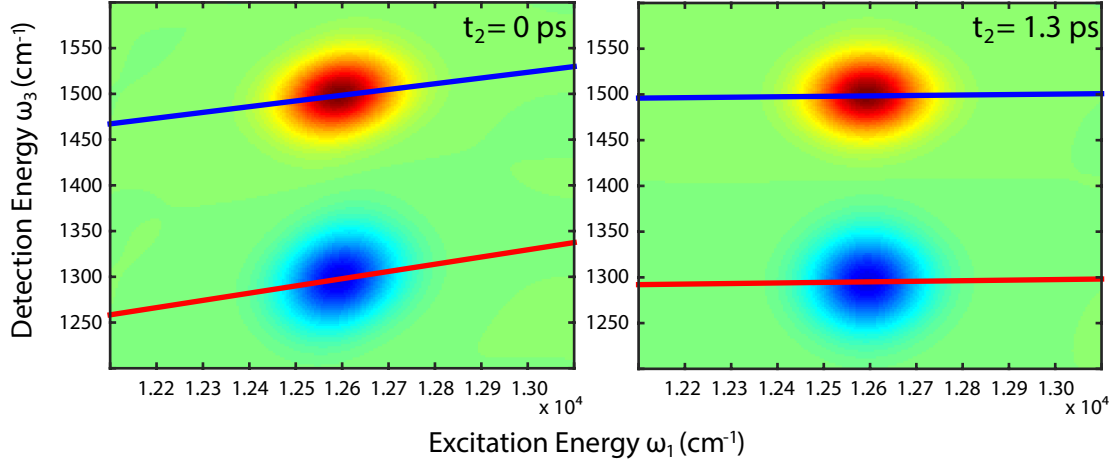


Figure 3.2: Simulated purely absorptive 2DEV spectra using the exact response functions in equation (3.3) with the center lines superimposed. The positive-going (red) features correspond to the vibration on the electronic ground state and the negative-going (blue) features correspond to the vibration on the electronic excited state. The details of this simulation are given in the text.

moment for the electronic transition  $\mu_{eg}$  and for the vibrational transitions  $\mu_{10}$  and  $\mu_{1'0'}$  on the ground or excited electronic states, and here the angled brackets indicate orientational averaging. The line broadening functions are given by

$$g(t) = -i\lambda t + \int_0^\infty d\omega \frac{\mathcal{J}(\omega)}{\omega^2} \coth\left(\frac{\omega\beta}{2}\right) (1 - \cos\omega t) + i \int_0^\infty d\omega \frac{\mathcal{J}(\omega)}{\omega^2} \sin\omega t, \quad (3.5)$$

where  $\mathcal{J}(\omega)$  is the spectral density for the electronic or vibrational degrees of freedom and  $\beta$  is the Boltzmann inverse temperature. The solvent reorganization energy is given by  $\lambda = \int_0^\infty d\omega \frac{\mathcal{J}(\omega)}{\omega}$  and is determined separately for the electronic and vibrational states by relevant spectral densities.

In the impulsive limit, the frequency domain 2D spectra  $S(\omega_1, t_2, \omega_3)$  for each term in the total response function can be obtained by taking the Fourier transform over  $t_1$  and  $t_3$ , and the total purely absorptive correlation spectrum, here referred to as  $S^{abp}$ , is obtained by combining the rephasing and nonrephasing components and taking the real part as  $S^{abp}(\omega_1, t_2, \omega_3) = \text{Re} [S^R(-\omega_1, t_2, \omega_3) + S^{NR}(\omega_1, t_2, \omega_3)]$ . Spectra simulated using this method are shown in Figure (3.2). For this simulation the spectral densities are chosen to be Drude-Lorentian, which has the form  $\mathcal{J}(\omega) = \frac{2\lambda\omega_c\omega}{\omega_c^2 + \omega^2}$ . The purpose of this simulation is not to reproduce the experimental results shown later, but to illustrate the main features of the 2DEV spectra for parameters similar to those typically used for the type of cyanine dye studied in the current experiments.[135] For the electronic degrees of freedom the cutoff

frequency  $\omega_{ce} = 50 \text{ cm}^{-1}$  and the reorganization energy  $\lambda_e = 50 \text{ cm}^{-1}$  and for the vibrational degrees of freedom  $\omega_{cv} = 10 \text{ cm}^{-1}$  and  $\lambda_v = 5 \text{ cm}^{-1}$ . The parameters scaling the strength of the coupling to the bath on the electronic excited state are set to  $\alpha_0 = 0.6$  and  $\alpha_1 = 1.8$ , the frequency of the vibration on the ground electronic state is  $\omega_g = 1500 \text{ cm}^{-1}$ , the frequency of the vibration on the electronic excited state is  $\omega_e = 1300 \text{ cm}^{-1}$  and the electronic transition frequency is  $\epsilon_{eg} = 12600 \text{ cm}^{-1}$ . The transition dipoles  $\mu_{10}$  and  $\mu_{1'0'}$  are taken to be the same. Of particular note is the slope of the center lines that are shown in the figure. At early  $t_2$  the slope is positive, due to the correlation between the fluctuations of the electronic and vibrational transitions. After a few picoseconds, however, the slope decays to zero, due to the decay of the correlation function. In the following section an analytical form for the center line slope is derived.

### 3.2.2 Center Line Slope

The derivation is based on a short time approximation of the response for the time periods  $t_1$  and  $t_3$ . [99, 137, 100, 101, 145] The dephasing times for the electronic coherence during  $t_1$  and the vibrational coherence during  $t_3$  are typically short ( $\sim 100 \text{ fs}$  -  $\sim 1 \text{ ps}$ ) compared to the typical electronic population relaxation times during  $t_2$  ( $\sim 100 \text{ ps}$  -  $\sim 1 \text{ ns}$ ), so we can perform a Taylor expansion of these variables in equations (3.4) and (3.5) and truncate to second-order. Following this procedure we obtain

$$\begin{aligned} f^+(t_1, t_2, t_3) &= 2it_3 (L^{(1)}(t_2) - \lambda) \\ &\quad + i(t_1 + t_3)t_3 \frac{dL^{(1)}(t_2)}{dt} + t_1 t_3 L^{(2)}(t_2), \\ f^-(t_1, t_2, t_3) &= t_1 t_3 \left( L^{(2)}(t_2) + i \frac{dL^{(1)}(t_2)}{dt} \right) \end{aligned} \quad (3.6)$$

and

$$g(t) = \frac{1}{2} \Omega^2 t^2 \quad (3.7)$$

where

$$\begin{aligned} L^{(1)}(t) &\equiv \int_0^\infty d\omega \frac{\mathcal{J}(\omega)}{\omega} \cos \omega t \\ L^{(2)}(t) &\equiv \int_0^\infty d\omega \mathcal{J}(\omega) \coth \left( \frac{\omega\beta}{2} \right) \cos \omega t \\ \Omega^2 &\equiv \int_0^\infty d\omega \mathcal{J}(\omega) \coth \left( \frac{\omega\beta}{2} \right). \end{aligned} \quad (3.8)$$

Here  $L^{(1)}(t)$  is the solvation correlation function and  $\Omega^2$  is the mean square fluctuation of the transition frequency for the relevant degrees of freedom. The functions  $L^{(1)}(t)$  and  $L^{(2)}(t)$  are related by the fluctuation dissipation theorem.  $L^{(1)}(t)$  describes the bath induced dissipation,

and  $L^{(2)}(t)$  describes the fluctuations.[164] If  $L^{(1)}(t)$  is a slowly varying function, then we can neglect the terms that involve  $dL^{(1)}(t)/dt$  and further simplify equation (3.6) to obtain

$$\begin{aligned} f^+(t_1, t_2, t_3) &= 2it_3 (L^{(1)}(t_2) - \lambda) + t_1 t_3 L^{(2)}(t_2), \\ f^-(t_1, t_2, t_3) &= t_1 t_3 L^{(2)}(t_2). \end{aligned} \quad (3.9)$$

This approximation is reasonable for the absorptive (real) part of the spectrum when the solvation correlation function is over-damped, and at high temperatures.[99] The validity of these approximations, for the parameter regime considered in this work, are illustrated with an example simulation in Figure (3.3).

Together, using equations (3.7) and (3.9), the response functions in equation (3.3) can be simplified to

$$\begin{aligned} R_g^R(t_1, t_2, t_3) &= \langle \mu_{eg}^2 \mu_{10}^2 \rangle \\ &\quad \times \exp[i\epsilon_{eg}t_1 - i\omega_g t_3] \\ &\quad \times \exp\left[-\frac{1}{2}At_1^2\right] \times \exp\left[-\frac{1}{2}B_g t_3^2\right] \\ &\quad \times \exp[-C_g(t_2)t_1 t_3], \\ R_e^R(t_1, t_2, t_3) &= -\langle \mu_{eg}^2 \mu_{1'0'}^2 \rangle \\ &\quad \times \exp[i\epsilon_{eg}t_1 - i(\omega_e + \Delta\omega_e(t_2))t_3] \\ &\quad \times \exp\left[-\frac{1}{2}At_1^2\right] \times \exp\left[-\frac{1}{2}B_e t_3^2\right] \\ &\quad \times \exp[-C_e(t_2)t_1 t_3], \\ R_g^{NR}(t_1, t_2, t_3) &= \langle \mu_{eg}^2 \mu_{10}^2 \rangle \\ &\quad \times \exp[-i\epsilon_{eg}t_1 - i\omega_g t_3] \\ &\quad \times \exp\left[-\frac{1}{2}At_1^2\right] \times \exp\left[-\frac{1}{2}B_g t_3^2\right] \\ &\quad \times \exp[C_g(t_2)t_1 t_3], \\ R_e^{NR}(t_1, t_2, t_3) &= -\langle \mu_{eg}^2 \mu_{1'0'}^2 \rangle \\ &\quad \times \exp[-i\epsilon_{eg}t_1 - i(\omega_e + \Delta\omega_e(t_2))t_3] \\ &\quad \times \exp\left[-\frac{1}{2}At_1^2\right] \times \exp\left[-\frac{1}{2}B_e t_3^2\right] \\ &\quad \times \exp[C_e(t_2)t_1 t_3], \end{aligned} \quad (3.10)$$

where

$$\Delta\omega_e(t) \equiv 2\alpha_0 (\alpha_1 - \alpha_0) (L_v^{(1)}(t) - \lambda_v) \quad (3.11)$$

is the dynamic Stokes shift for the vibrational transition on the electronic excited state and we have defined

$$\begin{aligned}
 A &\equiv \Omega_e^2 + \alpha_0 \Omega_v^2, \\
 B_g &\equiv \Omega_v^2, \\
 B_e &\equiv (\alpha_1 - \alpha_0)^2 \Omega_v^2, \\
 C_g(t_2) &\equiv -\alpha_0 L_v^{(2)}(t_2), \\
 C_e(t_2) &\equiv -\alpha_0 (\alpha_1 - \alpha_0) L_v^{(2)}(t_2)
 \end{aligned} \tag{3.12}$$

to simplify the notation. These terms correspond to the different origins of the overall line shape, where  $A$  is the component for the electronic transition, and  $B_g$  and  $B_e$  are the pure vibrational components on the ground and excited electronic states. The most interesting terms are  $C_g(t_2)$  and  $C_e(t_2)$ , which are the components of the line shape that are correlated between the electronic and vibrational degrees of freedom. Within the current approximations  $A$ ,  $B_g$  and  $B_e$  are static components of the line shape, whereas  $C_g(t_2)$  and  $C_e(t_2)$  evolve with  $t_2$ , decaying proportionally to the vibrational correlation function  $L_v^{(2)}(t_2)$ .

The Fourier transforms over  $t_1$  and  $t_3$  can be performed analytically for the form of the response functions given in equation (3.10) to provide:

$$\begin{aligned}
 S_g^{abp}(\omega_1, t_2, \omega_3) &= \frac{2 \langle \mu_{eg}^2 \mu_{10}^2 \rangle}{(AB_g - (C_g(t_2))^2)^{1/2}} \\
 &\times \exp \left[ \frac{\left( \begin{aligned} &-A(\omega_3 - \omega_g)^2 - B_g(\epsilon_{eg} - \omega_1)^2 \\ &- 2C_g(t_2)(\epsilon_{eg} - \omega_1)(\omega_g - \omega_3) \end{aligned} \right)}{2AB_g - 2(C_g(t_2))^2} \right], \\
 S_e^{abp}(\omega_1, t_2, \omega_3) &= \frac{-2 \langle \mu_{eg}^2 \mu_{1'0'}^2 \rangle}{(AB_e - (C_e(t_2))^2)^{1/2}} \\
 &\times \exp \left[ \frac{\left( \begin{aligned} &-A(\omega_e + \Delta\omega_e(t_2) - \omega_3)^2 - B_e(\epsilon_{eg} - \omega_1)^2 \\ &- 2C_e(t_2)(\epsilon_{eg} - \omega_1)(\omega_e + \Delta\omega_e(t_2) - \omega_3) \end{aligned} \right)}{2AB_e - 2(C_e(t_2))^2} \right].
 \end{aligned} \tag{3.13}$$

The complete spectrum is obtained by adding the contributions from the ground and excited electronic states.

At early  $t_2$ , the fluctuations in the electronic and vibrational degrees of freedom are correlated through the fluctuations of the vibrations on the electronic excited state. This has the effect of making the slope of the center lines of each feature non-zero. To evaluate the dynamics of the center line slopes, we can determine an analytic form as a function of  $t_2$ . To do this we differentiate the real (absorptive) part of the spectrum with respect to  $\omega_3$ ,

which is then set to 0 and can be solved to give  $\omega_g'$  and  $\omega_e'$ , the maxima in  $\omega_3$  as a function of  $\omega_1$ , parameterized by  $t_2$

$$\begin{aligned}\omega_g'(\omega_1, t_2) &= k_g(t_2)(\omega_1 - \epsilon_{eg}) + \omega_g \\ \omega_e'(\omega_1, t_2) &= k_e(t_2)(\omega_1 - \epsilon_{eg}) + \omega_e + \Delta\omega_e(t_2)\end{aligned}\tag{3.14}$$

where the slopes of the center lines are given by

$$\begin{aligned}k_g(t_2) &= \frac{\alpha_0 L_v^{(2)}(t_2)}{\Omega_e^2 + \alpha_0 \Omega_v^2}, \\ k_e(t_2) &= \frac{\alpha_0(\alpha_1 - \alpha_0) L_v^{(2)}(t_2)}{\Omega_e^2 + \alpha_0 \Omega_v^2},\end{aligned}\tag{3.15}$$

and so the center line slopes for both the ground ( $k_g$ ) and excited ( $k_e$ ) electronic states are directly proportional to  $L_v^{(2)}(t_2)$ . Furthermore, we can take the ratio

$$\frac{k_e(t_2)}{k_g(t_2)} = (\alpha_1 - \alpha_0)\tag{3.16}$$

and therefore if it is possible to separately measure  $k_g$  and  $k_e$  for the same vibrational mode, then these can be used to provide an approximation for the strength with which the vibrational transition on the electronic excited state couples to its bath. The dynamics for the center line slope extracted from simulated spectra are shown in Figure (3.3) comparing the center line slope for the exact response function with the short time approximation and the analytical result in equation (3.15).

In the presence of inhomogeneous broadening, a result analogous to equation (3.16) can be obtained. To determine this we allow the transition energies  $\epsilon_{eg}$ ,  $\omega_g$  and  $\omega_e$  to be described by a joint Gaussian distribution function, such as

$$\begin{aligned}p(\epsilon_{eg}, \omega_g) &= \frac{1}{2\pi\sigma_{eg}\sigma_{\omega_g}\sqrt{1-\zeta^2}} \\ &\times \exp\left[-\frac{(\epsilon_{eg} - \epsilon_{eg}^0)^2}{2(1-\zeta^2)\sigma_{eg}^2} - \frac{(\omega_g - \omega_g^0)^2}{2(1-\zeta^2)\sigma_{\omega_g}^2} + \frac{\zeta(\epsilon_{eg} - \epsilon_{eg}^0)(\omega_g - \omega_g^0)}{(1-\zeta^2)\sigma_{eg}\sigma_{\omega_g}}\right]\end{aligned}\tag{3.17}$$

where  $\zeta$  is a correlation factor between the distributions of electronic and vibrational transition frequencies that is 0 when there is no correlation,  $\zeta > 0$  for positive correlation and  $\zeta < 0$  for negative correlation. The widths of the inhomogeneous distribution is given by  $\sigma_{eg}$  for the electronic transition, and by  $\sigma_{\omega_g}$  and  $\sigma_{\omega_e}$  for the vibrational transitions on the ground and excited electronic states. The effects that would result in this type of correlated frequency distribution have been described theoretically,[27, 71] and the effect of an inhomogeneous distribution with this form is discussed at greater length elsewhere.[43] The effect of this inhomogeneous broadening on the spectrum can be obtained by integrating  $S^{abp}(\omega_1, t_2, \omega_3)$



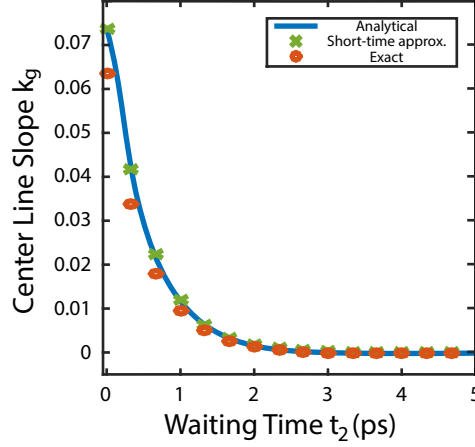


Figure 3.3: The center-line slope of the ground state feature for the model shown in Figure (3.2). The solid blue line shows the analytical result from equation (3.15), the green crosses show the result for the calculation with the short-time approximation without the further approximation in equation (3.9) and the red circles show the result for the calculation using the exact response functions in equation (3.3). The small discrepancy between the exact result and the analytical result comes from the relatively long vibrational dephasing and the short-time approximation. The discrepancy decreases as  $\lambda_v$  is increased.

over this distribution, after which  $\tilde{k}_g$  and  $\tilde{k}_e$ , the center line slopes with inhomogeneous broadening included, can be found in the same manner as before:

$$\begin{aligned}\tilde{k}_g(t_2) &= \frac{\alpha_0 L_v^{(2)}(t_2) + \zeta \sigma_{eg} \sigma_{\omega_g}}{(\Omega_e^2 + \alpha_0 \Omega_v^2) + \sigma_{eg}^2}, \\ \tilde{k}_e(t_2) &= \frac{\alpha_0(\alpha_1 - \alpha_0) L_v^{(2)}(t_2) + \zeta \sigma_{eg} \sigma_{\omega_e}}{(\Omega_e^2 + \alpha_0 \Omega_v^2) + \sigma_{eg}^2}.\end{aligned}\tag{3.18}$$

The long-time slope is determined by the widths of the inhomogeneous distribution and the correlation factor, and by subtracting this component and taking the ratio of these slopes we recover the same result as in equation (3.16)

$$\frac{\tilde{k}_e(t_2) - \tilde{k}_e(\infty)}{\tilde{k}_g(t_2) - \tilde{k}_g(\infty)} = (\alpha_1 - \alpha_0).\tag{3.19}$$

If instead of taking the derivative with respect to  $\omega_3$  to find the center-line as a function of  $\omega_1$  we do the reverse, differentiating with respect to  $\omega_1$ , we can find an analogous centerline slope,  $k'$ , defined via the equations

$$\begin{aligned}\omega'_g(\omega_3, t_2) &= k'_g(t_2)(\omega_3 - \omega_g) + \epsilon_{eg} \\ \omega'_e(\omega_3, t_2) &= k'_e(t_2)(\omega_3 - \omega_e - \Delta\omega_e(t_2)) + \epsilon_{eg}.\end{aligned}\tag{3.20}$$

For one-color measurements, where the same degrees of freedom are correlated with themselves after the waiting time  $t_2$ , these slopes are equivalent. Here, because the measurement is of a cross-peak, these slopes are not directly related in this manner, and instead we can find

$$\begin{aligned}\tilde{k}'_g(t_2) &= \frac{\alpha_0 L_v^{(2)}(t_2) + \zeta \sigma_{eg} \sigma_{\omega_g}}{\Omega_v^2 + \sigma_{\omega_g}^2}, \\ \tilde{k}'_e(t_2) &= \frac{\alpha_0(\alpha_1 - \alpha_0) L_v^{(2)}(t_2) + \zeta \sigma_{eg} \sigma_{\omega_e}}{(\alpha_1 - \alpha_0)^2 \Omega_v^2 + \sigma_{\omega_e}^2}.\end{aligned}\tag{3.21}$$

These slopes are somewhat less useful than their counterparts, however, because it is not possible to extract  $(\alpha_1 - \alpha_0)$  as in equation (3.19). In the absence of correlated inhomogeneous broadening, i.e. when either the system is purely homogeneously broadened or  $\zeta = 0$ , if we note that  $L_v^{(2)}(0) = \Omega_v^2$  then we can determine  $\alpha_0$  and  $\alpha_1$  explicitly and find them to be

$$\begin{aligned}\alpha_0 &= k'_g(0) \\ \alpha_1 &= \frac{k'_g(0)}{k'_e(0)} + k'_g(0).\end{aligned}\tag{3.22}$$

Therefore in certain circumstances it can be possible to directly measure the relative strengths with which the vibration couples to the bath on the excited versus the ground electronic states.

Through the derivation of equations (3.16) and (3.22) we have a general analytical procedure which can be used to extract information from 2DEV spectra about the correlated aspects of the line shape, as well as to obtain values for the important parameters  $\alpha_0$ ,  $\alpha_1$  and  $\alpha_1 - \alpha_0$  which describe the strength of the vibrational coupling to the bath on the electronic excited state for a given vibrational mode.

## 3.3 Experimental

### 3.3.1 Methods

The experimental details involved in 2DEV have been described previously,[127] and in chapter 2. Briefly, the experiment was driven by the output of an amplified Ti:Sapphire femtosecond laser system (Coherent; Legend Elite USP; 806 nm, 40 fs, 0.9 mJ, 1 kHz). A portion of this laser ( $\sim 0.2$  mJ) was used to pump a homebuilt mid-IR optical parametric amplifier (OPA), creating 200 nJ pulses centered at 7  $\mu\text{m}$  with a duration of  $\sim 80$  fs.

The pulse pair for the electronic excitation was derived from a small portion of the regenerative amplifier beam. Prior to the sample, the pump was passed through an acousto-optic programmable dispersive filter (Fastlite; Dazzler) which was used to temporally compress the pump to 40 fs at the sample position and to generate a pair of identical pulses with a controlled time delay  $t_1$  and relative phase  $\phi_{12}$ . This pulse pair was then delayed by reflecting it off a retroreflector mounted on a translation stage to control the time delay  $t_2$  between the

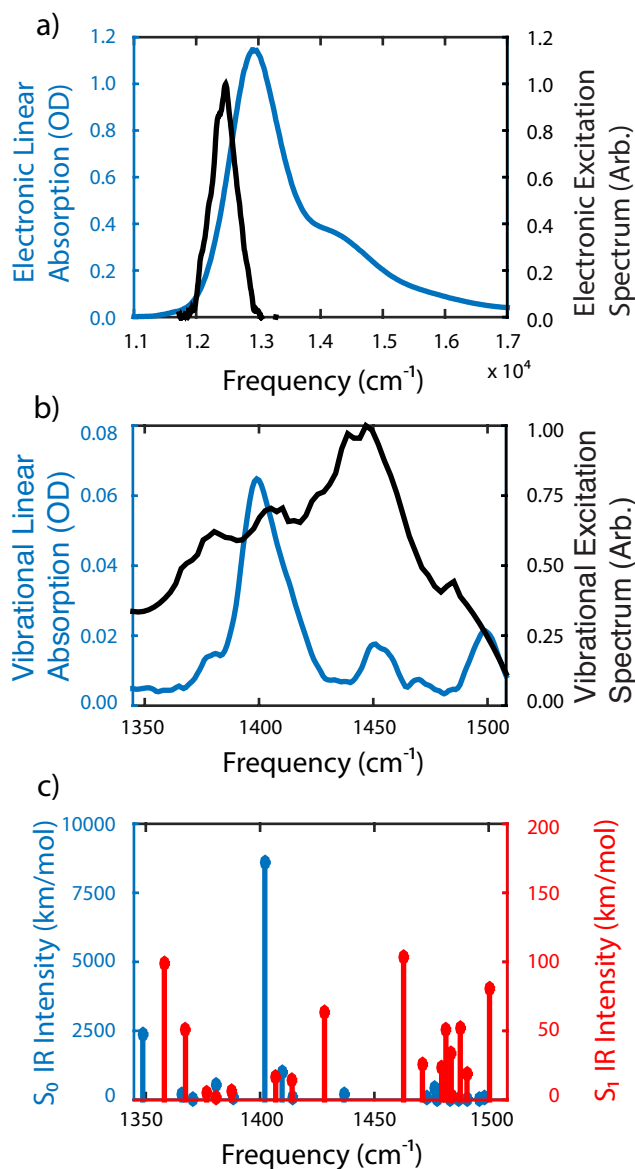


Figure 3.4: (a-b) The linear absorption of DTTCI dissolved in  $\text{CDCl}_3$  at the concentration used in the present experiment is shown in blue. The electronic absorption is shown in a) and the vibrational absorption, with the solvent signal subtracted, is shown in b). In each case the normalized laser spectrum used to excite the relevant transition superimposed in black. c) Stick spectra of the calculated normal mode frequencies and infrared intensities within the probed region calculated for the  $S_0$  (blue) and  $S_1$  (red) electronic states. Note the axes for the two sets of data differ by a factor of 50. In each case the frequencies have been scaled by a factor of 0.98.[4] The details of the calculation are given in the text.

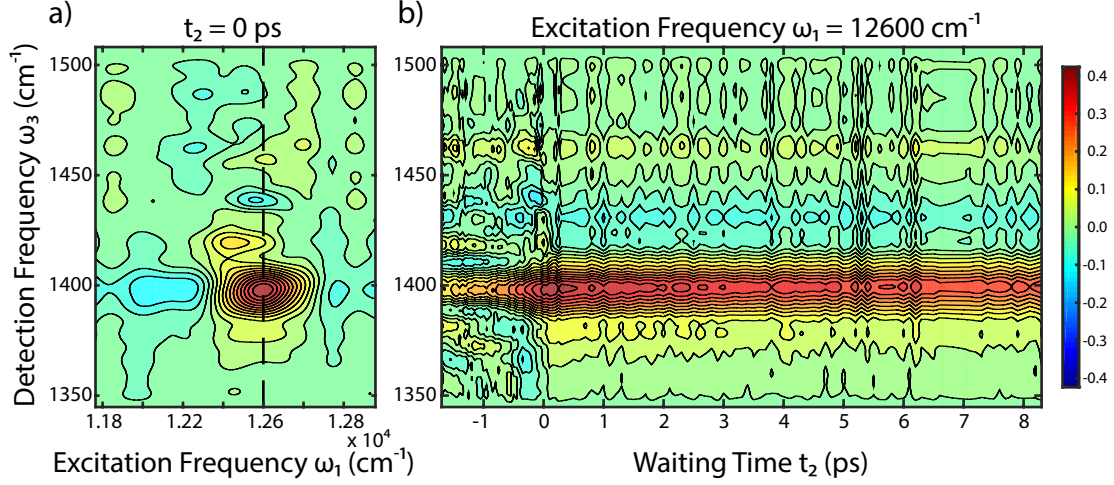


Figure 3.5: a) A purely absorptive 2DEV spectrum of DTTCl at  $t_2 = 0$  ps. The dotted line indicates the slice through the spectrum shown as a function of  $t_2$  in b). For  $t_2 > 0$  the signal at  $\omega_3 = 1400$   $\text{cm}^{-1}$  decays with a time constant of  $\sim 250$  ps. For  $t_2 < 0$  it decays with a time constant of 1.5 ps.

second 800 nm pulse and the 7  $\mu\text{m}$  probe pulse. At the sample, the total power of the pump beam was 100 nJ, focused to a spot size of 250  $\mu\text{m}$  by an  $f = 25$  cm,  $90^\circ$  off-axis parabolic silver mirror. The spectrum of the excitation laser at the sample position is shown in Figure (3.4.a).

Following the OPA, this 7  $\mu\text{m}$  beam was split by a 50:50 ZnSe beam splitter to form the probe and reference beams, which were both focused at the sample to separate 250  $\mu\text{m}$  spots by an  $f = 15$  cm,  $90^\circ$  off-axis parabolic gold mirror. The probe and reference beams were then dispersed in a spectrometer (Horiba; Triax 180) and imaged onto a dual-array HgCdTe detector with 64 elements per array (Infrared Systems Development). The spectrum of the probe laser at the sample position is shown in Figure (3.4.b). The reference beam was used to normalize the probe spectrum, to compensate for shot-to-shot instability in the laser intensity. The probe beam was overlapped in the sample with a small portion of the regenerative amplifier output to serve as the pump. The cross-correlation time between the pump and probe pulses was measured to be  $\sim 90$  fs.

For each waiting time  $t_2$  a 2DEV surface was measured by using the pulse shaper to scan the delay  $t_1$  from 0 fs to 175 fs in 0.875 fs steps. For each value of  $t_1$  the signal was measured with the relative phase  $\phi_{12}$  set to 0,  $\frac{\pi}{4}$ ,  $\frac{\pi}{2}$  and  $\frac{3\pi}{4}$  and the signal was recovered using a  $4 \times 1 \times 1$  phase cycling scheme.[122, 181] The signal was collected in the rotating frame, to remove the optical frequency of the pump from the signal. Because the experiment was performed in a partially collinear geometry (referred to as the pump-probe geometry) it was not necessary to perform a separate phasing procedure to recover the purely absorptive part of the spectrum.[64]

The sample was prepared by dissolving the laser dye DTTCl in  $\text{CDCl}_3$  so that the optical density at the maximum of the electronic transition (760 nm) was 1.2 OD in a 250  $\mu\text{m}$  path length cell, corresponding to 0.4 OD at the wavelength of maximum pump laser intensity (806 nm). Under these conditions  $\sim 9.5\%$  of the molecules in the interaction volume were excited. The vibrational transition had an optical density of  $\sim 0.06$ . The cell was constructed from a pair of  $\text{CaF}_2$  windows separated by a 250  $\mu\text{m}$  teflon spacer, and the sample was continuously flowed to minimize the effects of local heating and photo-induced degradation of the dye. The electronic linear absorption was measured before and after the experiments to ensure the sample did not degrade over the course of the 2DEV measurements. The experiments were performed at ambient temperature. The linear absorption spectra for the electronic and vibrational transitions of the sample, with solvent subtracted, are shown in Figure (3.4.a) and (3.4.b), respectively.

### 3.3.2 Results

A 2DEV spectrum of DTTCl probed near  $1400\text{ cm}^{-1}$  at  $t_2 = 0\text{ ps}$  is shown in Figure (3.5.a). The spectrum is dominated by a single positive-going feature centered at an excitation energy  $12600\text{ cm}^{-1}$  and a detection energy of  $1400\text{ cm}^{-1}$ . This is assigned to the bleaching of the backbone  $\text{C}=\text{C}$  stretch mode on the electronic ground state, based on density functional theory (DFT) calculations using the  $\omega\text{B97XD}$  functional and the 6-311+G(d) gaussian basis set using the Gaussian09 package with a polarizable continuum solvent model with parameters appropriate for chloroform.[58] The corresponding feature for evolution of this mode on the electronic excited state is not observed because of the very small extinction coefficient associated with the vibrational transition on the electronic excited state, as predicted from TDDFT calculations. The calculated vibrational frequencies and infrared activities are shown in Figure (3.4.c). The  $\text{S}_1$  vibrations in the probed region are predicted to have activities  $\sim 100$  times smaller than the  $1400\text{ cm}^{-1}$   $\text{S}_0$  mode.

In addition to the primary resonance at  $1400\text{ cm}^{-1}$ , there are several smaller features, including two positive-going peaks, one at  $\omega_3 = 1420\text{ cm}^{-1}$  and the other at  $1455\text{ cm}^{-1}$ , and a negative-going peak at  $\omega_3 = 1440\text{ cm}^{-1}$ . These features correspond to, respectively, ground and excited electronic state vibrations with small vibrational oscillator strength, such as backbone  $\text{C}-\text{H}$  wag modes. Additionally there is a small amplitude negative-going peak at the same detection frequency as the primary feature but centered at a lower excitation frequency of  $\omega_1 = 12100\text{ cm}^{-1}$ . The origin of this peak is unclear, as it is located past the red-most edge of the DTTCl linear electronic absorption in  $\text{CDCl}_3$ . Due to the low intensity of these peaks the signal to noise ratio is poor, and they will not be considered further.

The dynamics of the spectrum at the frequency of the maximum absorption at  $\omega_1 = 12600\text{ cm}^{-1}$  is shown in Figure (3.5.b) as a function of detection frequency  $\omega_3$  and waiting time  $t_2$ . For  $t_2 > 0\text{ ps}$  the signal of the  $1400\text{ cm}^{-1}$  mode decays with a single time constant of  $\sim 250\text{ ps}$ . This decay is substantially faster than previous studies, which have found the excited state lifetime for the  $\text{S}_1$  state of DTTCl to be 845 ps in ethanol.[69] It is known, however, that chloroform acts as a quencher for electronic excited states,[14, 173] and so the decay we

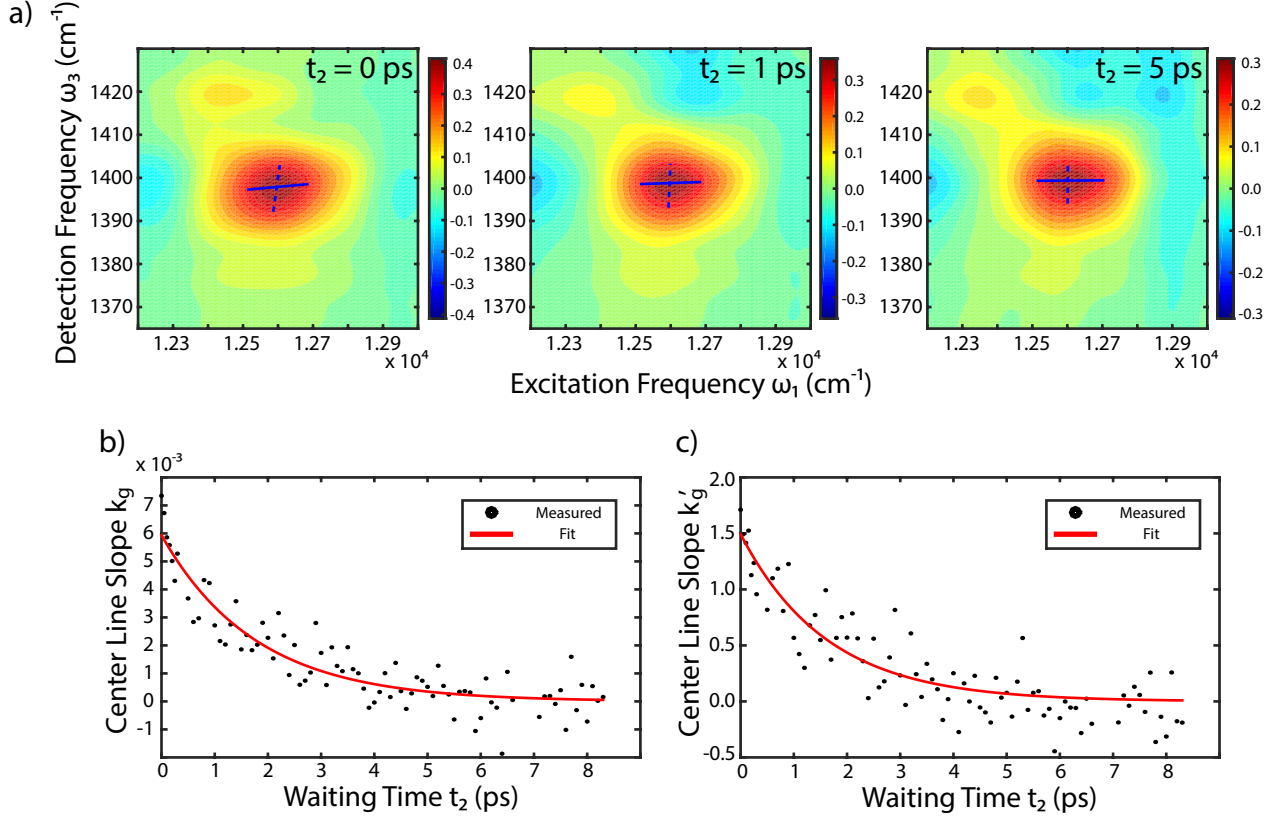


Figure 3.6: a) Purely absorptive 2DEV spectra of the  $1400 \text{ cm}^{-1}$  mode of DTTCl<sub>3</sub> at waiting times  $t_2 = 0, 1$  and  $5$  ps. The center line with respect to  $\omega_3$  is indicated by the solid lines and the center line with respect to  $\omega_1$  is indicated with dashed lines. b) The center line slope with respect to  $\omega_3$ ,  $k_g(t_2)$ , as a function of the waiting time  $t_2$ . The solid red line is the fit of the data to a single exponential, with a lifetime of  $\tau = 1.8$  ps. c) The center line slope with respect to  $\omega_1$ ,  $k'_g(t_2)$ , as a function of the waiting time  $t_2$ . The solid red line is the fit of the data to a single exponential, with a lifetime of  $\tau = 1.6$  ps and an amplitude of  $k'_g(0) = 1.5$ .

observe appears to be consistent with the lifetime of the recovery of the bleach of the ground electronic state vibration, due to electronic relaxation. The central position and width of the  $1400 \text{ cm}^{-1}$  feature in the  $\omega_3$  axis does not change significantly in the first 10 ps following electronic excitation.

For  $t_2 < 0$  ps, the infrared laser excites a vibrational coherence on the ground electronic state which is subsequently perturbed by the 800nm laser, and so the signal corresponds to the perturbed free-induction-decay of the vibrational coherence.[72] This signal is therefore expected to decay with the dephasing time for the vibration. It is observed that the signal intensity decays with a single time constant of 1.5 ps, providing a direct time domain measurement for the dephasing time for this vibration within the current experiment.

Of particular interest are the dynamics of the line shape of the main  $1400\text{ cm}^{-1}$  peak. A series of 2DEV spectra at  $t_2 = 0, 1$  and  $5\text{ ps}$  is shown in Figure (3.6.a), focusing on the dominant feature in the spectrum. The center line slope  $k_g$  for the feature is illustrated with the solid blue lines superimposed on the spectra, while the inverse slope  $k'_g$  is shown with the dashed blue lines. To minimize potential issues with lower signal to noise ratio at the wings of the feature we only consider values greater than the half-maximum. At early  $t_2$  the peak shows a clear ellipticity and diagonal elongation with positive center-line slopes. The decay of the center line slope  $k_g$  is shown in Figure (3.6.b) and the dynamics of  $k'_g$  is shown in (3.6.c). Here we can see that  $k_g$  has an initial value of  $\sim 0.006$  while  $k'_g$  has an initial value of  $\sim 1.5$ . Both slopes decay on a few picosecond timescale. They can be fit to a single exponential with lifetimes of  $\tau = 1.8\text{ ps}$  for  $k_g$  and  $1.6\text{ ps}$  for  $k'_g$ , which are very close (within error) to the vibrational dephasing time found for this vibration from the perturbed free-induction decay. This agreement between the dynamics of  $k_g(t_2)$  and  $k'_g(t_2)$  and the vibrational dephasing time is consistent with the model Hamiltonian and equation (3.15). This provides support for the model discussed in this work, which predicts that these parameters should all decay with the same lifetime.

In both Figures (3.6.b) and (3.6.c) we note the slopes decay completely to 0, with no long time offset. This indicates that the  $1400\text{ cm}^{-1}$  mode of DTTCI is either primarily homogeneously broadened, as would be expected for a dye in solution at room temperature, or that the inhomogeneous broadening is not correlated ( $\zeta = 0$ ). In the former of these scenarios, equation (3.22) is applicable and we can use the fit to estimate  $\alpha_0 = 1.5$ , providing a direct measurement for the relative strength of the bath on the electronic excited state versus the ground state for this mode. The primary sources for error in this estimate come from the approximations made in the derivation of equations (3.18, 3.21), particularly the impulsive limit and the short time approximation. The precise effect of these approximations on the estimate for  $\alpha_0$  have not been fully characterized. The origin of this increase in the strength of the coupling to the bath on the electronic excited state could be explained for example by the increase in the permanent electric dipole moment – from DFT calculations the electric dipole moment increases from  $1.32\text{ D}$  on the ground state to  $1.63\text{ D}$  on the excited state – or other related parameters such as the polarizability.

It is interesting to note that despite analyzing a spectral feature that corresponds to  $t_2$  evolution on the electronic ground state, it is possible to measure  $\alpha_0$ , a parameter that describes the electronic excited state. This is because the dynamics are initiated by an electronic absorption, which depends on  $\alpha_0$  via its effect on the line broadening function for the electronic transition. If we also could measure the center line slope for the excited state feature corresponding to the same nuclear coordinate then it would be possible to measure  $\alpha_1$  for that mode in addition to  $\alpha_0$ . If the system were inhomogeneously broadened then it would not be possible to directly measure  $\alpha_0$  and  $\alpha_1$ , but only the difference. This parameter is still of interest, because it describes the strength of the coupling to the bath of the vibrational transition on the electronic excited state. 2DEV is uniquely capable of measuring these parameters,  $\alpha_0$  and  $\alpha_1$ . This information would be very difficult to extract from a 2DES spectrum, as it would be incorporated as a component of the overall electronic line shape

function. In principle it might be possible to extract the  $\alpha_1 - \alpha_0$  from a combination of 2DIR and transient-2DIR, but to our knowledge this has not been attempted.[15, 115] Indeed, it would likely not be as straight forward as measuring the center line slopes, as these provide the normalized solvation correlation function, whereas  $\alpha_1$  and  $\alpha_0$  are related to the absolute magnitude of the coupling to the bath.

### 3.4 Conclusion

In this chapter we have analyzed the line shape of a 2DEV resonance for a simple model comprised of a two-level electronic system with a single vibration, coupled to a bath. We make use of a short-time approximation to derive an analytical form for the center line slope of a resonance. In particular, we find that the center line slope has a decaying component which is proportional to the vibrational correlation function and a static component that depends on the correlation between the inhomogeneous frequency distributions for the electronic and vibrational transitions. The origin of the dynamic component as the vibrational correlation function comes from the effect that fluctuations in the vibrational zero point energy on the electronic excited state has on the electronic transition frequency.

In addition to the dynamics of the slope, we show that it is possible in certain circumstances to measure the relative strength of the coupling of a vibration to the bath on the electronic excited state relative to the ground state, here referred to as  $\alpha_0$  for the 0 vibrational level and  $\alpha_1$  for the first excited vibrational level. These are unique parameters that the 2DEV spectroscopic technique is particularly suitable for observing, as they are theoretically or practically excluded from being extracted from 2DES or 2DIR spectra. It may be possible to measure these parameters using transient-2DIR, but this would likely depend on a more complicated analytical procedure than that which was been presented here.

We also demonstrate experimentally the validity and practical application of the theoretical results, by showing 2DEV spectra of the  $1400\text{ cm}^{-1}$  mode of the dye DTTCI. Here the center line slope is shown to decay with a time constant of  $\sim 1.7\text{ ps}$ , which is very close to the observed vibrational dephasing time. Furthermore, we are able to directly measure a value for  $\alpha_0$  for the  $1400\text{ cm}^{-1}$  vibration of  $\sim 1.5$ . In other words, on the electronic excited state this vibration couples to the environment about 1.5 times more strongly than the electronic ground state vibration for the same mode.

In this data we only observe the ground electronic state feature of a single vibration. An open question, therefore, is whether the parameters  $\alpha_0$  and  $\alpha_1$  vary within the same molecule for different vibrational modes. Exactly what molecular parameters these values depend on also remains uncertain, and will require further theoretical developments.



## Chapter 4

# A Method for the Direct Measurement of Electronic Site Populations in a Molecular Aggregate

### 4.1 Introduction

Photosynthetic pigment-protein complexes perform a number of distinct tasks, including light harvesting, exciton migration, dissipation of excess energy, and the separation and transfer of charge carriers.[152, 5, 12] They are able to perform these tasks with only a relatively small molecular toolbox, consisting primarily of a variety of chlorin derivatives and carotenoids. Photosynthetic organisms are able to use this small toolbox to significant advantage, tuning the properties towards specific roles. They accomplish this by precisely controlling the spatial organization and the local environments of the pigments to tune the electronic structure of the complex, affecting the electronic energies of each pigment as well as the strength of the coupling between neighboring molecules. These interactions result in varying degrees of delocalization in the electronic excited states and help to guide both the energetic and the spatial dynamics of the electronic excitation energy.

In recent years, two-dimensional electronic spectroscopy (2DES) has become a mature technique for studying electronic dynamics in photosynthetic complexes, as well as other types of molecular aggregates.[65, 117] Much progress towards the understanding of electronic excitation dynamics in these types of systems has been enabled by this technique, with the determination of precise energetic pathways and unraveling of the degree to which electronic coherence may, or may not, determine the rate and efficiency of energy transfer.[103, 49, 88, 138, 133, 34, 132, 147, 62] All of these applications of electronic spectroscopies, however, critically rely on the development of accurate models to provide the link between the electronic energy levels and the spatial character of the states. Typically, these models rely on incomplete information regarding both the electronic and spatial structures of these complexes, and necessitate complicated procedures that aim to optimize the fit to

a number of different, but related, observables, such as the spectral structures in 2DES and various linear spectra.[1, 30, 21, 77] It has been demonstrated that the polarization dependence of 2DES can provide structural information that helps constrain the parameters of the model,[151, 66] but this crucially relies on complex mutant studies to link the excitons with their spatial locations. Imperfections in the model still have substantial ramifications for the results, potentially resulting in an incorrect interpretation of the spatial localization of the excitation due to the difficulty in correctly separating the site energies from the strength of the electronic coupling. The information derived from this model-based approach has been very successfully applied towards the accurate reproduction of experimental observables in even very large and complex systems,[10] and recent developments in highly scalable electronic structure methods show promise in aiding the future refinement of these models.[159] To improve feedback between theory and experiment, however, there is a distinct need for an experimental method capable of directly linking the energetic and spatial domains without need for a model, or the assumptions that this entails.

Electronic spectroscopies, like 2DES, are very useful for understanding energetic structure and dynamics in complicated systems, but they lack a direct connection to spatial information. Alternatively, vibrational spectroscopies are capable of providing structural information, and 2D infrared spectroscopy (2DIR) has become a widespread tool in the study of protein structure and structural dynamics.[52, 74] Pure vibrational spectroscopy does not, however, provide any information about electronic dynamics. The recently developed 2D electronic-vibrational spectroscopy (2DEV) provides a direct link between these two regimes.[127] 2DEV measures the direct correlation between electronic and vibrational degrees of freedom, providing the cross peak between the traditional 2DES and 2DIR spectra. The successful application of 2DEV to the study of molecular aggregates, such as photosynthetic pigment protein complexes, has the potential to provide a direct experimental connection between the energetic and spatial domains of electronic energy transfer that has heretofore been missing.

In this chapter, we propose a method by which 2DEV spectra of a molecular aggregate could be used to directly measure electronic site populations, without need for a model. This method is based on the idea that a localized vibrational mode that is only weakly coupled to the electronic transition of interest could be used as a proxy for spatial location in an extended molecule or aggregate. This idea of using localized vibrations as proxies for position in a molecular aggregate has been used previously in the analysis of visible-infrared pump-probe spectroscopy,[68, 161] and is similar to the idea of using high frequency vibrational modes to monitor conformational dynamics commonly found in the analysis of femtosecond stimulated Raman spectroscopy.[98, 33] The extension of the method to a multidimensional technique, in which both the excitation axis and the detection axis are resolved, allows for much greater detail in the information extracted from the spectra. Indeed, the approach described here not only provides the rates of energy transfer and relaxation, but also, without approximation, enables the extraction of electronic populations in the site basis.

The specific method that we propose in this chapter is not without its flaws, and indeed is not entirely general. It crucially relies on the ability to resolve a spectral feature corre-

sponding to each electronic excited state and a vibration localized on each monomer. In our spectral simulations, the parameters have been chosen to provide an illustrative example. Our goal here is not to provide a fully general analysis method that will work with spectra where these conditions are not met, but rather to demonstrate that in principle the information can be extracted with a relatively straight-forward technique. To this end, it is important to note the distinction between the approximate model we use to provide illustrative simulations, and the method used to extract the information from these approximate spectra, which is not subject to the same approximations.

In this chapter, we extend the response functions developed and discussed in chapter 3 for simulating the 2DEV spectra of a monomer, and successfully applied to the study of correlated electronic and vibrational spectral dynamics and disorder,[43, 108] to the case of a molecular dimer. We then describe how these spectra can be used to directly measure the electronic site populations in a generic molecular aggregate without need for an accompanying model. Finally, we use the response function simulations to provide a numerical demonstration of this method for the dimer case, which shows that the resulting measured populations are exactly equal to those from a direct calculation using a quantum master equation with the same dynamical model.

## 4.2 Model

### 4.2.1 Dimer Hamiltonian

To demonstrate the feasibility of the proposed measurement, we use a simplified model to describe the system. A schematic illustration of this model is shown in figure 4.1. The Hamiltonian for our model is given by

$$H = H^A + H^B + J(|e_A\rangle\langle e_B| + |e_B\rangle\langle e_A|), \quad (4.1)$$

where  $H^A$  and  $H^B$  are the Hamiltonians for the monomers  $A$  and  $B$ ,  $J$  is the electronic coupling, and  $|e_A\rangle$  and  $|e_B\rangle$  are the electronic excited states for the monomers. The monomer Hamiltonians are taken to be the same as in our previous studies of the 2DEV spectra of a solvated dye molecule,[43, 108] and are considered as four-level systems with the form

$$H^M = H_{bath}^M + H_{g1}^M |g_M 1\rangle\langle g_M 1| + H_{e0}^M |e_M 0\rangle\langle e_M 0| + H_{e1}^M |e_M 1\rangle\langle e_M 1|, \quad (4.2)$$

where each of the terms are defined as

$$H_{bath}^M = \hbar \sum_i \omega_i^M a_i^{M\dagger} a_i^M + \hbar \sum_j \nu_j^M b_j^{M\dagger} b_j^M, \quad (4.3)$$

$$H_{g1}^M = \hbar \omega_M + \hbar \sum_j h_j^M \nu_j^M (b_j^{M\dagger} + b_j^M), \quad (4.4)$$

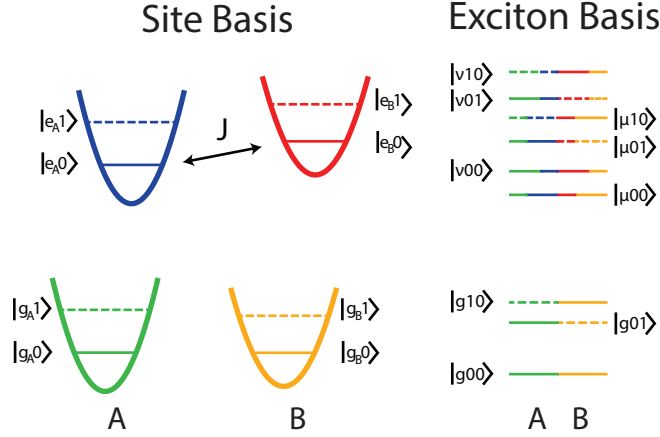


Figure 4.1: A schematic illustration of the model used in this work (energies are not drawn to scale). The electronic ground state is indicated by green for monomer  $A$  and yellow for monomer  $B$ , whereas the electronic excited state is indicated by blue and red, respectively. Solid lines indicate the vibration is on the ground state, while dashed lines indicate the vibration is excited. Note that when one of the excitons is populated, a vibrational excitation can occur with that monomer on either the ground or excited electronic state.

$$H_{e0}^M = \epsilon_M + \hbar \sum_i d_i^M \omega_i^M \left( a_i^{M\dagger} + a_i^M \right) + \hbar \sum_j \alpha_0^M h_j^M \nu_j^M \left( b_j^{M\dagger} + b_j^M \right), \quad (4.5)$$

$$H_{e1}^M = \epsilon_M + \hbar \omega'_M + \hbar \sum_i d_i^M \omega_i^M \left( a_i^{M\dagger} + a_i^M \right) + \hbar \sum_j \alpha_1^M h_j^M \nu_j^M \left( b_j^{M\dagger} + b_j^M \right). \quad (4.6)$$

Here,  $M = A$  or  $B$  labels the monomers. We define  $\epsilon_M$  as the electronic energy gap, while  $\omega_M$  and  $\omega'_M$  are defined as the frequency of the probed vibrational mode when monomer  $M$  is on the ground ( $\omega_M$ ) or excited ( $\omega'_M$ ) electronic state.  $H_{bath}^M$  denotes the Hamiltonian for the environment, and the operators  $a_i^M$  ( $a_i^{M\dagger}$ ) and  $b_j^M$  ( $b_j^{M\dagger}$ ) are the annihilation (creation) operators for the bath degrees of freedom for the electronic and vibrational modes, respectively, which are taken to be harmonic oscillators with frequencies  $\omega_i^M$  and  $\nu_j^M$ . The electronic and vibrational degrees of freedom on each monomer are all assumed to have completely independent baths. The parameters  $d_i^M$  and  $h_j^M$  describe the strength of the system-bath coupling for the electronic and vibrational degrees of freedom. These system-bath coupling components of the Hamiltonian are typically characterized by spectral densities, defined as  $\mathcal{J}_e^M(\omega) = \sum_i d_i^{M2} \omega_i^{M2} \delta(\omega - \omega_i^M)$  and  $\mathcal{J}_v^M(\omega) = \sum_j h_j^{M2} \nu_j^{M2} \delta(\omega - \nu_j^M)$  for the electronic and vibrational levels, respectively. The coupling between the electronic and vibrational system degrees of freedom is included via the change in the frequency of the vibration and the parameters  $\alpha_0^M$  and  $\alpha_1^M$ , which rescale the strength of the vibration-bath coupling due to the electronic excitation.[43, 108] We have shown previously, in chapter 3, how these parameters can be extracted from the 2DEV spectra of a monomer.[108]

In choosing this form for the monomer Hamiltonians, we have made several assumptions and approximations. First of all, we assume that the laser used to drive the electronic transition only excites the fundamental 0-0 transition in the vibration that is being probed, and does not excite higher vibronic transitions, either due to insufficient bandwidth or small Franck-Condon factors. This assumption allows us to consider the monomers as four-level systems, and greatly reduces the number of pathways that must be considered, simplifying the resulting spectra. It also allows us to neglect any displacement in the equilibrium position of the vibration that is probed, the dominant effect of which would be to modify the Franck-Condon factors and shift the oscillator strength of the electronic transition towards higher vibronic transitions. Additionally, we assume that the monomer Hamiltonian is diagonal in the basis  $\{|g_M 0\rangle, |g_M 1\rangle, |e_M 0\rangle, |e_M 1\rangle\}$ , and therefore we neglect relaxation of the electronic and vibrationally excited states. In photosynthetic light harvesting complexes, electronic relaxation to the ground state typically occurs on a much longer timescale ( $\sim 100$  ps - 1 ns) than the energy transfer processes ( $\sim 100$  fs - 1 ps) we are concerned with here, and should be easily separable from the desired information using our proposed procedure. Neglecting vibrational relaxation should not have a significant effect due to the assumption that the initial excitation only involves the ground vibrational states. Because of this assumption, the vibrational lifetime will primarily contribute via its effects on the vibrational linewidth, which will not have a significant impact on the quantities that are the focus of this work.

For the interaction between the monomers, we include an electronic coupling term, characterized by the parameter  $J$ . The electronic coupling serves to mix the electronic states and form delocalized excitons, labelled  $|\mu\rangle$  and  $|\nu\rangle$ , with the form

$$\begin{aligned} |\mu\rangle &= \cos \theta |e_A\rangle + \sin \theta |e_B\rangle, \\ |\nu\rangle &= -\sin \theta |e_A\rangle + \cos \theta |e_B\rangle, \end{aligned} \quad (4.7)$$

where the mixing angle  $\theta$  depends on the strength of the electronic coupling  $J$  and the difference in electronic site energies, and is given by

$$\tan 2\theta = \frac{2J}{\bar{\epsilon}_A - \bar{\epsilon}_B}, \quad (4.8)$$

where  $\bar{\epsilon}_M = \epsilon_M + \lambda_e^M + \alpha_0^{M^2} \lambda_v^M$  is the electronic transition energy on monomer  $M$  renormalized by the environmental reorganization energy for the electronic transition. The reorganization energy is related to the spectral density by  $\lambda_x^M = \hbar \int_0^\infty d\omega \mathcal{J}_x^M(\omega)/\omega$ , with  $x = e$  or  $v$ . Using this analytic form for the diagonalization of the Hamiltonian, we have four total electronic states for the system, the ground state  $|g\rangle$ , the two exciton states  $|\mu\rangle$  and  $|\nu\rangle$  and the doubly excited state  $|f\rangle$ , which is not accessible in the current experiment and will not be considered further. The overall state of the system can then be described as  $|\varepsilon v_A v_B\rangle$ , where  $\varepsilon$  denotes the electronic state, and  $v_A$  and  $v_B$  denote the vibrational quantum number for monomers  $A$  and  $B$ , respectively. The exciton energies are  $\epsilon_\mu = (\epsilon_A + \epsilon_B)/2 + \text{sign}(J)\sqrt{(\epsilon_A - \epsilon_B)^2 + 4J}$ , and  $\epsilon_\nu = (\epsilon_A + \epsilon_B)/2 - \text{sign}(J)\sqrt{(\epsilon_A - \epsilon_B)^2 + 4J}$ . Throughout this work we use capital

Roman letter to index sites, lowercase Greek letters to index excitons, and lowercase Roman letters to index other quantities. In particular, when we refer to the specific case of the dimer, we use  $\mu$  and  $\nu$  to denote the excitons, and  $A$  and  $B$  to denote the sites, whereas  $\alpha$ ,  $\beta$ ,  $\gamma$  and  $\delta$  are used to denote generic excitons, and  $M$  and  $N$  are used to denote generic sites, in the case of the dimer as well as in the case of a larger molecular aggregate.

We assume that the coupling only induces mixing between the electronic states, and that the vibrations have no role in the mixing and remain localized on the monomers. This should be a reasonable approximation for the range of parameter values considered here, where the energies of the vibrations are substantially larger than the energy gaps between the electronic states. Furthermore, for the method we propose here, all that is required is that there exists a vibrational mode on each monomer that has these properties. This will likely always be the case, even when other modes are strongly mixed with the electronic states. The inclusion of vibronic mixing and the study of its effects on the structure of the 2DEV spectra would be very interesting, but the details become complicated, and a proper treatment would require a more sophisticated method for solving the quantum dynamics than used in this study.[19, 146, 96, 60, 26] We leave the incorporation of these effects for future work.

The total Hamiltonian can be rewritten in the exciton representation as

$$\begin{aligned}
 H = & H_{bath}^A + H_{bath}^B + H_{g1}^A |g10\rangle \langle g10| + H_{g1}^B |g01\rangle \langle g01| \\
 & + (H_{e0}^A \cos^2 \theta + H_{e0}^B \sin^2 \theta + J \sin 2\theta) |\mu00\rangle \langle \mu00| \\
 & + H_{e1}^A \cos^2 \theta |\mu10\rangle \langle \mu10| + H_{e1}^B \sin^2 \theta |\mu01\rangle \langle \mu01| \\
 & + (H_{e0}^A \sin^2 \theta + H_{e0}^B \cos^2 \theta - J \sin 2\theta) |\nu00\rangle \langle \nu00| \\
 & + H_{e1}^A \sin^2 \theta |\nu10\rangle \langle \nu10| + H_{e1}^B \cos^2 \theta |\nu01\rangle \langle \nu01| \\
 & - \left[ (H_{e0}^A - H_{e0}^B) \frac{\sin 2\theta}{2} - 2J \cos 2\theta \right] (|\mu00\rangle \langle \nu00| + |\nu00\rangle \langle \mu00|) \\
 & - H_{e1}^A \frac{\sin 2\theta}{2} (|\mu10\rangle \langle \nu10| + |\nu10\rangle \langle \mu10|) + H_{e1}^B \frac{\sin 2\theta}{2} (|\mu01\rangle \langle \nu01| + |\nu01\rangle \langle \mu01|). \quad (4.9)
 \end{aligned}$$

In the derivations of the response functions used in this work, it is necessary for us to neglect the terms of the Hamiltonian that go as  $(|\mu \dots\rangle \langle \nu \dots| + |\nu \dots\rangle \langle \mu \dots|)$ , which drive energy transfer between the excitons. To account for energy transfer processes, we include the dynamics in an *ad hoc* manner similar to that used previously in the development of response functions for energy transfer and reactive systems,[178, 179] modified so that the dynamics are equivalent to Redfield theory under the secular approximation.[139, 140] The details of the method by which we include these dynamics in the response functions are given in section 4.6.

To be precise, we use excited state dynamics that are fully determined by rates of population transfer. The rates are taken from Redfield theory, which is based on a second order perturbative expansion of the system-bath coupling terms in the Hamiltonian, together with a Markov approximation.[139, 140] For a generic molecular aggregate, the Redfield relaxation

tensor is given by

$$\mathcal{R}_{\alpha\beta,\gamma\delta} = \Gamma_{\delta\beta,\alpha\gamma} + \Gamma_{\gamma\alpha,\beta\delta}^* - \delta_{\beta\delta} \sum_{\kappa} \Gamma_{\alpha\kappa,\kappa\gamma} - \delta_{\alpha\gamma} \sum_{\kappa} \Gamma_{\beta\kappa,\kappa\delta}^* \quad (4.10)$$

with the damping matrix

$$\Gamma_{\alpha\beta,\gamma\delta} = \frac{1}{\hbar^2} \sum_{M,N} \langle \alpha | V_M | \beta \rangle \langle \gamma | V_N | \delta \rangle C_{MN}[\omega_{\delta\gamma}]. \quad (4.11)$$

Here,  $V_M = \hbar \sum_i d_i^M \omega_i^M (a_i^{M\dagger} + a_i^M)$  is the system-bath coupling operator for the electronic degrees of freedom,  $C_{MN}[\omega]$  is the Fourier-Laplace transform of the environment correlation function and  $\hbar\omega_{\alpha\beta} = \epsilon_{\alpha} - \epsilon_{\beta}$  is the difference energy between excitons  $\alpha$  and  $\beta$ . The indices  $\alpha, \beta, \gamma$  and  $\delta$  run over the electronic states, expressed in the exciton basis, and  $M$  and  $N$  run over the sites. With the Redfield tensor defined in this way, the dynamics of the density matrix are given by the Redfield master equation

$$\frac{\partial}{\partial t} \rho_{\alpha\beta} = -i\omega_{\alpha\beta} \rho_{\alpha\beta}(t) + \sum_{\gamma,\delta} \mathcal{R}_{\alpha\beta,\gamma\delta} \rho_{\gamma\delta}(t). \quad (4.12)$$

The element  $\mathcal{R}_{\alpha\beta,\gamma\delta}$  represents the rate of exchange from state  $|\gamma\rangle\langle\delta|$  to state  $|\alpha\rangle\langle\beta|$ . In the full Redfield theory, any of these elements may take nonzero values. Therefore, any pair of elements in the density matrix, either population or coherence, might be coupled. By considering only the rates of population transfer, we are making the secular approximation, whereby when  $|\omega_{\alpha\beta} - \omega_{\gamma\delta}| \neq 0$ , we set  $\mathcal{R}_{\alpha\beta,\gamma\delta} = 0$ . This serves to decouple the dynamics of populations and coherences, and significantly simplifies the interpretation of the dynamics and the derivation of the response functions. In general it is not a good approximation,[163, 89] but it provides a sufficient illustration for the purposes of this work. A demonstration that the dynamics used in the response functions in this work are equivalent to the secular Redfield theory is provided in section 4.7.

## 4.2.2 Response Functions

The double-sided Feynman diagrams for the Liouville pathways included in the present approximate description are shown in figure 4.2. In this section we restrict our focus to the specific case of the dimer, though the results can be extended to a larger molecular aggregate.[30, 28] Only the diagrams corresponding to rephasing pathways are depicted, and for each there is a corresponding nonrephasing pathway, which differs by a complex conjugation of the state during  $t_1$ . Due to the very large difference in the frequencies of the electronic and vibrational coherences during the  $t_1$  and  $t_3$  periods, these pathways do not possess a significant rephasing power, and so the the information content of the rephasing and nonrephasing pathways are essentially equivalent.[43] Despite this, we maintain this

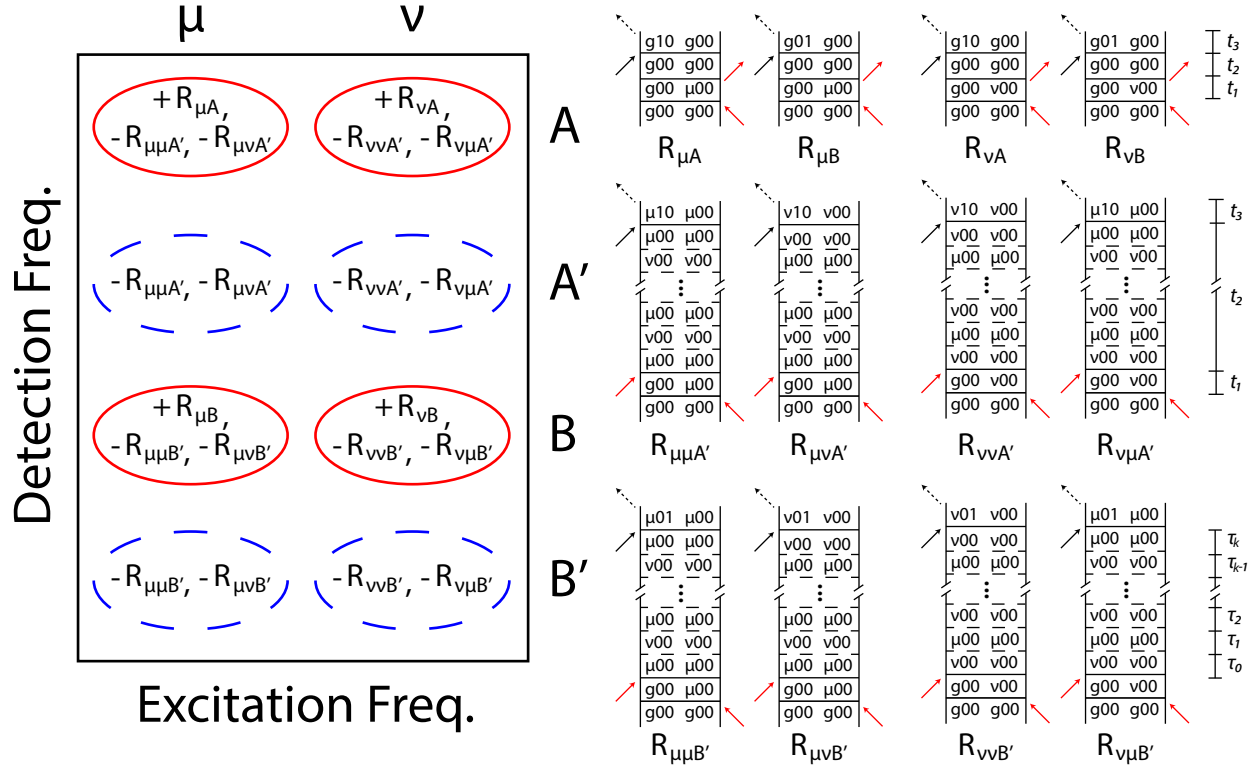


Figure 4.2: The rephasing Liouville pathways considered in this work (right), and a schematic representation of the resulting spectrum (left). The pathways that evolve on the electronic ground state are labelled as  $R_{\alpha M}$  to indicate that exciton  $|\alpha\rangle$  is excited, and the vibration on site  $M$  is probed, while those on the electronic excited state are labelled as  $R_{\alpha\beta M'}$ , to indicate the population is transferred from exciton  $|\alpha\rangle$  to exciton  $|\beta\rangle$  during  $t_2$  and that the vibration on site  $M$  is probed. The interactions with the visible laser are indicated by red arrows while the interactions with the infrared laser are indicated by black arrows, and the emission of the infrared signals are indicated by the black dashed arrows. Within the current approximations, the pathways that evolve on the electronic ground state during  $t_2$  have positive contributions (solid red lines), while the pathways that evolve on an electronic excited state make negative contributions (dashed blue lines). The plus and minus signs are present to emphasize the sign of each contribution to the total response. The time variables  $\{\tau_i\}$  are used to describe the details of the trajectory on the electronic excited state.



language here to make a clear the connection with degenerate spectroscopies. The response functions have the form

$$\begin{aligned}
 R_{\alpha M}^R(t_1, t_2, t_3) &= \langle |\vec{\mu}_\alpha|^2 |\vec{\mu}_M|^2 \rangle \\
 &\quad \times \exp \left[ i \frac{\bar{\epsilon}_\alpha}{\hbar} t_1 - i \bar{\omega}_M t_3 \right] F_{\alpha M}^R(t_1, t_2, t_3), \\
 R_{\alpha M}^{NR}(t_1, t_2, t_3) &= \langle |\vec{\mu}_\alpha|^2 |\vec{\mu}_M|^2 \rangle \\
 &\quad \times \exp \left[ -i \frac{\bar{\epsilon}_\alpha}{\hbar} t_1 - i \bar{\omega}_M t_3 \right] F_{\alpha M}^{NR}(t_1, t_2, t_3),
 \end{aligned} \tag{4.13}$$

for the rephasing and nonrephasing pathways on the ground electronic state. The angled brackets represent an orientational average, and the transition dipole moment  $\vec{\mu}_\alpha$  corresponds to the transition between the ground state and exciton  $|\alpha\rangle$ , whereas the factor  $\vec{\mu}_M$  corresponds to the transition dipole moment for the  $0 \rightarrow 1$  transition for the vibration on site  $M$ , on the electronic ground state. The coherence factor oscillates during the time period  $t_1$  at the renormalized exciton frequency  $\bar{\epsilon}_\alpha/\hbar = (\epsilon_\alpha + \lambda_\alpha)/\hbar$ , and at the renormalized vibrational frequency  $\bar{\omega}_M = \omega_M + \lambda_v^M/\hbar$  during the time period  $t_3$ . The factors  $F_{\alpha M}(t_1, t_2, t_3)$  are the third-order lineshape functions, and can be written in terms of the linear lineshape functions which describe the bath induced fluctuations in the energies of the electronic and vibrational states,  $g_e^A(t)$ ,  $g_e^B(t)$ ,  $g_v^A(t)$  and  $g_v^B(t)$ , which in turn can be directly calculated from the spectral densities for the different components of the bath.[120, 28]

The pathways that evolve on the electronic excited state during  $t_2$  have a similar structure, with a few important differences. They take the form:

$$\begin{aligned}
 R_{\alpha\beta M'}^R(t_1, t_2, t_3) &= - \left( \langle |\vec{\mu}_\alpha|^2 |\vec{\mu}_{M'}|^2 \rangle |U_{\beta M}|^2 \exp \left[ i \frac{\bar{\epsilon}_\alpha}{\hbar} t_1 - i \bar{\omega}'_M t_3 \right] \right. \\
 &\quad \left. + \langle |\vec{\mu}_\alpha|^2 |\vec{\mu}_M|^2 \rangle (1 - |U_{\beta M}|^2) \exp \left[ i \frac{\bar{\epsilon}_\alpha}{\hbar} t_1 - i \bar{\omega}_M t_3 \right] \right) F_{\alpha\beta M'}^R(t_1, t_2, t_3), \tag{4.14}
 \end{aligned}$$

$$\begin{aligned}
 R_{\alpha\beta M'}^{NR}(t_1, t_2, t_3) &= - \left( \langle |\vec{\mu}_\alpha|^2 |\vec{\mu}_{M'}|^2 \rangle |U_{\beta M}|^2 \exp \left[ -i \frac{\bar{\epsilon}_\alpha}{\hbar} t_1 - i \bar{\omega}'_M t_3 \right] \right. \\
 &\quad \left. + \langle |\vec{\mu}_\alpha|^2 |\vec{\mu}_M|^2 \rangle (1 - |U_{\beta M}|^2) \exp \left[ -i \frac{\bar{\epsilon}_\alpha}{\hbar} t_1 - i \bar{\omega}_M t_3 \right] \right) F_{\alpha\beta M'}^{NR}(t_1, t_2, t_3), \tag{4.15}
 \end{aligned}$$

where  $\alpha$  is the initial excitonic state and  $\beta$  is the final excitonic state. Note that  $\alpha$  and  $\beta$  may or may not be equal. The factor  $\bar{\omega}'_M = \omega'_M + (\alpha_1^M - \alpha_0^M)^2 \lambda_v^M/\hbar$  is the renormalized vibrational frequency when the monomer is in the electronic excited state. The factor  $\vec{\mu}_{M'}$  denotes the transition dipole moment for the  $0 \rightarrow 1$  transition for the vibration on site  $M$ , on the electronic excited state. Aside from the increased complexity of the third-order lineshape functions, which are described in detail for the general case in section 4.6, the main difference from the ground state pathways is in the transition dipole term, with the replacement of  $e.g.$

$|\vec{\mu}_M|^2$  with  $|\vec{\mu}_M U_{\beta M}|^2$ , the transition dipole for the vibration on site  $M$  when exciton  $|\beta\rangle$  is populated. The origin of the two terms can be understood from figure 4.1. The first term is related to the probability that the monomer  $M$  is in the electronic excited state, whereas the second term is related to the probability that it is in the electronic ground state. The factor of  $U_{\beta M}$  is the fraction of exciton  $|\beta\rangle$  that is localized on site  $M$ . For the case of the dimer, it is simply related to the mixing angle, *e.g.* as either  $U_{\mu A} = \cos \theta$  or  $U_{\nu A} = -\sin \theta$ . This additional factor scales the signal with the probability that the electronic excitation is localized on a given site, and is a crucial piece of information that impacts the 2DEV spectra much more directly than other techniques, such as 2DES.

We assume for this work that the interaction with the infrared pulse will only drive vibrational transitions, neglecting the possibility that it will excite transitions between the excitons. For the small excitonic energy gaps considered here, such transitions would appear at a much lower frequency ( $\sim 200 \text{ cm}^{-1}$ ) than the vibrational transitions ( $\sim 1500 \text{ cm}^{-1}$ ). A combined excitation of a vibration together with the excitonic transition will, however, have a similar energy to the pure vibrational transition, but these transitions might be very weak, depending on the symmetries and selection rules for the vibrations. For large polyatomic molecules, these selection rules can become very complex.[47, 81, 160] In either case, the electronic coherences will typically dephase much more quickly than the vibrational coherences, and so the resulting features are expected to be broad and structureless.

The frequency domain 2DEV spectrum is computed in the impulsive limit by taking the Fourier transform over the  $t_1$  and  $t_3$  domains for each term in the response function. The total response is then given by the sum of the rephasing and nonrephasing components as  $S^{tot}(\omega_1, t_2, \omega_3) = S^R(-\omega_1, t_2, \omega_3) + S^{NR}(\omega_1, t_2, \omega_3)$ . The rephasing component is reflected along the  $\omega_1$  axis because of the change in the sign of the  $t_1$  coherence oscillation term between the rephasing and nonrephasing pathways. The purely absorptive spectrum corresponds to the real part of the total spectrum, so the final result is given by  $S^{abp} = \text{Re}[S^{tot}]$ . To relax the impulsive approximation, the response functions should be convolved with the electromagnetic fields prior to the Fourier transforms. So long as the spectral bandwidths of the fields are sufficient to cover all of the transitions of interest and the pulse durations are significantly shorter than the timescale of the exciton dynamics, inclusion of realistic laser pulses should not significantly alter the discussion of the current work, so for simplicity we do not account for this additional experimental complication.

The response function method used in this work does not provide the exact result, primarily due to the neglect of the exciton coupling terms in the Hamiltonian, as described following equation (4.9), but it has substantial benefits in the ease of interpretation. With the response functions, it is easy to consider the results term-by-term, and so there is no doubt as to the origin or interpretation of any given feature. It would certainly be possible to simulate the spectral response using an exact method for solving the quantum dynamics, such as the Hierarchy Equations of Motion,[60, 93, 92] but for establishing the feasibility of our proposed approach, the current method should prove adequate.

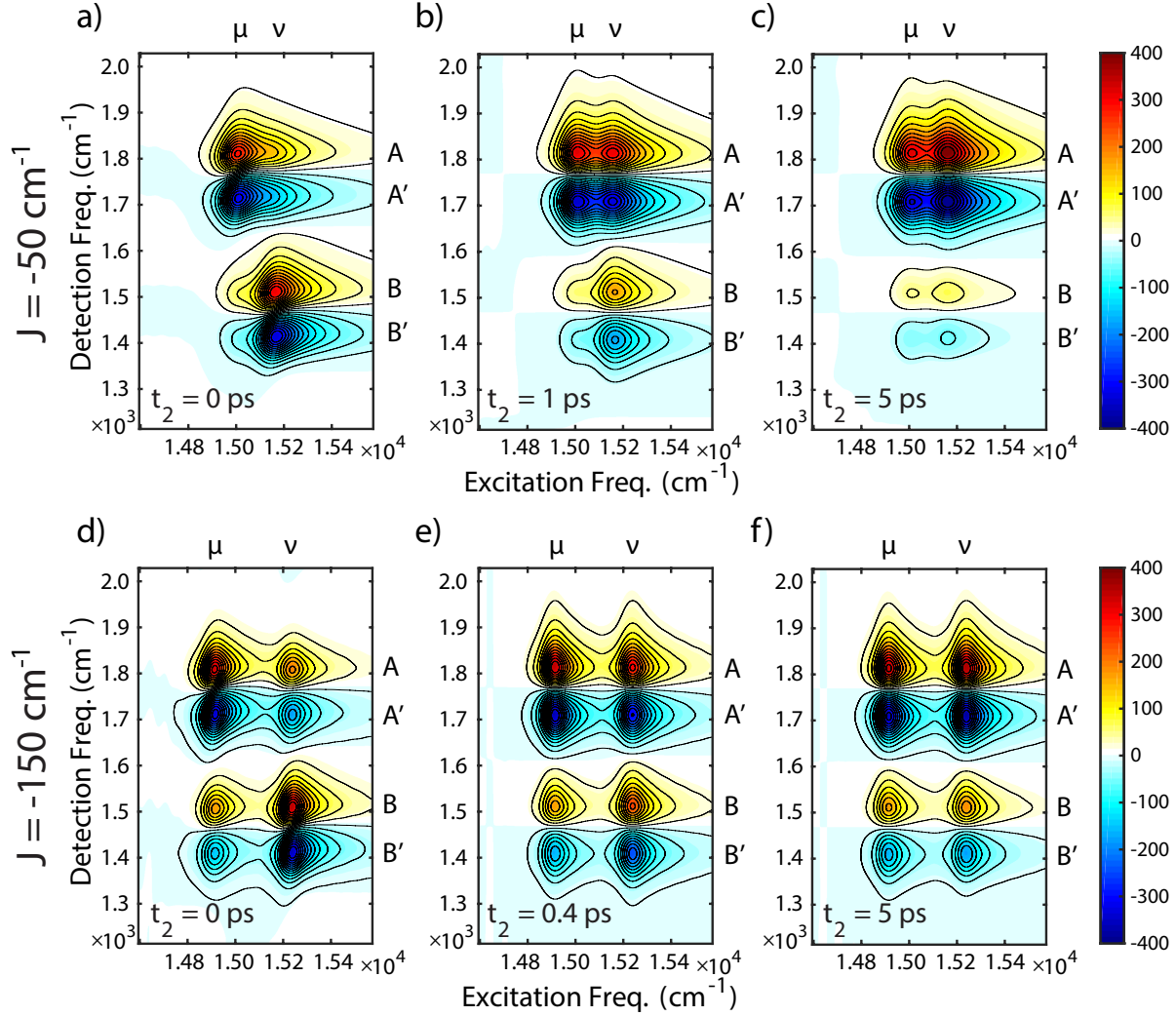


Figure 4.3: 2DEV spectra for an electronic coupling of  $J = -50 \text{ cm}^{-1}$  at a)  $t_2 = 0 \text{ ps}$ , b)  $t_2 = 1 \text{ ps}$  and c)  $t_2 = 5 \text{ ps}$ , and for an electronic coupling of  $J = -150 \text{ cm}^{-1}$  at d)  $t_2 = 0 \text{ ps}$ , e)  $t_2 = 0.4 \text{ ps}$  and f)  $t_2 = 5 \text{ ps}$ . The excitons and vibrations are labelled for clarity. The rest of the parameters used in this simulation are provided in the text.

### 4.3 Simulation Results

A series of 2DEV spectra calculated using this model are shown in figure 4.3 for two different strengths of the electronic coupling  $J$ , where we have chosen  $J = -50 \text{ cm}^{-1}$  and  $-150 \text{ cm}^{-1}$ . The spectra are shown at several different waiting times following the initial excitation, to demonstrate the structure of the spectra that result from our model. For these simulations, the site energy difference was  $\epsilon_B - \epsilon_A = 125 \text{ cm}^{-1}$ , and the vibrational frequencies were set to  $\omega_A = 1800 \text{ cm}^{-1}$ ,  $\omega'_A = 1700 \text{ cm}^{-1}$ ,  $\omega_B = 1500 \text{ cm}^{-1}$  and  $\omega'_B = 1400$

$\text{cm}^{-1}$ . These values for the frequencies were chosen to be similar to a C=C or C=O double bond stretch, as these types of modes are common in organic chromophores, and have been studied in previous transient infrared experiments of light-harvesting complexes.[68, 161, 41] The spectral densities for the baths were taken to have the Drude-Lorentz form,

$$\mathcal{J}_x^M(\omega) = \frac{2\lambda_x^M \omega_{c_x}^M \omega}{\omega_{c_x}^{M^2} + \omega^2}, \quad (4.16)$$

with reorganization energies set to  $\lambda_e^A = \lambda_e^B = 35 \text{ cm}^{-1}$  and  $\lambda_v^A = \lambda_v^B = 5 \text{ cm}^{-1}$  and cutoff frequencies for the timescales of the baths were set to  $\omega_{c_e}^A = \omega_{c_e}^B = \omega_{c_v}^A = \omega_{c_v}^B = 50 \text{ cm}^{-1}$ . We have chosen the parameters  $\alpha_0$  and  $\alpha_1$  for both monomers to take on the values 0.6 and 1.6, respectively, so that the vibrational transition on the electronic excited state couples to the bath with the same overall strength as the vibrational transition on the ground electronic state. The magnitude of these parameters is comparable to those found in measurements on the laser dye 3,3'-diethylthiatricarbocyanine iodide (DTTCl) in chloroform.[108] The temperature was set to  $T = 77 \text{ K}$ , as most multidimensional spectroscopy experiments on photosynthetic pigment-protein complexes are performed at this temperature, to improve the resolution of overlapping excitonic states. At  $T = 300 \text{ K}$  for the current parameters, the features become broad and unresolvable (results not shown). The bath parameters were chosen to be similar to those typically found in photosynthetic pigment-protein complexes.[25, 90] For demonstrative purposes, the transition dipole moments were all set to 1, and the electronic transition dipole moments for the monomers were assumed to be perpendicular. We will demonstrate in section 4.4 how these parameters can be removed in the extraction of the electronic site populations, and so this choice does not affect the results.

In each of the spectra shown in figure 4.3, there are four positive-going features that correspond to probing vibrations on the ground electronic state, and four negative-going features that correspond to vibrations on the electronic excited states (see figure 4.2). The features arise from each combination of exciton and vibrational mode, and the intensity of a given feature is proportional to the probability that the electronic excitation is localized on that monomer, together with the associated transition dipole moments. As  $t_2$  increases, the intensities of the features change, with those features corresponding to probing site *A* (the lower energy site) increasing and those corresponding to probing site *B* (the higher energy site) decreasing, due to the relaxation of the electronic populations towards thermal equilibrium. Comparing the simulations with different strengths of electronic coupling, for the stronger coupling case the exciton absorption energies show a greater separation, due to the larger splitting between the excitonic energies. Furthermore, the intensities of the features resulting from probing the separate monomers are more similar, due to the greater delocalization of the excitons relative to the weaker coupling case. Both traits are directly related to the formation of delocalized excitonic states by the electronic coupling.

The 2DEV spectrum reports on the exciton that is initially populated, but otherwise it does not provide direct information on the electronic state of the system. Instead, it provides information relating to the spatial distribution of the electronic excitation. As the higher

energy exciton  $|\nu\rangle$  relaxes and the population is transferred to  $|\mu\rangle$ , the ratio between the peaks corresponding to exciting  $|\nu\rangle$  and probing the vibrations on sites  $A$  and  $B$  becomes more like the ratio of site populations for exciton  $|\mu\rangle$ . At long waiting times, the spectra reflect the thermal populations of electronic excited states. For the low temperature simulations shown here, the equilibrium population of the higher energy exciton is very small, and, whether  $|\mu\rangle$  or  $|\nu\rangle$  is initially excited, the long-time ratios between the monomer  $A$  and  $B$  features are very similar to the ratio for the lower energy exciton.

There is no difference between the dynamics obtained by probing the vibrations when the monomer is on either the ground or the excited electronic state. In each case, the dynamics originate from the pathways  $R_{\alpha\beta M'}$ , where the system evolves according to the electronic excited state. From equations (4.14), (4.15), (4.33) and (4.34), the amplitudes resulting from these pathways depend on the probability that a given exciton is populated, together with the fraction of that exciton localized on each monomer. These features suggest that it should be possible to directly extract the electronic site populations from the spectra, without the need for a model. A method for isolating this information is described in section 4.4.

In addition to reporting on the dynamics of the system during the waiting time, the 2DEV spectra also provide information about the bath dynamics, and the system-bath coupling. At early waiting times, the features in the 2DEV spectra have positive center-line slopes, which is indicative of the initial correlation between the electronic and vibrational transition frequencies. For the isolated monomers, the decay of this slope is proportional to the correlation function for the bath-induced fluctuations in the energy of the vibrational transition, and there may be a long-time non-zero slope when there exists a correlation between the inhomogeneous distributions of the electronic and vibrational energy gaps.[43, 108] Due to the electronic mixing in the dimer, the specific form of the center-line slope becomes more complicated, as it will contain contributions from multiple pathways and will depend on the electronic mixing angle and the correlation functions for the vibration on each monomer. The dynamics still reflect the correlation between the electronic and vibrational transitions, primarily induced via the fluctuations of the vibrational zero-point energies on the electronic excited state, but interference effects may complicate the precise dynamics.[178, 179] A detailed analysis of the information that can be extracted from these slopes is left for future considerations.

## 4.4 Measurement of Electronic Site Populations

The major advantage of 2DEV comes from its ability to provide a direct experimental connection between the electronic eigenstates and the physical location of the excitation energy on a molecular scale. In this section, we demonstrate how the 2DEV spectrum of a molecular aggregate could be used to directly measure the electronic site populations. As will become clear, this method does not rely on a model. The fundamental experimentally measurable quantity that we use is  $S_{\alpha M}(t_2)$ , the integrated intensity of the spectral feature

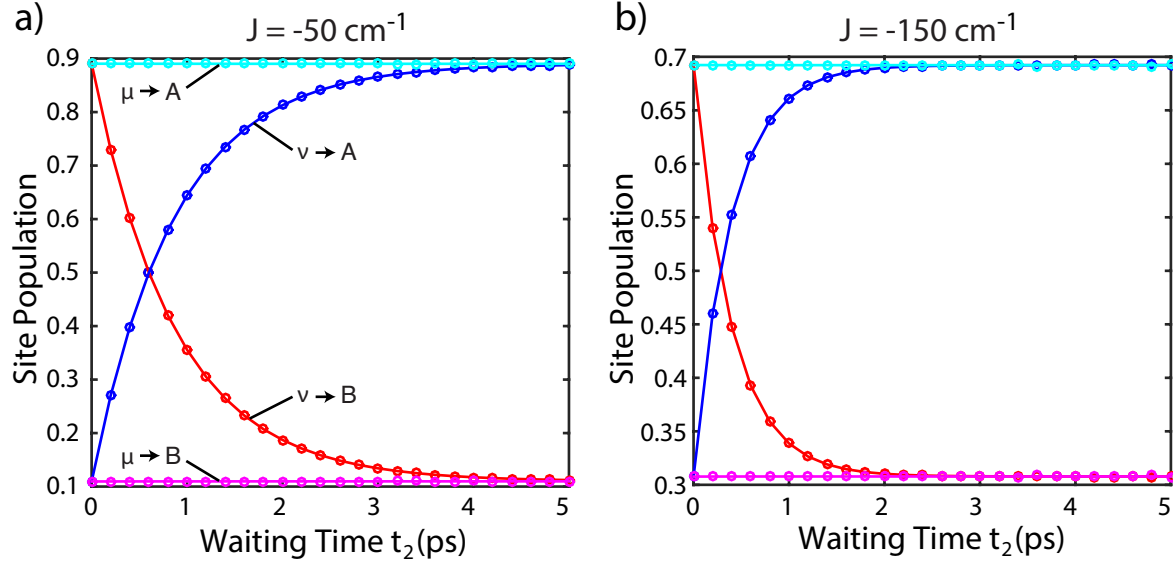


Figure 4.4: The site populations extracted from the simulated spectra (circles), compared against the populations calculated by integrating the Redfield master equation (lines). The parameters are for the same as figure 4.3. Panel a) shows results for  $J = -50 \text{ cm}^{-1}$ , and panel b) shows results for  $J = -150 \text{ cm}^{-1}$ . The blue and red curves show the populations on sites A and B following initial excitation to the higher energy exciton, while for the cyan and magenta curves the initial excitation was to the lower energy exciton. For this figure, the values from the spectral simulations were taken from the electronic excited state features. It makes no difference if the ground state features are used instead.

arising from excitation of exciton  $|\alpha\rangle$  and detection of the vibration on site  $M$ . We can choose to use the features that arise from probing the vibration on either the electronic ground or excited state, each of which contains contributions from the pathways  $R_{\alpha\beta M'}$ . For probing the vibration on the electronic ground state, this is given by

$$S_{\alpha M}(t_2) = \int d\omega_1 d\omega_3 \sum_{\beta} S_{\alpha\beta M}^{abp}(\omega_1, t_2, \omega_3) = \langle |\vec{\mu}_{\alpha}|^2 |\vec{\mu}_M|^2 \rangle P_{\alpha M}(t_2), \quad (4.17)$$

where  $P_{\alpha M}(t_2)$  is the probability that the electronic excitation is localized on site  $M$  at time  $t_2$ , given that the initial excitation populated exciton  $|\alpha\rangle$ . The sum runs over all the exciton states. The only change that is made for probing the vibration on the electronic excited state is to replace the vibrational transition dipole on the electronic ground state,  $|\vec{\mu}_M|^2$ , with that on the electronic excited state,  $|\vec{\mu}_{M'}|^2$ . The overall probability that an electronic excited state is populated at time  $t_2$ , following excitation to exciton  $|\alpha\rangle$ , is given by  $\sum_N P_{\alpha N}(t_2)$ , so the

normalized site population is given by

$$\frac{P_{\alpha M}(t_2)}{\sum_N P_{\alpha N}(t_2)} = \left(1 + \sum_{N \neq M} \frac{P_{\alpha N}(t_2)}{P_{\alpha M}(t_2)}\right)^{-1} = \left(1 + \sum_{N \neq M} \frac{\langle |\vec{\mu}_M|^2 \rangle S_{\alpha N}(t_2)}{\langle |\vec{\mu}_N|^2 \rangle S_{\alpha M}(t_2)}\right)^{-1}. \quad (4.18)$$

The only information required in addition to the 2DEV spectral amplitudes is therefore the ratios of transition dipole moments for the vibrations on either the electronic ground or excited state, depending on which features are being used. It is also important to note that any decay of the signal due to relaxation to the electronic ground state will be removed by the normalization. If it is desired that the relaxation to the ground electronic state be included, then equation (4.18) must be modified by taking the denominator on the left-hand side at  $t_2 = 0$ . This, however, may introduce difficulties related to the finite duration of real laser pulses.

So far as the current discussion is concerned, there is no significant difference between the information content that can be extracted from probing the vibrations on the ground versus the excited electronic states. This choice is a practical matter, since in particular molecules and for particular vibrations the vibrational transition dipoles on the ground and excited electronic states might have very different magnitudes. For example, 2DEV spectra of the C=C backbone stretch mode in DTTCl are dominated by the electronic ground state feature,[108] whereas in 8'-apo- $\beta$ -caroten-8'-al the spectrum is dominated by electronic excited state features.[131, 126] Additionally, it is often easier to assign vibrations on the ground electronic state, due to the computational expense of *ab. initio* excited state frequency analysis.

There is, however, a substantial difference in the ease with which the ratio of vibrational transition dipoles that appears in equation (4.18) can be measured for the ground or excited electronic states. For the ground electronic state, this ratio can be easily extracted from the vibrational linear absorption. The ratio  $\langle |\vec{\mu}_{M'}|^2 \rangle / \langle |\vec{\mu}_{N'}|^2 \rangle$  between vibrational transition dipoles on the electronic excited state, however, is in general very difficult to measure. In principle it could be extracted from transient-2DIR spectra, or approximated from the 2DEV spectra of the monomers in isolation, but each of these approaches would require performing another difficult experiment in addition to measuring the 2DEV spectra of the system of interest. Here, we propose a method for measuring this ratio that requires only the 2DEV spectrum at  $t_2 = 0$  and the electronic linear absorption spectrum. To understand this procedure, consider  $S_\alpha^{(1)}$ , the integrated intensity of the electronic linear absorption to exciton  $|\alpha\rangle$ . This is given by

$$S_\alpha^{(1)} = \int d\omega \langle |\vec{\mu}_\alpha|^2 \rangle S_\alpha^{(1)}(\omega) = \langle |\vec{\mu}_\alpha|^2 \rangle, \quad (4.19)$$

where  $S_\alpha^{(1)}(\omega)$  is given by the Fourier Transform of the linear lineshape function  $g_\alpha(t)$ . This integrated intensity can be related to the integrated intensity of the 2DEV spectrum at  $t_2 = 0$  as  $S_\alpha^{(1)} = \sum_N S_{\alpha N}(0) / \langle |\vec{\mu}_{N'}|^2 \rangle$ . Therefore, if we populate a vector  $|S^{(1)}\rangle$  with the values  $S_\alpha^{(1)}$

for every exciton  $|\alpha\rangle$ , and a matrix  $\hat{S}_{ex-site}$  with the values  $S_{\alpha N}(0)$  for every exciton  $|\alpha\rangle$  and site  $N$ , then it is possible to extract the required ratio of transition dipoles as

$$\frac{\langle |\vec{\mu}_{M'}|^2 \rangle}{\langle |\vec{\mu}_{N'}|^2 \rangle} = \frac{\langle N | \hat{S}_{ex-site}^{-1} | S^{(1)} \rangle}{\langle M | \hat{S}_{ex-site}^{-1} | S^{(1)} \rangle}, \quad (4.20)$$

where  $|N\rangle = |0_1, 0_2, \dots, 0_{N-1}, 1_N, 0_{N+1}, \dots\rangle$  indicates a unit vector representing site  $N$ . In equation (4.20), the matrix  $\hat{S}_{ex-site}$  can be thought of as a linear mapping between the exciton basis and the site basis. The special case of the dimer is given by

$$\frac{\langle |\vec{\mu}_A|^2 \rangle}{\langle |\vec{\mu}_B|^2 \rangle} = \frac{S_\mu^{(1)} S_{\nu A}(0) - S_\nu^{(1)} S_{\mu A}(0)}{S_\nu^{(1)} S_{\mu N}(0) - S_\mu^{(1)} S_{\nu N}(0)}, \quad (4.21)$$

where  $N$  is either site  $A$  or  $B$ . Therefore, so long as it is possible to measure  $S_{\alpha N}(t_2)$  and  $S_\alpha^{(1)}$  for each exciton  $|\alpha\rangle$  and each site  $N$ , then it should be possible to isolate  $P_{\alpha M}(t_2)/\sum_N P_{\alpha N}(t_2)$ , the population on site  $M$  following excitation to exciton  $|\alpha\rangle$  at time  $t_2$ . Note that in a real experiment with finite pulse durations the spectrum at  $t_2 = 0$  might be contaminated by other pathways, and so equation (4.20) becomes approximate, and it may be necessary to use a different method to estimate the ratio of transition dipoles.

Once the relevant ratio of vibrational transition dipole moments has been measured, the only information necessary from the 2DEV spectrum to extract the site populations following excitation to exciton  $|\alpha\rangle$  is the quantity  $S_{\alpha M}(t_2)$ , for each site  $M$ . This might be a very difficult task in a real situation, when there are many vibrational transitions and many excitons, all potentially overlapping in the spectrum. In the case shown in figure 4.3 d-f) with electronic coupling  $J = -150 \text{ cm}^{-1}$ , it is relatively easy to see that this would be possible, due to the substantial splitting between the exciton energies. For the weaker electronic coupling of  $J = -50 \text{ cm}^{-1}$  shown in figure 4.3 a-c), the features corresponding to different excitons overlap significantly, and the separation of the contributions from each feature becomes more difficult. In many cases, even this degree of spectral resolution might not be possible. For experimental data, one method for extracting the necessary information and removing the interference from neighboring features might be to perform an evolution-associated decomposition of the spectrum.[162, 174, 128] In principle, however, equation (4.18) provides a method by which the site population could be directly extracted from the experimental data without the need for a model Hamiltonian to relate the excitons to the sites.

A numerical demonstration of this procedure is shown in figure 4.4. We take advantage of the fact that each term of the total response function is calculated separately, and so it is trivial to calculate the integral over each individual contribution. In this figure, we compare the site populations as extracted from the simulations of the 2DEV spectra using equation (4.18) with those calculated directly by propagating the Redfield master equations under the secular approximation. For the Redfield dynamical simulations, the initial conditions were



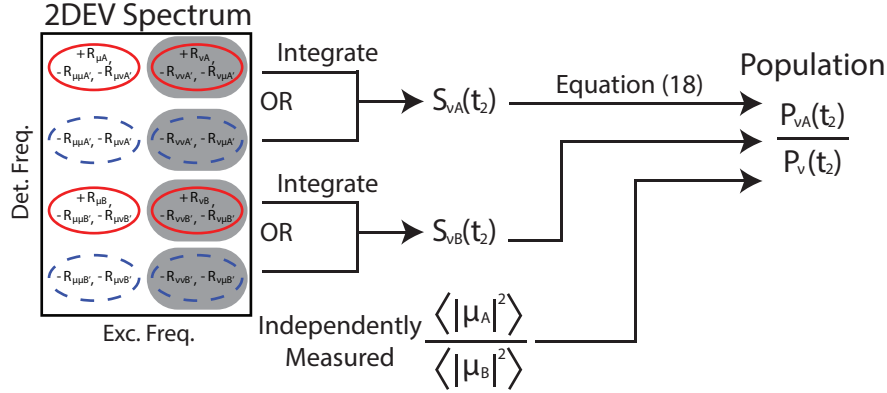


Figure 4.5: A schematic overview of the proposed method for measuring the electronic site populations for a dimer. Either the ground or excited electronic state features are chosen for the analysis. The ratio of transition dipole moments for the vibrations on the relevant electronic state can be measured with any method, though some suggestions that rely only on linear absorption and the 2DEV spectrum are described in the text.

chosen as either  $\rho(0) = |\mu\rangle\langle\mu|$  or  $|\nu\rangle\langle\nu|$ . The results from the spectral simulations match perfectly with the results from the secular Redfield theory, demonstrating that there is no approximation in equation (4.18). Furthermore, this method of extracting populations is not specific to the use of secular Redfield theory for the dynamics, and we expect that it should work equally well for exact quantum dynamics, or to extract the true quantum dynamics from the real experimental data. Therefore, this method provides a means by which 2DEV spectra can be used to directly extract the electronic site population as a function of time without need for a model, or the associated approximations. To our knowledge, no other experiment is currently capable of this measurement.

A schematic summary of the proposed method for extracting the electronic site populations from the 2DEV spectra is shown in figure 4.5. The choice to use either the ground or excited electronic state features can be made based on convenience, and makes only a practical difference. The only information required in addition to the 2DEV spectra is the ratio of vibrational transition dipoles, and no comparison with a model is necessary.

## 4.5 Conclusion

In this work, we have derived response functions for simulating the 2DEV spectra of a molecular dimer, and proposed a method by which the 2DEV spectra of a molecular aggregate could be used to directly measure the electronic site populations following the initial electronic excitation, without the need for a model to interpret the results. The proposed method, given by equation (4.18) and illustrated schematically in figure 4.5, makes no approximations that are apparent with the current model. To demonstrate the feasibility

of this experiment, we have analyzed the results from the response function simulations that use excitonic dynamics consistent with Redfield theory, under the secular approximation, and compared the results with a direct quantum dynamics simulation. We believe that the results do not depend on the specific quantum dynamics used, and, in future work, we intend to demonstrate this, as well as relax some of the assumptions in the model. Of significant interest would be the direct measurement of coherent electronic dynamics, and the incorporation of vibronic mixing between the sites, involving either the probed vibration or a separate low frequency mode.[60, 49, 34, 96] A number of synthetic and biological dimers which sample different parameter regimes have been described, which would serve as very interesting systems to test the practical application of this experiment.[130, 63, 24, 76, 165, 78, 53, 70]

It is important to note that there are a number of practical difficulties that might limit the general applicability of the approach described in this work. In particular, it crucially relies on the ability to resolve the spectral features corresponding to each exciton and to a vibration on each site in the 2DEV spectra. For many commonly studied molecular aggregates, including J-aggregates and most photosynthetic pigment-protein complexes, this may be a difficult task. It is exacerbated by the absence of strong rephasing power in 2DEV spectroscopy, which means that the homogeneous and inhomogeneous components of the linewidth cannot be separated onto different axes, as occurs with degenerate techniques such as 2DES and 2DIR. This implies that unless the features can be resolved in the linear absorption spectra, it is unlikely that they will be resolvable in the 2DEV spectra. A possible approach to alleviating this difficulty might be to use an evolution-associated spectral decomposition, to take advantage of the different dynamics for each exciton and site, but this approach can be complicated, and is not always guaranteed to provide all of the information required here. We expect that future experimental and theoretical studies will provide a method that is more generally applicable and robust to the complexity of real experimental systems.

Aside from these limitations, the promise of the proposed experiment is substantial. It represents, to our knowledge, the first experimental technique that directly links the energetic dynamics of electronic excitations with spatial information describing where in the complex the excitation is located, on the scale of individual pigments. Other experiments, such as time resolved fluorescence or transient absorption anisotropy,[176, 183, 116] 2DES with polarization control[151, 66] and coherent nonlinear frequency generation,[39] can provide indirect information which, when assisted by a model, can inform our understanding of the link between the excitonic and spatial structures, but they will always be strongly dependent on the details and quality of the model. 2DEV is capable of providing a direct experimental link between these representations, and shows promise in aiding the development of a more complete picture of excitonic dynamics in molecular aggregates.

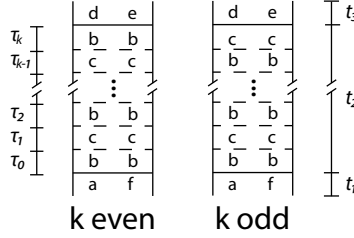


Figure 4.6: Generic Feynman diagrams for the type of exciton dynamics considered in this work. During  $t_2$  we allow  $k$  transitions between the population states in the one exciton manifold obeying some rate equation, with no coupling into coherences.

## 4.6 Derivation of the Dimer Response Functions

Generic Feynman diagrams for the type of pathway considered in this work to describe the excited state dynamics are shown in figure 4.6. The derivations in this section do not depend on any specific details of the system, so the labels  $a-f$  are used to denote any generic states. The central approximation we are making here is that the energy transfer dynamics are determined by a rate  $k_{c \leftarrow b}$  from  $|b\rangle \langle b|$  to  $|c\rangle \langle c|$ , and a rate  $k_{b \leftarrow c}$  for the reverse process, while assuming that there is no transfer between these populations and the coherences, eg:  $|b\rangle \langle b|$  to  $|b\rangle \langle c|$ . If we take the rates from the Redfield theory, then this corresponds to the secular approximation. It is important here because it allows us to write a relatively simple closed form for the response function. The substantial simplification allowed by this approximation appears if we notice that the overall nuclear propagator during  $t_2$  has no contribution when isolated, and so when we perform the second order cumulant expansion we will only have to consider the cross terms between  $t_1$  and  $t_2$  and between  $t_2$  and  $t_3$ . The terms in the expansion that only depend on  $t_2$  all cancel.

The response functions shown in figure 4.6 can be written as [178, 179]

$$F(t_1, t_2, t_3; \{\tau_m\}) = \left\langle \mathcal{G}_{de,de}(t_3) \left[ \prod_{m=0}^k (\delta_{me} \mathcal{G}_{bb,bb}(\tau_m) + \delta_{mo} \mathcal{G}_{cc,cc}(\tau_m)) \right] \mathcal{G}_{af,af}(t_1) \rho_{eq} \right\rangle \quad (4.22)$$

where  $\rho_{eq}$  is the equilibrium density matrix,  $\mathcal{G}_{ij,ij}(t)$  denotes the Liouville space Green's function that describes evolution according to the state  $|i\rangle \langle j|$ , and  $\delta_{me}$  and  $\delta_{mo}$  are delta functions that test for whether  $m$  is even or odd, respectively.

Written in terms of the Hilbert space time evolution operators, we have

$$\begin{aligned}
 F(t_1, t_2, t_3; \{\tau_m\}) = & \left\langle \exp_- \left( \frac{i}{\hbar} \int_0^{t_1} d\tau' U_{fg} \right) \exp_- \left( \frac{i}{\hbar} \int_{t_1}^{t_1+\tau_0} d\tau' U_{bg} \right) \right. \\
 & \times \left[ \prod_{m=0}^{k-1} \exp_- \left( \frac{i}{\hbar} \int_{t_1+\sum_{n=0}^m \tau_n}^{t_1+\sum_{n=0}^{m+1} \tau_n} d\tau'_m (U_{cg}\delta_{me} + U_{bg}\delta_{mo}) \right) \right] \\
 & \times \exp_- \left( \frac{i}{\hbar} \int_{t_1+t_2}^{t_1+t_2+t_3} d\tau' U_{eg} \right) \exp_+ \left( -\frac{i}{\hbar} \int_{t_1+t_2}^{t_1+t_2+t_3} d\tau' U_{dg} \right) \\
 & \times \left[ \prod_{m=0}^{k-1} \exp_+ \left( -\frac{i}{\hbar} \int_{t_1+\sum_{n=0}^m \tau_n}^{t_1+\sum_{n=0}^{m+1} \tau_n} d\tau'_m (U_{cg}\delta_{me} + U_{bg}\delta_{mo}) \right) \right] \\
 & \times \exp_+ \left( -\frac{i}{\hbar} \int_{t_1}^{t_1+\tau_0} d\tau' U_{bg} \right) \exp_+ \left( -\frac{i}{\hbar} \int_0^{t_1} d\tau' U_{ag} \right) \rho_{eq} \Big\rangle, \quad (4.23)
 \end{aligned}$$

where  $\exp_+$  and  $\exp_-$  are, respectively, the positively and negatively time-ordered exponentials, and  $U_{ig} = (V_i - V_g) - \langle V_i - V_g \rangle$  denotes the difference between the system-bath coupling terms in the Hamiltonian for level  $|i\rangle$  and the ground state.[120, 28] Now, via an application of the second order cumulant expansion, we can find the general result for the third order lineshape function to be

$$F(t_1, t_2, t_3; \{\tau_m\}) = \mathcal{F}(t_1, t_2, t_3) \times \mathfrak{F}(t_2, t_3, \{\tau_m\}), \quad (4.24)$$

where the part that depends on the initial and final states, but not on the specific trajectory, is

$$\begin{aligned}
 \mathcal{F}(t_1, t_2, t_3) = & \exp \left[ -g_{dd}(t_3) - g_{ee}^*(t_3) - g_{aa}(t_1) - g_{ff}^*(t_1) \right] \\
 & \times \exp \left[ -f_{da}^-(t_1, t_2, t_3) + f_{df}^{*-}(t_1, t_2, t_3) + 2 \operatorname{Re} [g_{de}(t_3)] \right] \\
 & \times \exp \left[ 2 \operatorname{Re} [g_{af}(t_1)] + f_{ae}^-(t_1, t_2, t_3) - f_{fe}^{*-}(t_1, t_2, t_3) \right] \quad (4.25)
 \end{aligned}$$

with the auxiliary lineshape function

$$f_{ij}^-(t_1, t_2, t_3) = g_{ij}(t_2) - g_{ij}(t_1 + t_2) - g_{ij}(t_2 + t_3) + g_{ij}(t_1 + t_2 + t_3). \quad (4.26)$$

The part that depends on details of the particular trajectory is

$$\begin{aligned}
 \mathfrak{F}(t_2, t_3, \{\tau_m\}) = & \\
 & \times \exp [2i \operatorname{Im} [g_{be}(t_2 + t_3) - g_{be}(t_2 + t_3 - \tau_0) - g_{be}(t_2) + g_{be}(t_2 - \tau_0)]] \\
 & \times \exp \left[ 2i \sum_{m=0}^{k-1} \delta_{mo} \operatorname{Im} \left[ g_{be} \left( t_2 + t_3 - \sum_{n=0}^m \tau_n \right) - g_{be} \left( t_2 + t_3 - \sum_{n=0}^{m+1} \tau_n \right) \right. \right. \\
 & \quad \left. \left. - g_{be} \left( t_2 - \sum_{n=0}^m \tau_n \right) + g_{be} \left( t_2 - \sum_{n=0}^{m+1} \tau_n \right) \right] \right] \\
 & \times \exp \left[ 2i \sum_{m=0}^{k-1} \delta_{me} \operatorname{Im} \left[ g_{ce} \left( t_2 + t_3 - \sum_{n=0}^m \tau_n \right) - g_{ce} \left( t_2 + t_3 - \sum_{n=0}^{m+1} \tau_n \right) \right. \right. \\
 & \quad \left. \left. - g_{ce} \left( t_2 - \sum_{n=0}^m \tau_n \right) + g_{ce} \left( t_2 - \sum_{n=0}^{m+1} \tau_n \right) \right] \right] \\
 & \times \exp [-2i \operatorname{Im} [g_{bd}(t_2 + t_3) - g_{bd}(t_2 + t_3 - \tau_0) - g_{bd}(t_2) + g_{bd}(t_2 - \tau_0)]] \\
 & \times \exp \left[ -2i \sum_{m=0}^{k-1} \delta_{mo} \operatorname{Im} \left[ g_{bd} \left( t_2 + t_3 - \sum_{n=0}^m \tau_n \right) - g_{bd} \left( t_2 + t_3 - \sum_{n=0}^{m+1} \tau_n \right) \right. \right. \\
 & \quad \left. \left. - g_{bd} \left( t_2 - \sum_{n=0}^m \tau_n \right) + g_{bd} \left( t_2 - \sum_{n=0}^{m+1} \tau_n \right) \right] \right] \\
 & \times \exp \left[ -2i \sum_{m=0}^{k-1} \delta_{me} \operatorname{Im} \left[ g_{cd} \left( t_2 + t_3 - \sum_{n=0}^m \tau_n \right) - g_{cd} \left( t_2 + t_3 - \sum_{n=0}^{m+1} \tau_n \right) \right. \right. \\
 & \quad \left. \left. - g_{cd} \left( t_2 - \sum_{n=0}^m \tau_n \right) + g_{cd} \left( t_2 - \sum_{n=0}^{m+1} \tau_n \right) \right] \right]. \quad (4.27)
 \end{aligned}$$

Here we define the lineshape functions

$$\begin{aligned}
 g_{ij}(t) &= \int_0^t d\tau_1 \int_0^{\tau_1} d\tau_2 C_{ij}(\tau_2) \\
 C_{ij}(t) &= \frac{1}{\hbar^2} \langle U_{ig}(t) U_{jg}(0) \rho_{eq} \rangle
 \end{aligned} \tag{4.28}$$

where the angular brackets indicate averaging over the bath coordinates. Note that for any given pathway, either  $a$  or  $f$  is the ground state, so many of the terms in the above equation will not contribute (note that  $U_{gg}(t) = 0$ ). Typically, there will also be some relation between  $d$  and  $e$  that will result in simplification, as well.

To calculate the total response, it is necessary to integrate the above equation over all possible trajectories for a fixed  $t_2$ . The probability of a specific trajectory that has  $k$

transitions during  $t_2$  and begins on state  $|b\rangle$   $\langle b|$  is given by

$$P_b(k, t_2, \{\tau_m\}) = \Theta \left( t_2 - \sum_{m=0}^{k-1} \tau_m \right) \left( \delta_{ke} (k_{c \leftarrow b} k_{b \leftarrow c})^{\frac{k}{2}} + \delta_{ko} \left( k_{c \leftarrow b}^{\frac{k+1}{2}} k_{b \leftarrow c}^{\frac{k-1}{2}} \right) \right) \\ \times \exp \left[ - (k_{c \leftarrow b} \delta_{ke} + k_{b \leftarrow c} \delta_{ko}) \left( t_2 - \sum_{m=0}^{k-1} \tau_m \right) \right] \prod_{m=0}^{k-1} \exp [ - (k_{c \leftarrow b} \delta_{me} + k_{b \leftarrow c} \delta_{mo}) \tau_m ] \quad (4.29)$$

Where  $\Theta(t)$  denotes a Heaviside step function. The overall response function is then given by

$$F(t_1, t_2, t_3) = \sum_{k=0}^{\infty} \int_0^{t_2} d\tau_0 \int_0^{t_2} d\tau_1 \dots \int_0^{t_2} d\tau_{k-1} P_b(k, t_2, \{\tau_m\}) F(t_1, t_2, t_3; \{\tau_m\}) \quad (4.30)$$

To calculate a specific term of the response function, it is necessary to split up equation (4.30) in terms of the final state, which gives us the final result:

$$F_{bb}(t_1, t_2, t_3) = \sum_{k=0}^{\infty} \int_0^{t_2} d\tau_0 \int_0^{t_2} d\tau_1 \dots \int_0^{t_2} d\tau_{k-1} \delta_{ke} P_b(k, t_2, \{\tau_m\}) F(t_1, t_2, t_3; \{\tau_m\}) \quad (4.31)$$

$$F_{bc}(t_1, t_2, t_3) = \sum_{k=0}^{\infty} \int_0^{t_2} d\tau_0 \int_0^{t_2} d\tau_1 \dots \int_0^{t_2} d\tau_{k-1} \delta_{ko} P_b(k, t_2, \{\tau_m\}) F(t_1, t_2, t_3; \{\tau_m\}). \quad (4.32)$$

In practice, these summations can be truncated after a finite number of terms, as for a given  $t_2$ , the probability of a trajectory approaches 0 for large values of  $k$ . This can be clearly seen when it is recognized that equation (4.29) reduces to a Poisson distribution when  $k_{c \leftarrow b} = k_{b \leftarrow c}$ . For the simulations in this work the multidimensional integrals were computed using the VEGAS Monte Carlo algorithm,[105] and it was typically sufficient to truncate the summation to fewer than 10 terms.

## 4.7 Equivalence with Secular Redfield

We can verify that the dynamics used in the spectral simulations are the same as for secular Redfield theory, with the initial conditions of  $\rho(0) = |\mu\rangle \langle \mu|$  or  $\rho(0) = |\nu\rangle \langle \nu|$ . For the spectral simulations, the dynamics following excitation of exciton  $|\mu\rangle$  are given by the direct integration of equations

$$\rho_{\mu \leftarrow \mu}(t) = \sum_{k=0}^{\infty} \int_0^t d\tau_0 \int_0^t d\tau_1 \dots \int_0^t d\tau_k \delta_{ke} P_{\mu}(k, t, \{\tau_i\}) \quad (4.33)$$

and

$$\rho_{\nu \leftarrow \mu}(t) = \sum_{k=0}^{\infty} \int_0^t d\tau_0 \int_0^{\tau_0} d\tau_1 \dots \int_0^{\tau_{k-1}} d\tau_k \delta_{k0} P_{\mu}(k, t, \{\tau_i\}) \quad (4.34)$$

with analogous equations for the initial condition  $\rho(0) = |\nu\rangle \langle \nu|$ .

To show that the secular Redfield dynamics are equivalent to the dynamics from equations (4.33) and (4.34), we can write the formal solution to the Redfield equations in the interaction picture,[89]

$$\rho_{\alpha\beta} = \rho_{\alpha\beta}(0) e^{\mathcal{R}_{\alpha\beta, \gamma\delta} t} + \sum_{(\gamma, \delta) \neq (\alpha, \beta)} \mathcal{R}_{\alpha\beta, \gamma\delta} \int_0^t dt' e^{\mathcal{R}_{\alpha\beta, \alpha\beta}(t-t')} e^{i(\omega_{\alpha\beta} - \omega_{\gamma\delta})t'} \rho_{\gamma\delta}(t'). \quad (4.35)$$

Now we will make the secular approximation and focus on the population dynamics of the dimer system, and take the initial condition to be  $\rho_{\mu\mu}(0) = 1$ . Under these conditions, we can find the population terms for the singly excited states to be:

$$\begin{aligned} \rho_{\mu\mu}(t) &= e^{-\mathcal{R}_{\mu\mu, \mu\mu}(t)} + \mathcal{R}_{\mu\mu, \nu\nu} \int_0^t dt' e^{\mathcal{R}_{\mu\mu, \mu\mu}(t-t')} \rho_{\nu\nu}(t') \\ \rho_{\nu\nu}(t) &= \mathcal{R}_{\nu\nu, \mu\mu} \int_0^t dt' e^{\mathcal{R}_{\nu\nu, \nu\nu}(t-t')} \rho_{\mu\mu}(t'). \end{aligned} \quad (4.36)$$

By combining these equations, and making the identification of  $k_{\nu \leftarrow \mu} = \mathcal{R}_{\mu\mu, \mu\mu} = -\mathcal{R}_{\nu\nu, \mu\mu}$  and  $k_{\mu \leftarrow \nu} = \mathcal{R}_{\nu\nu, \nu\nu} = -\mathcal{R}_{\mu\mu, \nu\nu}$ , we can get a recursive equation for  $\rho_{\mu\mu}(t)$ , which when taken to infinite depth becomes

$$\rho_{\mu\mu}(t) = \sum_{k'=0}^{\infty} \int_0^t dt'_0 \dots \int_0^{t'_{2k-1}} dt'_{2k} (k_{\mu \leftarrow \nu} k_{\nu \leftarrow \mu})^{k'} \prod_{i=0}^{2k'} (\exp [-(k_{\nu \leftarrow \mu} \delta_{ie} + k_{\mu \leftarrow \nu} \delta_{io})(t - t'_i)]) \quad (4.37)$$

with an analogous equation for  $\rho_{\nu\nu}(t)$ . Under a straightforward change of variables, equation (4.37) is equivalent to equation (4.33). Therefore, the only approximation to the dynamics in the spectral simulations on top of those already made in the secular Redfield theory is the truncation of equations (4.33) and (4.34) after a finite number of terms. This is acceptable, because this sum can be made to converge to the limiting value with a moderate number of terms.

## Chapter 5

# Two-Dimensional Electronic-Vibrational Spectroscopy of Chlorophyll *a* and *b*

### 5.1 Introduction

Chlorophyll serves a central role in the photosynthetic apparatus of most photosynthetic organisms, including plants. In higher plants, chlorophyll molecules (structure shown in Figure 5.1), in particular chlorophyll *a* (Chl *a*) and chlorophyll *b* (Chl *b*) serve as the major light absorbing molecules in photosynthetic pigment-protein complexes (PPCs).[12] The majority of Chl *a* and Chl *b* molecules can be found bound in the light-harvesting complex II (LHCII), which is the primary light harvesting PPC in plants. In this complex, the major role of the Chl *a* and *b* is to absorb light, and to transfer this energy through space until it reaches the reaction center, where the electronic excitation can drive charge separation, ultimately leading to the excitation energy being converted to chemical energy.

A detailed understanding of the excitation energy transfer pathways in LHCII and related PPCs is essential for a complete and accurate understanding of the workings of the photosynthetic apparatus, and much progress has been made in recent years in mapping out the energetic landscape of these PPCs using multidimensional electronic spectroscopy.[21, 149, 151, 77, 7, 129, 54, 44, 20, 46] There still remain important questions, however, about the details of the relationship between the energetic structures of these PPCs, which are readily accessible with electronic spectroscopies, and the spatial structures of the actual pigment layout in the protein. In chapter 4, we proposed a method by which two-dimensional electronic-vibrational spectroscopy (2DEV) could be used to make this link between the energetic and spatial domains, by using localized vibrational modes as a proxy for position within a complex system, such as a photosynthetic PPC.[107] This method critically relies on an ability to resolve and assign both electronic and vibrational features for each chromophore and electronic state of interest. A prerequisite for this to be possible is a detailed



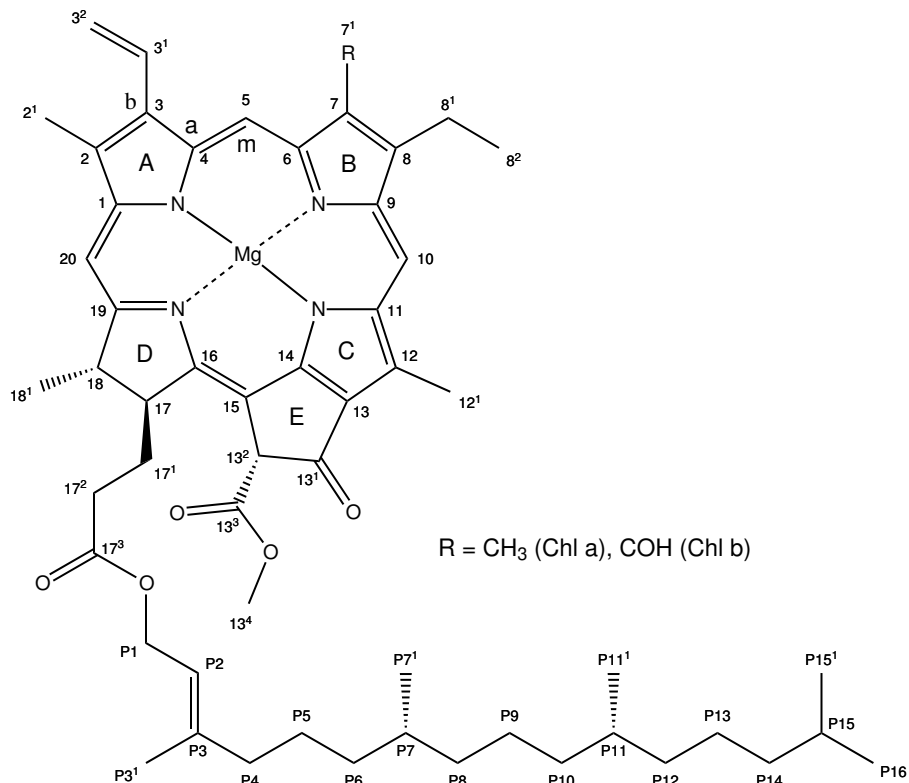


Figure 5.1: Structure of Chlorophyll molecule with IUPAC numbering and ring labels, and labelling of the distinct types of carbons on the porphyrin macrocycle ( $C_a$  and  $C_b$  on the pyrrole groups and  $C_m$  methine groups).

understanding of the spectral response of the relevant pigments in isolation. In this chapter, we present 2DEV spectra of isolated Chl *a* and Chl *b* dissolved in deuterated ethanol. By measuring the dependence of these spectra on the relative polarizations of the visible excitation and infrared (IR) probe laser pulses, in conjunction with density functional theory (DFT) calculations, we provide assignments for the major features of these spectra. We also provide evidence of features in the 2DEV spectra that correspond to different solvation states of the Chl molecules, distinguishing the contributions of pentacoordinate and hexacoordinate magnesium (Mg) species.

The 2DEV spectroscopic technique provides a method for correlating a molecule's electronic transitions, in the visible region of the electromagnetic spectrum, with its IR active vibrations.[127, 43, 108] The method is closely related to transient IR absorption pump-probe spectroscopy, whereby a molecule is electronically excited, and the resulting changes in the IR absorption is observed in a time resolved manner. Unlike transient IR absorption, however, 2DEV uses Fourier techniques to provide spectral resolution of the electronic excitation axis of the spectrum, in addition to the IR detection axis. This removes the trade-off

between temporal resolution and frequency resolution and reveals new types of information concerning correlations in the system.[43, 108, 107] 2DEV also makes it possible to more readily resolve and assign overlapping spectral features, by spreading the spectrum along an additional axis and thereby providing more information about their spectral structures.

An additional technique that can aid in providing assignments for bands in complex spectra is the use of the polarization dependent response and the spectral anisotropy. In combination, the isotropic (magic angle) response  $S_{iso}$ , the anisotropic response  $S_{aniso}$  and the anisotropy parameter  $r = S_{aniso}/S_{iso}$  can be used to assign spectral features based on the relative angles between their transition dipole moments.[102] The anisotropy parameter in particular is very useful, as for a spectrally isolated oscillator it can be directly related to the angle  $\theta$  between the transition dipole moments for the pumped and probed states, according to the well known relation  $r(\theta) = \frac{1}{5}(3\cos^2\theta - 1)$ . Because of this property, it is also possible to use the dynamics of the anisotropy parameter to measure such quantities as the rotational correlation function, or energy transfer dynamics.[94, 112] At a given waiting time, the anisotropy for a spectrally isolated transition is constrained to some frequency independent value in the region  $[-0.2, 0.4]$ . However, when spectral features of opposite sign interfere, it is possible for  $r$  to take on any value and demonstrate substantial spectral structure.[94] In this common scenario,  $r$  becomes much less useful as a quantitative measure of relative angles, but can still be used to identify features in complex spectra.

## 5.2 Results and Discussion

The transient IR pump-probe spectra of the high energy C=O and C=C stretch region of Chl *a* and Chl *b* are shown in Figure 5.2. In each case there are two major positive features, which are due to vibrations on the electronic ground state. The stronger of these appears at  $1660\text{ cm}^{-1}$  and is assignable to a C=O stretching motion. Based on a DFT harmonic frequency analysis this is most likely the antisymmetric combination of the C-13<sup>1</sup> ketone group and the C-13<sup>3</sup> ester group on ring E (see Figure 5.1 for labels). The weaker positive band appears around  $1550\text{ cm}^{-1}$ , and is attributable to a C=C stretch mode localized on the macrocycle. This band has been previously assigned to a combination of C<sub>b</sub>C<sub>b</sub> and C<sub>a</sub>C<sub>m</sub> stretching motions.[114, 83, 55] Based on the DFT results, this mode is primarily localized on rings C and E, and can be considered as predominantly a pyrrole stretching mode on ring C. In addition to these ground state vibrations, both the Chl *a* and the Chl *b* spectra show a strong negative band peaked near  $1615\text{ cm}^{-1}$ , and showing a long broad shoulder to lower frequencies. This band is most readily assignable to the carbonyl stretching mode on an electronic excited state. The shoulder might be due to either a second mode centered near  $1580\text{ cm}^{-1}$ , or to a positive ground electronic state feature interfering with the excited electronic state feature. The assignment of this shoulder will be made clear with the 2DEV spectra. In addition to these features common to both Chl species, the Chl *b* spectrum additionally shows a narrow negative feature at  $1640\text{ cm}^{-1}$ . This is unique to the Chl *b* spectrum, and therefore is likely related to the formyl group at position C-7<sup>1</sup> on ring B,

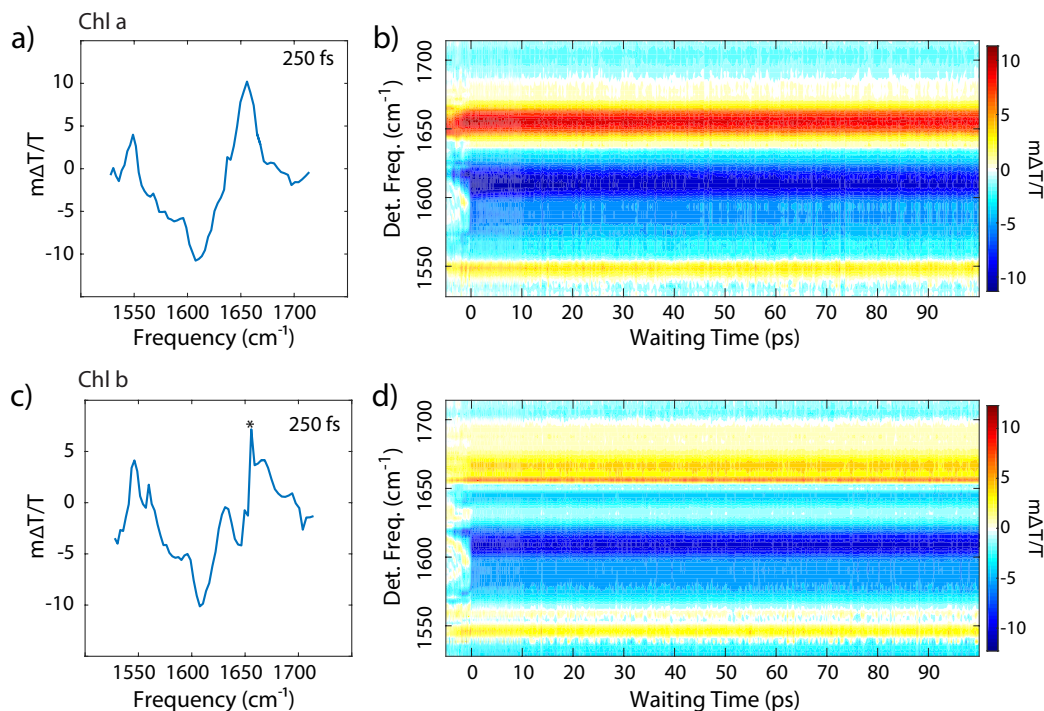


Figure 5.2: Isotropic transient IR absorption spectra of Chl *a* (a, b) and Chl *b* (c, d). Panels a) and c) show the transient spectra at waiting time  $t_2 = 250$  fs, and panels b) and d) show the full time resolved spectra. The positive (yellow/red) features indicate vibrations on the electronic ground state, and the negative (blue) features indicate vibrations on an electronic excited state. The \* in panel c) indicates an artifact introduced by atmospheric water.

which distinguishes Chl *b* from Chl *a* (see Figure 5.1). Because it is related to an electronic excited state and is not readily paired with an electronic ground state feature, it is difficult to assign precisely. It may be either a C=O stretch mode, or a distortion induced in a pyrrole mode on ring B due to the nearby electron withdrawing group. A sharp positive feature is also observed in the Chl *b* spectrum at 1655 cm<sup>-1</sup>, which is the result of an artifact caused by a depletion in the IR laser intensity by atmospheric H<sub>2</sub>O being incompletely normalized from the final spectrum, and is not indicative of a Chl *b* vibrational band. This artifact does not significantly affect the 2DEV spectra due to the greater degree of signal processing necessary for the construction of 2D spectra.

In making these assignments, we are proposing that all of the observed bands are results of primarily a  $1 \leftarrow 0$  vibrational transition, in which case the sign of the band is a direct indication of the electronic state on which this vibrational motion is occurring. It is also possible, in principle, to observe positive and negative features due to stimulated emission or induced absorption by excited vibrational states on either the ground or excited electronic states. These types of features would decay with the lifetime of the vibrational excited state, which would typically be on the order of  $\sim 1 - 10$  ps. All of the features in the current spectra

decay on a substantially longer timescale, commensurate with the  $Q_y$  lifetimes for isolated Chl *a* and Chl *b*.<sup>[158]</sup> Therefore we can rule out the possibility that the direct probing of vibrationally excited states are contributing significantly to these spectra.

The visible laser pulses used in these experiments had sufficient bandwidth to excite both the  $Q_y$  and the  $Q_x$  electronic transitions, for both Chl *a* and Chl *b*. The pump-probe spectra inherently integrate over both these contributions, but by performing 2DEV measurements, these features can be resolved. The polarization sensitive 2DEV spectra of both Chl *a* and Chl *b* are shown in Figure 5.3 for a waiting time  $t_2 = 250$  fs. This time was chosen to be late enough to prevent any contribution from pulse overlap effects, yet early enough to avoid any substantial orientational relaxation which would complicate the anisotropy data, though rotational contributions are also substantially suppressed by performing the experiments with the sample at 77 K (the rotational lifetime in ethanol at 77 K is  $\sim 100$  ns according to the Debye relation).<sup>[119]</sup> All of the major spectral features observed at this early time are maintained to at least 250 ps.

For the Chl *a* spectra in Figure 5.3 (a-c) there are clearly two major excitation bands, at around  $14650\text{ cm}^{-1}$  and  $15400\text{ cm}^{-1}$ . These structures are readily assignable from the electronic linear absorption. The intense anisotropic lower energy band is the  $Q_y$  transition, while the weaker isotropic band is the  $x$ -polarized feature known to be a mixture between the  $Q_x$  electronic transition and a vibronic excitation of the  $Q_y$  band.<sup>[141]</sup> Due to substantial overlap between different spectral bands, the precise angles between pumped and probed transition dipole moments cannot be readily extracted, but the qualitative polarization dependence of these bands is generally consistent with the assignments we have provided for these vibrational bands and the computed transition dipole moments for these modes. For the Chl *b* spectra shown in Figure 5.3 (d-f) there is an intense anisotropic band at  $15100\text{ cm}^{-1}$  which is due to the  $Q_y$  transition. Strong signals corresponding to exciting the  $Q_x$  transition are not observed for Chl *b*, but weak features located near  $16600\text{ cm}^{-1}$  could be due to this electronic excitation. It is unclear why the  $Q_x$  band is so weak in the Chl *b* spectra relative to those in the Chl *a* spectra, but this may be due to the lesser degree of vibronic mixing between  $Q_x$  and  $Q_y$  in Chl *b*,<sup>[141]</sup> or simply due to poorer overlap with the excitation laser spectrum.

It is important to note that while we certainly observe features in the 2DEV spectra that result from initially exciting the  $Q_x$  band, at least for Chl *a*, this does not imply that the  $Q_x$  electronic state has significant population at 250 fs. The lifetime of electronic relaxation from  $Q_x$  to  $Q_y$  has been calculated from non-adiabatic excited state molecular dynamics to be 128 fs for Chl *a* and 208 fs for Chl *b*.<sup>[16]</sup> In each case it is likely that the true rate is faster than observed in these calculations, due to the substantially overestimated  $Q_x - Q_y$  energy gap and the neglect of the vibronic mixing shown to exist between these states.<sup>[141]</sup> Therefore, by 250 fs, the majority of the population has already relaxed to the  $Q_y$  state, and the observation of spectral bands at the  $Q_x$  excitation energy are due to population in  $Q_y$  which merely originated as population in  $Q_x$ . The cross-correlation times of the visible and infrared laser pulses used in these experiments were measured to be  $\sim 90$  fs, comparable to the  $Q_x$  lifetime, and therefore it is unlikely that any vibrational features attributable to

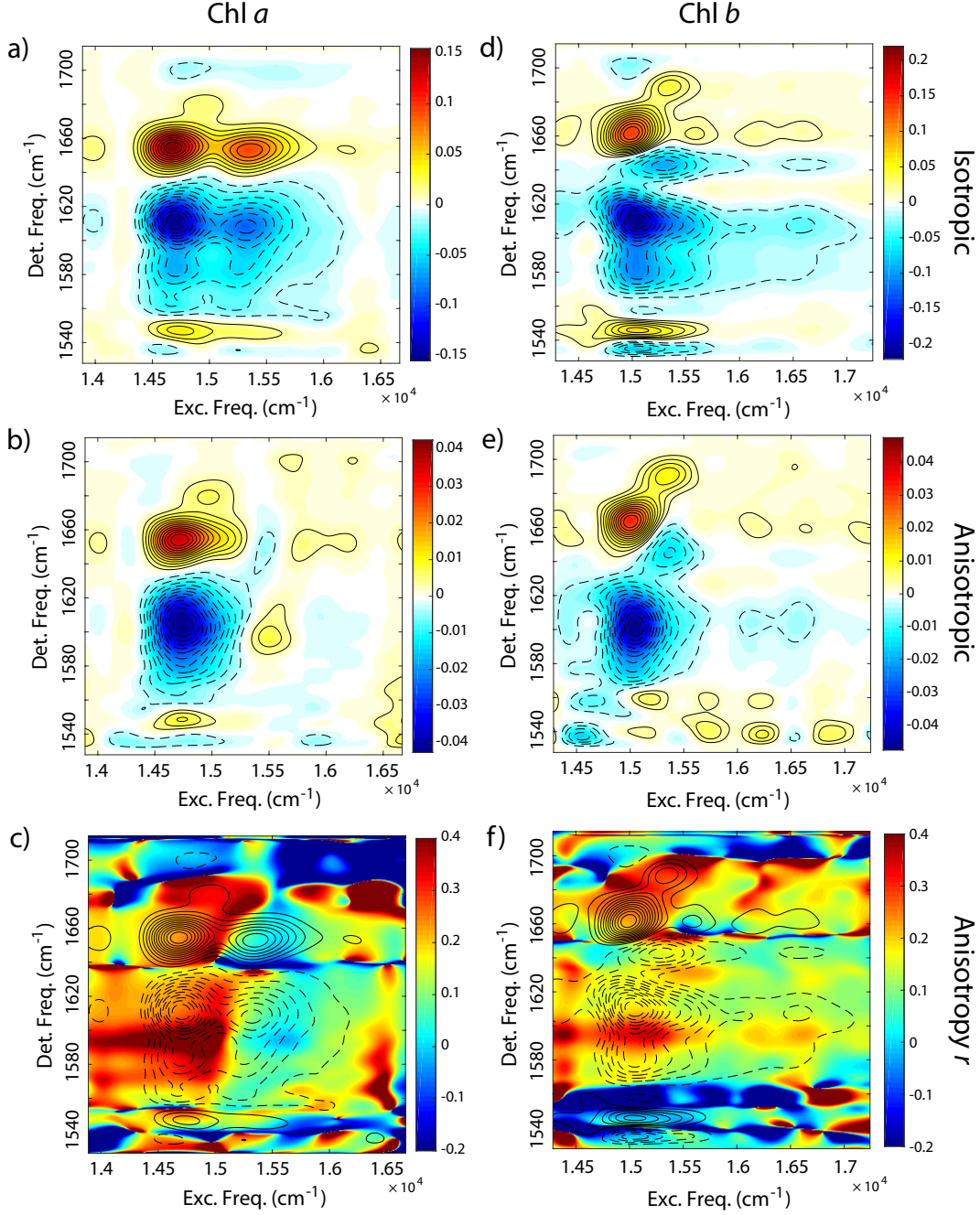


Figure 5.3: Polarization sensitive 2DEV spectra of the carbonyl stretch region of Chl *a* (a, b, c) and Chl *b* (d, e, f) at waiting time  $t_2 = 250$  fs. Solid contours indicate positive values for the spectrum, whereas dashed contours indicate negative values. The isotropic response  $S_{iso}$  is shown in panels a) and d), the anisotropic response  $S_{aniso}$  in panels b) and e), and the anisotropy parameter  $r$  is panels c) and f). The anisotropy values are overlaid by the contour plot of the isotropic spectra for the same waiting time. The value of  $r$  can diverge in the vicinity of nodes in the isotropic spectrum, so the color bars in panels c) and f) are truncated to  $[-0.2, 0.4]$ , the allowed range for an isolated transition.

population in the  $Q_x$  state could be observed with confidence in these 2DEV spectra.

For the isotropic response of both Chl *a* and Chl *b*, a significant shoulder on the low vibrational frequency side of the primary excited electronic state feature is observed. As mentioned previously this could reflect a second vibrational mode, but this interpretation is discredited by the anisotropic response shown in Figure 5.3 (b, e). For the anisotropic response of both molecules, there appears to be a single negative anisotropic feature. Indeed, by examining the anisotropy parameter  $r$ , shown in Figure 5.3 (c, f), a feature appears at around  $1590\text{ cm}^{-1}$  with very large values for the anisotropy, around 0.4 for Chl *b* and reaching 0.6 in the Chl *a* spectrum. For a region where the isotropic spectrum has significant amplitude, this type of structure in the anisotropy strongly implies that there is a positive feature at this position in the spectrum, as the only way to obtain a value for  $r$  greater than 0.4 is when multiple features with opposite sign interfere. In this case, because the positive band is not sufficiently intense to fully cancel the strong negative feature, the value for  $r$  does not diverge, but in the case where the negative feature is anisotropic (as is here) with a sufficiently strong, primarily isotropic positive feature,  $r$  can take on an arbitrarily large value. In this case, the positive feature is due to the well known band observed in the ground state IR absorption and resonance Raman of metallochlorins.[114, 83, 55] This vibrational mode is delocalized over the majority of the chlorin macrocycle, with a character of predominantly a  $C_aC_m$  stretch with some contribution of a  $C_bC_b$  stretch. The structure of the anisotropy does not allow us to determine with certainty whether the anisotropic negative feature is composed of a single broadened vibrational transition (presumably with C=O stretch character) or of two modes, with a lower energy transition related to the C=C mode. For both the Chl *a* and Chl *b* anisotropic spectra this feature has the qualitative appearance of a single band, which seems to suggest that it is likely to be predominantly due to a single broad transition.

So far, we have provided assignments for most of the major features appearing in the transient IR absorption and 2DEV spectra. There are, however, several smaller features that are evident in the 2DEV spectra for which the assignments are less immediately obvious. These include weak positive bands that appear in both the Chl *a* and Chl *b* spectra at higher energies than the ground electronic state C=O stretch mode at  $1660\text{ cm}^{-1}$  along both axes, as well as a substantial negative feature in the Chl *b* spectra displaced to higher energies along both axes from the dominant excited electronic state feature. The positive feature in the Chl *a* spectra appears at an excitation frequency of  $\sim 14900\text{ cm}^{-1}$  and a detection frequency of  $1680\text{ cm}^{-1}$ , while the corresponding feature in the Chl *b* spectra appears at an excitation frequency near  $\sim 15350\text{ cm}^{-1}$  and a detection frequency of  $1690\text{ cm}^{-1}$ . The negative feature appears at roughly the same excitation frequency, with a detection frequency near  $1640\text{ cm}^{-1}$ . The assignment of these features is not immediately clear, as there is no known electronic excited state that lies between  $Q_y$  and  $Q_x$ , and they decay on the timescale of  $Q_y$  relaxation and therefore cannot be attributed to vibrational excited states.

We propose that these features are due to different coordination states of the central Mg. In nucleophilic solvents, like ethanol, it is possible for the Mg to exist in either a pentacoordinate or a hexacoordinate states, in which it has bound to either one or two

Table 5.1: Chl  $S_1 \leftarrow S_0$  excitation energies ( $\text{cm}^{-1}$ )

	No. ethanol molecules			
	0	1 $Z$	1 $E$	2
Chl $a$	18346	18326	18213	18092
Chl $b$	18271	18159	18031	17769

solvent molecules. It has been shown using resonance Raman and IR absorption that for Chl and Bacteriochlorophyll (BChl) these two solvation states can be distinguished using several vibrational bands in this high frequency region.[36, 114, 61] These studies show that for Chl  $a$ , Chl  $b$  and BChl  $a$  in methanol, the dominant species is the hexacoordinate state. For ethanol, both configurations are present, with Cotton and Van Duyne showing that Bchl  $a$  is predominantly in the hexacoordinate state while Fujiwara and Tasumi argue that this is reversed for Chl  $a$  and  $b$ , which are predominantly pentacoordinate.[36, 61] In addition to these vibrational spectroscopies, it has been argued by J. J. Katz and co. that these solvation states can be distinguished by shifts in the electronic absorption spectra of the  $Q$  bands.[35, 50] For Chl  $a$  dissolved in methanol, they show that in addition to the primary  $Q_y$  absorption at 665 nm that is due to the hexacoordinate species, there is also a minor component located at 650 nm which they attribute to the pentacoordinate state. Using 2DEV we can correlate these shifts along the electronic and vibrational axes, and provide direct evidence that they are indeed due to the same species.

In contrast to previous work, we conclude that in ethanol the hexacoordinate state is the dominant species for both Chl  $a$  and Chl  $b$ . While not impossible, it would be surprising if such a dramatic change in the dominant solvation state of the Mg would arise due to the differences between methanol and ethanol, or between Chl and BChl. It is also possible that this has a temperature dependence, as has been demonstrated that in n-propylether, BChl forms a mixture of penta- and hexacoordinate at 228 K, but becomes entirely hexacoordinate at 160 K.[50]

To confirm our assignment of the blue-shifted bands as a minority population of pentacoordinate Chl molecules, we performed a series of DFT and time-dependent DFT (TD-DFT) calculations on isolated Chl  $a$  and Chl  $b$ , on these species with a single ethanol molecule coordinated to the face of the molecule either  $E$  or  $Z$  with respect to the phytol chain, and with the Mg coordinated to two ethanol molecules, one on each face. For each of the equilibrium ground state geometries for both Chl  $a$  and Chl  $b$  in the various solvation states, we performed TD-DFT calculations to determine estimates for the  $S_1 \leftarrow S_0$  excitation energies. In each case, the calculation correctly identified  $S_1$  with the  $Q_y$  transition. The results of these calculations are shown in Table 6.1. For Chl  $a$ , the energy difference between the hexacoordinate species and the  $Z$  pentacoordinate species is  $234 \text{ cm}^{-1}$ , and for the  $E$  pentacoordinate species is  $121 \text{ cm}^{-1}$ . For Chl  $b$  these differences are  $390 \text{ cm}^{-1}$  and  $262 \text{ cm}^{-1}$ , respectively. These values compare reasonably well to the observed energy differences of

$\sim 250 \text{ cm}^{-1}$  for Chl *a* and  $\sim 340 \text{ cm}^{-1}$  for Chl *b*. The TD-DFT calculations may not quantitatively predict the correct energy differences, but it does correctly predict the smaller energy difference for Chl *a* compared to Chl *b*. These values for the changes in electronic excitation energy for the various solvation states, together with the previously observed differences in the vibrational and electronic absorption spectra for the different states suggest that this is a plausible assignment for these spectral features, and that, at least at low temperature, the hexacoordinate species is the dominant solvation state for Chl *a* and Chl *b* in ethanol.

In principle, it should be possible to use the 2DEV spectra to measure the exchange rate between the different coordination states of the Mg, in a similar manner as has been demonstrated with 2DIR spectroscopies. [175, 182] We do not see evidence of a significant degree of exchange between these species, for either Chl *a* or Chl *b*, within 250 ps. Given that these experiments were performed at cryogenic temperatures (77 K), with any significant energetic barrier separating the different species, and with diffusion essentially eliminated, such a slow rate of exchange is reasonable. It would be interesting in future work to study the temperature dependence of the 2DEV spectra to determine the magnitude of this energy barrier between the pentacoordinate and hexacoordinate Chl species in varying solvents, as well as to study how the ratio between these species changes at higher temperatures.

### 5.3 Conclusion

To conclude, we have presented transient IR absorption spectra and 2DEV spectra of isolated Chl *a* and Chl *b* dissolved in deuterated ethanol and held at 77 K. We have provided assignments for the major spectral features that appear in the  $1540 - 1700 \text{ cm}^{-1}$  spectral region, including bands assignable to C=O and C=C stretch modes on the electronic ground state, and the C=O stretch on the  $Q_y$  electronic excited state. For Chl *a* we observe strong features due to initial excitation of the  $Q_x$  band, which either do not appear or are very weak in the Chl *b* spectra. The assignments were made by comparing the observed spectra with the well known IR and resonance Raman spectra of these Chl species, using DFT calculations, and by taking advantage of the polarization dependence of the spectra, which is capable of revealing spectral features which cannot be otherwise resolved. We have also observed features resolvable from the main  $Q_y$  bands along both the electronic and the vibrational axes, which we assign to be the different solvation states of the Chl molecules, with either a pentacoordinate or a hexacoordinate Mg. This work demonstrates the potential usefulness of 2DEV as a technique for distinguishing molecular conformers, and serves as an important first step towards using 2DEV to study the electronic and vibrational properties of photosynthetic PPCs.



## 5.4 Methods

### 5.4.1 Two-Dimensional Electronic-Vibrational Spectroscopy

The 2DEV technique has been described in detail previously, in chapter 2.[127] Briefly, the experiment was driven by a Ti:Saph regenerative amplifier (Coherent; Legend Elite USP; 806 nm, 40 fs, 0.9 mJ, 1 kHz) seeded by a Ti:Saph oscillator (Coherent; Micra). This was used to pump a home-built optical parametric amplifier (OPA) with difference frequency generation and a home-built non-collinear OPA (NOPA). The OPA was tuned to generate  $\sim 300$  nJ pulses centered at  $6.1 \mu\text{m}$  with a pulse duration of  $\sim 80$  fs. This beam was split by a 50:50 ZnSe beamsplitter to generate the probe and reference beams, which were subsequently focused to  $\sim 200 \mu\text{m}$  spots by a  $f = 15$  cm gold coated  $90^\circ$  off-axis parabolic mirror. The reference beam was displaced so that it would not overlap with the pump or probe beams at the sample. After the sample, the probe and reference beams were dispersed in an imaging spectrometer (Horiba; Triax 180) and detected with a dual-array HgCdTe detector with 64 elements per array (Infrared Systems Development). The reference beam was used to normalize the probe spectrum and to compensate for instability in the laser intensity on a shot-by-shot basis.

The NOPA was used to generate  $3.5 \mu\text{J}$  broadband pulses spanning  $\sim 500 - 800$  nm. The beam was passed through an acousto-optic programmable dispersive filter (AOPDF) (Fastlite; Dazzler). For the Chl *a* samples, the beam was attenuated to 315 nJ and limited to 120 nm total bandwidth centered at 660 nm and compressed at the sample position to 22 fs. For the Chl *b* samples, the beam was attenuated to 350 nJ and limited to 120 nm total bandwidth centered at 640 nm and compressed at the sample position to 18 fs. The NOPA spectra are shown in Figure 5.4. The AOPDF was additionally used to split the pump beam into two degenerate pulses, with a controllable time delay  $t_1$  and phase  $\phi_1$  between the two pulses. Subsequent to the AOPDF, the pump beam was bounced off a retroreflector on a controllable delay stage to control the time delay  $t_2$  between the pump pulse pair and the probe pulse, and focused to a  $\sim 250 \mu\text{m}$  spot at the sample by a  $f = 25$  cm silver coated  $90^\circ$  off-axis parabolic mirror. The relative polarization between the pump pulses and the probe pulse was controlled with a  $\lambda/2$  waveplate in the pump beam. The isotropic response  $S_{iso}$  and anisotropic response  $S_{ansio}$  were constructed from the parallel  $S_{\parallel}$  and perpendicular  $S_{\perp}$  spectra using the relations  $S_{iso} = S_{\parallel} + 2S_{\perp}$  and  $S_{ansio} = S_{\parallel} - S_{\perp}$ . The cross-correlation time between the pump pulse and probe pulse was found to be  $\sim 90$  fs.

For a given waiting time  $t_2$  between the pump pulses and the probe pulse, a 2DEV spectrum was acquired by scanning  $t_1$  from  $0 - 75$  fs in 2.4 fs steps and the desired signal was isolated by phase cycling with respect to  $\phi_1$  in a  $4 \times 1 \times 1$  phase cycling scheme.[122] The signal was collected in the fully rotated frame with respect to  $t_1$  to remove the optical frequency of the pump laser. It was not necessary to phase the signal by fitting to a separate pump-probe experiment, due to the partially collinear geometry used in this setup.[64]

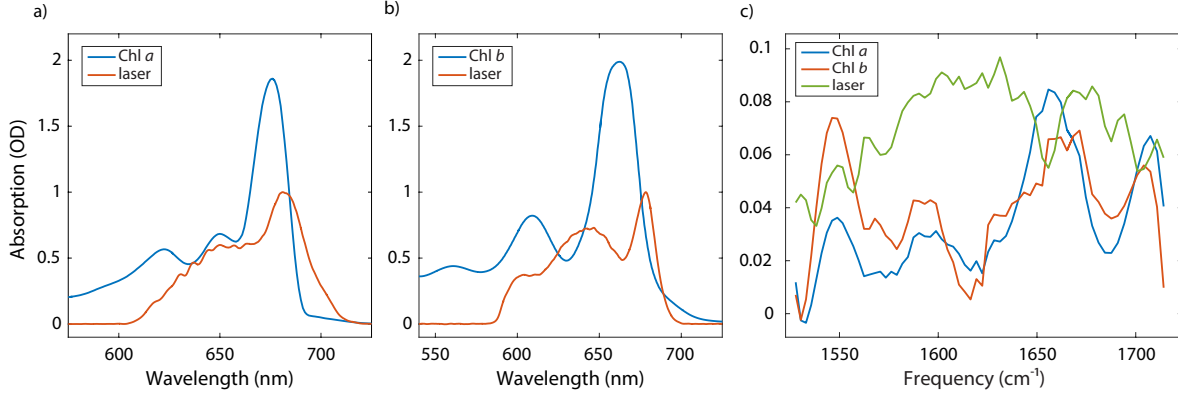


Figure 5.4: Electronic (a, b) and solvent-subtracted vibrational (c) linear absorption of Chl *a* and Chl *b*. Superimposed in red (a, b) and green (c) are the laser spectra (normalized) used to excite these electronic transitions. The IR laser spectrum in (c) is normalized to 0.1.

### 5.4.2 Sample

The experiments were performed with the sample held at 77 K in a cryostat (Oxford Instruments; OptistatDN2) with CaF<sub>2</sub> outer windows and ZnS inner windows. The Chl *a* and Chl *b* samples were both purchased from Sigma Aldrich and used without further purification. The samples were dissolved in fully deuterated ethanol purchased from Cambridge Isotopes to an optical density of  $\sim 2$  at the absorption maximum of the  $Q_y$  electronic transition in a sample cell composed of two CaF<sub>2</sub> windows separated by a 100  $\mu\text{m}$  thick kapton spacer. This concentration corresponds to an optical density of  $\sim 0.04 - 0.1$  for the vibrations. The linear electronic absorption spectra, with the cryostat background subtracted, and the solvent-subtracted IR absorption spectra are shown in Figure 5.4.

The high optical density of the sample in the visible, and the relatively high pump laser power deserve some discussion. It has been shown that the use of high optical density samples can introduce distortions to degenerate 2D spectra.[180, 110] Several of the mechanisms for these distortions are strongly dependent on the experimental geometry, and become far less significant in the pump-probe geometry used here. This is due primarily to the unimportance of phase-matching, and the co-propagation of the local oscillator with the signal. Indeed, it has been demonstrated that experiments performed in this geometry are less sensitive to these distortions.[177] The remaining distortion mechanisms that depend directly on the optical density are due to the reshaping of the pump spectrum by the sample absorption, and the reabsorption of the signal. The latter of these effects is effectively irrelevant for the current work, due to the very low optical densities of the vibrational transitions. The primary effect of the reshaping of the pump spectrum is to induce broadening of the spectrum along the excitation axis. The magnitude of this effect has been shown to be on the order of  $\sim 10 \text{ cm}^{-1}$ , which is relatively unimportant for the current experiments.[177, 110] Furthermore, we do not rely on the spectral linewidths for the results of this work, so its effect on these

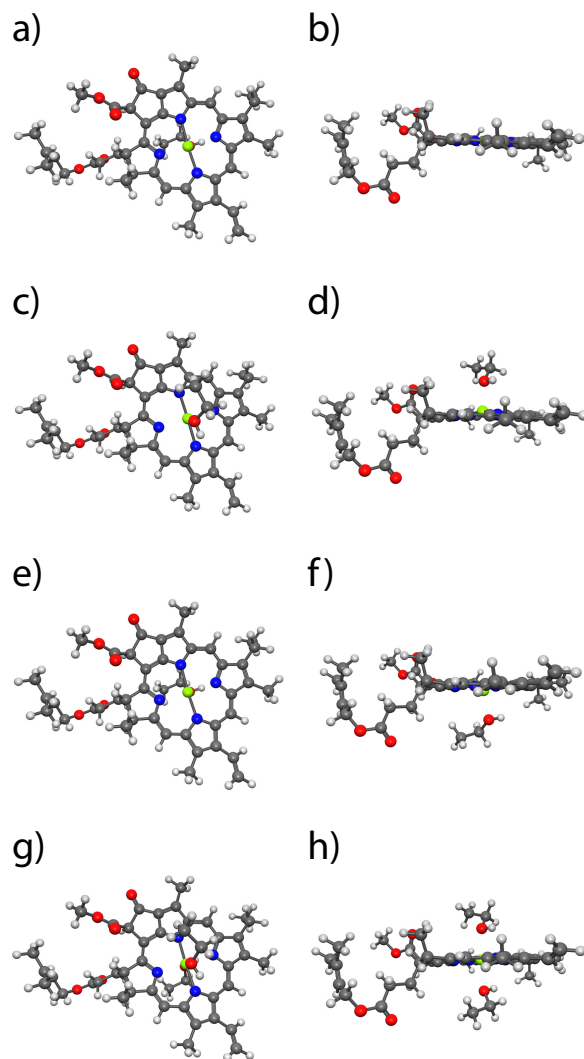


Figure 5.5: Ground state equilibrium geometries of Chl *a* with 0 ethanol molecules (a, b), with 1 ethanol molecule bound to the face *E* to the phytyl chain (c, d), on the face *Z* to the phytyl chain (e, f) and with 2 ethanol molecules (g, h).

results are minimal. The high pump laser power is mitigated by the large focal spots used in this experiment, so that the actual photon flux is not substantially larger than generally considered acceptable for 2D electronic spectroscopy. The sample was monitored for laser-induced degradation, and none was observed.

### 5.4.3 Electronic Structure Calculations

Density functional theory (DFT) calculations were performed using the Q-Chem 4.32 computational package.[153] All calculations were performed *in vacuo* with the B3LYP functional and the 6-31G(d,p) basis set. The equilibrium geometries were calculated for each Chl *a* and Chl *b* as isolated molecules, coordinated through the Mg to a single ethanol molecule on either face of the macrocycle as well as coordinated to two ethanol molecules with a  $D_{4h}$  type symmetry about the Mg. For each of these coordination states a harmonic vibrational analysis was performed for the ground electronic states. Additionally, the transition energy for the  $Q_y$  and  $Q_x$  transitions were calculated using TD-DFT under the Tamm-Dancoff approximation. The equilibrium structures in Cartesian coordinates can be provided upon request.

To reduce the cost of these calculations, the phytyl chains were truncated at position C–P4, subsequent to the olefin moiety. The relaxed ground state geometries for the various Chl *a* species are shown in Figure 5.5. The structures for Chl *b* were found to be similar. For both the four-coordinate (no ethanols) and the hexacoordinate (two ethanols) species, the chlorin macrocycle was found to be highly planar, with N-Mg-N angles close to  $180^\circ$  with respect to the plane of the macrocycle (the Mg is shifted slightly away from the center of the macrocycle, so the exact N-Mg-N angle is close to  $177^\circ$ ). For the pentacoordinate species, however, the macrocycle is significantly distorted from planarity, with the Mg pulled out of the plane of the molecule and the ring distorted, so that the N-Mg-N angles become close to  $163^\circ$ , and the entire macrocycle becomes somewhat puckered. The observation that the chlorin ring becomes deformed in certain solvation states, and that the Mg serves as the primary site for solvation by nucleophilic solvents, is not new, and has been used to explain shifts in the low energy Raman Mg-N modes.[114]

## Chapter 6

# Spatio-Energetic Dynamics in Light Harvesting Complex II

### 6.1 Introduction

Light harvesting complex II (LHCII) is the major photosynthetic antenna complex for higher plants. It comprises a substantial fraction of the protein content in the thylakoid membrane, and binds a majority of the chlorophyll (Chl) *a* and *b* found in plants.[12] In the membrane, LHCII forms a trimer with pseudo- $C_3$  symmetry. Each monomer binds 14 Chl molecules, typically 8 Chl *a* and 6 Chl *b*, as well as four carotenoids – two luteins, one neoxanthin and one violaxanthin, which is believed to interconvert according to the violaxanthin-antheraxanthin-zeaxanthin cycle.[6] The positions of the chlorophyll molecules inside the LHCII trimer are shown in figure 6.1. The Chls serve primarily as light harvesting pigments, absorbing solar photons and transferring the electronic excitation energy to the photosystem II (PSII) reaction center. The role of the various carotenoids is rather more complex, as they can function both in light harvesting and in photoprotection.[57, 172, 85, 148, 3, 111, 59]

LHCII is responsible for the majority of light absorption associated with PSII. Because of this central role in oxygenic photosynthesis, the structure and the detail of the electronic excitation dynamics in LHCII have been thoroughly characterized,[6] using a wide variety of techniques, ranging from x-ray crystallography,[97, 113] genetic manipulation,[142, 37] and structure-based modeling[67, 124] to a broad variety of steady-state and time resolved spectroscopies,[48, 79, 45, 11, 2, 167, 136, 150] including a series of recent studies utilizing two-dimensional electronic spectroscopy (2DES).[149, 21, 151, 46] However, there remain limits on our understanding that are imposed, in large part, by the limitations of the techniques which have been hitherto available.

All spectroscopic methods which rely solely on interaction with electronic transitions suffer from the same defect, which is related ultimately to the difficulty in separating the effects of differences in electronic site energies of individual pigments and of electronic cou-

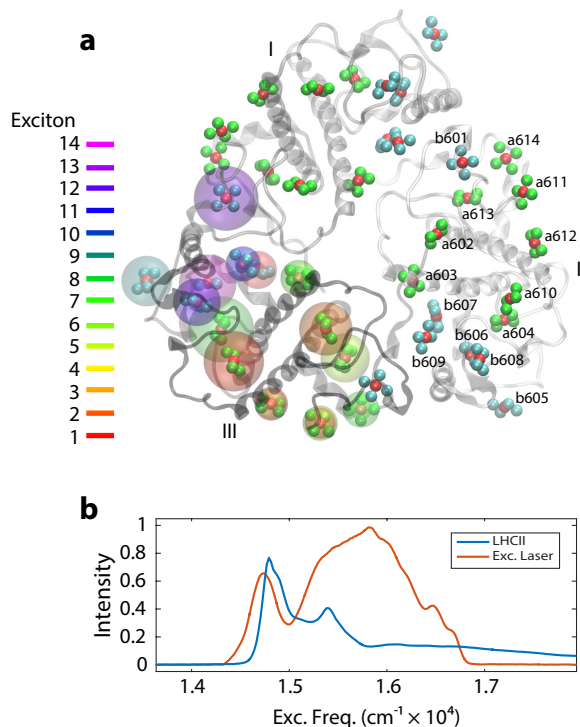


Figure 6.1: (a) Structure of LHCII trimer viewed from the stromal surface, from the 2.72 Å x-ray crystal structure.[113, 86] The Chl *a* and *b* are represented by their Mg (red spheres) and N (Chl *a* green, Chl *b* cyan). The carotenoids and lipids are omitted for clarity. The Chl ligands in monomer II are labelled with the crystal structure numbers. The Chl ligands in monomer III are marked with colored orbs, where the color indicates the 14 exciton states. The size of each orb indicates the degree to which that site contributes to the exciton, according to the Novoderezhkin Hamiltonian.[124] (b) The electronic absorption spectrum of LHCII at 77 K, together with the normalized excitation laser spectrum.

pling between pigments. Electronic transitions occur between eigenstates of the electronic Hamiltonian, which in complex systems are often not easily related to the site basis of actual pigments and their positions. This fact necessitates sophisticated modeling efforts to provide the link between the electronic spectroscopies and the actual flow of the excitation energy through the complex, which is typically the goal of these studies. A variety of techniques based on a combination of structural and spectroscopic information have been developed to address this issue for photosynthetic light harvesting complexes,[67, 1] and progress has also been made in addressing these questions using quantum chemistry techniques,[155, 82, 159, 23, 38] but a significant degree of ambiguity and uncertainty remains. Additional complexities arise from the fact that the site basis is generally the natural basis in which to describe the environment and the interactions between the environment and the electronic excited states, and that the strength of the coupling to the environment is typically of the

same order of magnitude as the strength of the electronic coupling between pigments, and the thermal energy  $k_B T$ . Thus, accurate quantum dynamics simulations must rely on computationally expensive exact methods,[89, 88] or on approximation schemes that must balance accuracy with cost.[67, 124, 144, 10] The spatial organization of the electronic eigenstates according to the best currently available Hamiltonians developed using these modeling procedures is shown in figure 6.1, but an experimental approach capable of directly providing this link between the electronic eigenstates and the site basis would be of great value in the research of photosynthetic light harvesting.

In chapter 4, we proposed an experimental method by which this direct link might be obtained, based on 2D electronic-vibrational (2DEV) spectroscopy.[127, 107] 2DEV spectroscopy is a two-color coherent multidimensional spectroscopic technique that is capable of directly correlating the electronic transitions of a molecule with its vibrational structure, by using a combination of visible and mid-infrared (IR) laser pulses.[127, 43, 108] The essential idea is to leverage the local character of certain high frequency Chl vibrational modes, and use these localized vibrations as a proxy for position within the large protein complex. The pigments are located in different positions within the protein, and are therefore exposed to slightly different electrostatic fields induced by the protein. Furthermore, the differences in the various binding pockets induce different minor structural deformations in the Chls located at each binding site, and bind the Chl to the protein using different axial ligands and hydrogen bonding configurations.[113] Together, these effects cause shifts in the frequencies of various high energy vibrations, making it possible, in principle, to identify specific sites by their vibrational bands. These are the same effects which result in different electronic energies for each site. However, unlike the electronic absorption spectrum, which is determined by both the site energies as well as the electronic couplings, the vibrational spectrum of the individual pigments is not likely to be strongly affected by dipole interactions with neighboring pigments. Therefore, so long as it is possible to assign vibrational bands to specific pigments, it should be possible to use 2DEV spectroscopy to directly relate the electronic excitation spectrum and the excited state energy transfer dynamics to specific sites within the complex.

Here, we present 2DEV spectra of the Chl *a* and Chl *b* *Q* bands in isolated LHCII trimers and demonstrate how different bands display different dynamics, depending on the both the electronic state that is excited as well as the vibration that is probed. Some of these features, such as the relaxation from Chl *b* site to Chl *a* sites, are easy to assign, and provide us with an unambiguous measurement of these relaxation dynamics, potentially revealing discrepancies with the best available Hamiltonians for LHCII. Other vibrational bands are more difficult to localize, and at present can only be tentatively assigned based on their dynamics and the available Hamiltonians. These results compare favorably to previous transient IR spectra of LHCII, which, due to the nature of transient absorption spectroscopy, suffered from limitations in spectral and temporal resolution, hindering the degree of information that could be extracted.[161] We expect that a combination of mutant studies, theoretical calculations of vibrational electrochromic shifts and high level QM/MM simulations will make the assignments of these bands possible, thereby placing these measurements among

the most detailed experimental studies of the electronic relaxation dynamics in LHCII, or any other photosynthetic light harvesting complex, to date.

## 6.2 Results and Discussion

We present the discussion of the results in three parts. In section 6.2.1 we provide assignments for the major features observed in the 2DEV spectra of LHCII, given in comparison to 2DEV spectra of isolated Chl *a* and Chl *b*. In section 6.2.2 we qualitatively describe the dynamics observed in the spectra. Finally, in section 6.2.3, we perform a principal component analysis of the LHCII spectra based on the singular value decomposition (SVD), and provide a more quantitative analysis of the timescales and dynamics observed in these spectra.

### 6.2.1 Spectral Assignments

2DEV spectra of isolated Chl *a* and Chl *b* and of LHCII at an early waiting time  $t_2 = 0.25$  ps, prior to the majority of the exciton transfer and relaxation, are shown in figure 6.2. The features in spectra of the isolated chromophores have been assigned in detail in chapter 5,[106] but for clarity we will briefly discuss them here. These spectra are dominated by several broad structures along the detection axis  $\omega_3$ . The intense bleach features at  $\omega_3 = 1655 \text{ cm}^{-1}$  in the Chl *a* spectra and at  $1665 \text{ cm}^{-1}$  in the Chl *b* spectra are assigned to C=O stretch modes, while the broad excited state absorptions peaking near  $1610 \text{ cm}^{-1}$  are most likely due to the analogous modes on the electronic excited states. Less intense bleaches are observed at  $1550 \text{ cm}^{-1}$  and as depletions in the excited state feature near  $1590 \text{ cm}^{-1}$  are assigned to chlorin ring-stretching modes. Along the excitation axis  $\omega_1$  of the Chl *a* spectra, two major features are observed, at  $14650 \text{ cm}^{-1}$  and  $15400 \text{ cm}^{-1}$ , corresponding to excitation of the electronic transitions that dominate the visible linear absorption spectrum – the lower energy  $Q_y$  band, and the higher energy band that arises from a vibronic mixture of  $Q_y$  and  $Q_x$ . [141] In the Chl *b* spectra shown in figure 6.2 (b), the  $Q_y$  band dominates at  $\omega_1 = 15000 \text{ cm}^{-1}$ , and the  $Q_x$  associated bands appear as weak features near  $\omega_1 = 16500 \text{ cm}^{-1}$ . In addition to these major spectral features, there are also weaker bands which are important to discuss, particularly a weak bleach band in the Chl *a* spectra at  $\omega_1 = 14900 \text{ cm}^{-1}$  and  $\omega_3 = 1680 \text{ cm}^{-1}$ , and two moderate intensity bands in the Chl *b* spectra at  $\omega_1 = 15350 \text{ cm}^{-1}$ , a bleach at  $\omega_3 = 1690 \text{ cm}^{-1}$  and an excited state absorption at  $1640 \text{ cm}^{-1}$ . These features are due to the five-coordinate Chl molecules, where the central Mg is axially bound to only a single solvent molecule, as opposed to the major features of the spectra, which arise from the six-coordinate species, axially coordinated by two solvent molecules.[106] According to the crystal structure of LHCII,[113] the majority of the Chl pigments are either four- or five-coordinate, and so the spectral positions of these peaks should be expected to be more similar to the features observed in the LHCII spectra.

The 2DEV spectrum of LHCII shown in figure 6.2 (c) shows several bands that can be readily related to the spectra of Chl *a* and Chl *b*. The spectrum shows two major electronic



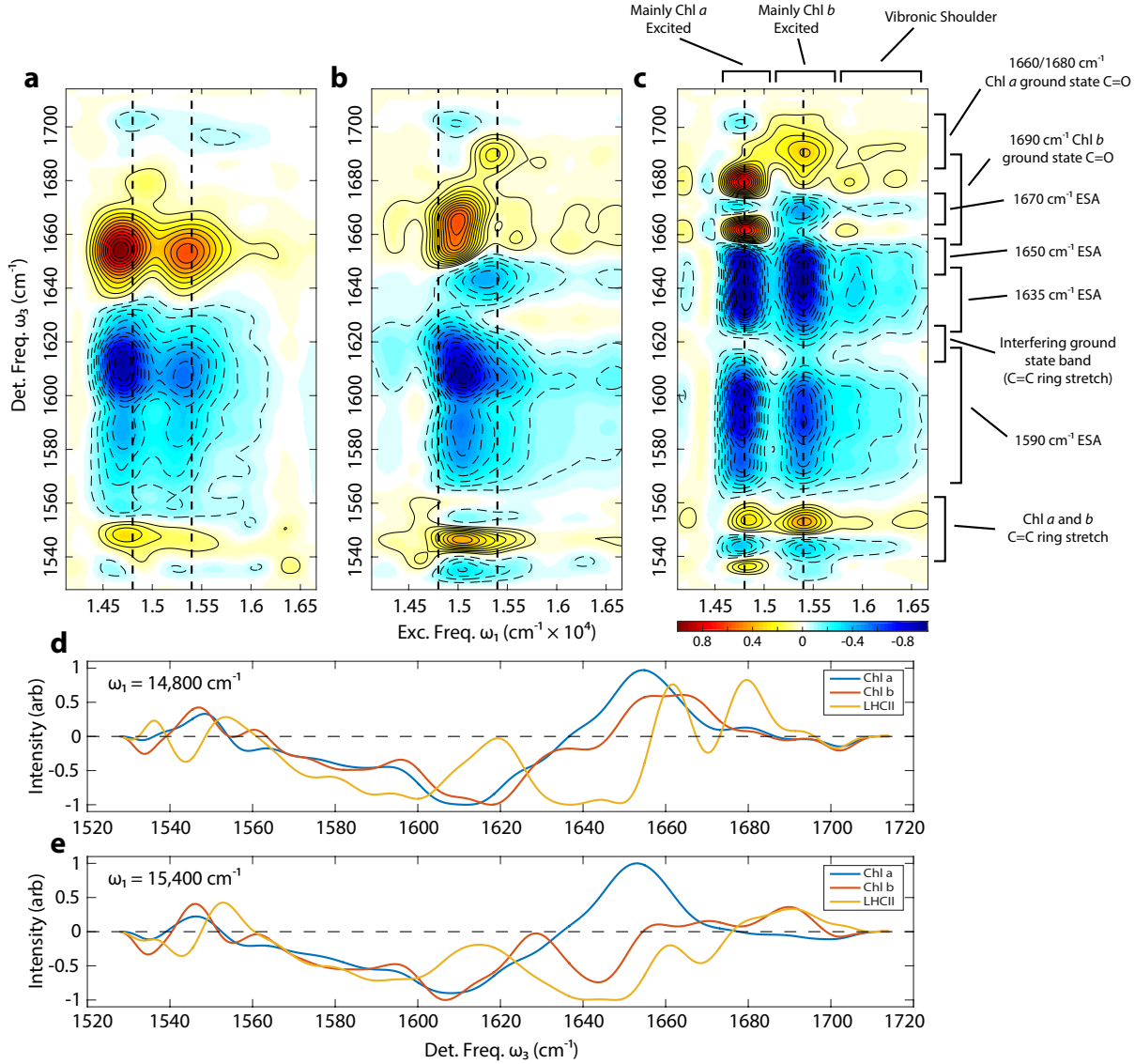


Figure 6.2: 2DEV spectra of Chl *a* (a), Chl *b* (b) and LHCII (c) at  $t_2 = 250$  fs. The positive features shown in yellow-red and solid contours indicate the bleach of the vibrational modes on the ground excited state, and the negative features shown in blue and dashed contours indicate absorptions by vibrations on the electronic excited states. Each spectrum is normalized relative to its own absolute maximum. The dashed lines at  $\omega_1 = 14800$  cm<sup>-1</sup> and  $15400$  cm<sup>-1</sup> mark the location of the slices shown in (d) and (e). The assignments of the bands of the LHCII spectrum (c) have been labeled.

excitation bands at  $\omega_1 = 14800$  and  $15400$  cm<sup>-1</sup>, as well as a low intensity shoulder to higher excitation energies. These structures can be understood in direct relationship to the LHCII linear visible absorption spectrum shown in figure 6.1 (b). The  $14800$  cm<sup>-1</sup> band has been

assigned as a combination of several electronic states associated with Chl *a*  $Q_y$  transitions, while the  $15400\text{ cm}^{-1}$  band arises primarily from Chl *b* transitions, with some contribution from higher energy Chl *a* states.[149, 124] Presumably, this band also contains contributions from Chl *a*  $Q_x$  transitions, which in isolation occur at a similar energy. The higher energy shoulder, which extends past  $16500\text{ cm}^{-1}$ , is due to the  $Q_x$  transitions and higher energy vibronic excitations.

Along the detection axis  $\omega_3$ , there are several features which can be directly assigned based on comparison to the 2DEV spectra of the isolated chromophores. Slices through the Chl *a*, Chl *b* and LHCII spectra at  $\omega_1 = 14800$  and  $15400\text{ cm}^{-1}$  are shown in figure 6.2 (d) and (e) to facilitate the comparison between these spectra. The bleach feature at  $\omega_1 = 15400\text{ cm}^{-1}$  and  $\omega_3 = 1690\text{ cm}^{-1}$  is a clear indication of populated Chl *b* in LHCII, being located at precisely the same spectral location as the bleach of the five-coordinate Chl *b* in the isolated chromophore. The two prominent positive features in the LHCII spectrum located at  $\omega_1 = 14800\text{ cm}^{-1}$  and at  $\omega_3 = 1660$  and  $1680\text{ cm}^{-1}$  undergo identical dynamics and most likely arise from the same underlying band, corresponding to the ground electronic state C=O stretch of the Chl *a*, with an interfering excited state band at  $\omega_3 = 1670\text{ cm}^{-1}$ . An excited state band corresponding to the same vibrational mode can be clearly observed at the early waiting times for initial excitation to the higher energy electronic band, at  $\omega_1 = 15400\text{ cm}^{-1}$ . It is unclear whether this excited state band corresponds to a mode on Chl *a*, on Chl *b* or on both, as this band does not appear in the 2DEV spectra of the isolated chromophores. Another possibility is that this band arises from distortions induced in nearby protein vibrations due the excitation of a Chl. According to the  $2.72\text{ \AA}$  crystal structure, a number of the Chl ligands are coordinated to the side chain of a glutamate moiety (a602, b609, a610), an asparagine moiety (a612) or a glutamine moiety (a613), or to a backbone carbonyl (b601, b605). Each of these amino acids possess vibrational modes with frequencies near  $1670\text{ cm}^{-1}$ , [8] mostly with C=O stretch character. If the frequency or absorption strength of these protein modes is altered by the electronic excitation of the coordinated Chl, this could potentially explain the appearance of the new induced absorption band.

In addition to these bleach bands which can be used to identify excited state population on Chl *a* and Chl *b*, the bleach of a chlorin ring stretching mode is observed at  $\omega_3 = 1555\text{ cm}^{-1}$  across the whole excitation band. This band appears to be blue-shifted by  $\sim 5\text{ cm}^{-1}$  relative to the corresponding band in the spectra of the isolated pigments. This shift can be explained by interactions between the pigments and the protein. The Chls bound to proteins are generally not entirely planar, as observed in the crystal structure,[113] due to the coordination state and the structures of the binding pockets. Furthermore, many of the pigments are in close proximity to charged amino acid residues, so the shift of this band could also be caused by some combination of the vibrational electrochromic shift induced by the electrostatic charges of the protein,[134, 29, 31] and hydrogen bonding interactions.

The 2DEV spectra of LHCII shown in figures 6.2 (c) and 6.3 (a-d) are dominated by broad negative features, which correspond to absorption by vibrations on the electronic excited states. In addition to the narrow feature at  $1670\text{ cm}^{-1}$  we have already described,

these absorption features are composed of two major bands, centered at  $\omega_3 \simeq 1590 \text{ cm}^{-1}$  and  $1640 \text{ cm}^{-1}$ , and arise from excitation anywhere in the visible absorption spectrum. The gap between these absorption features at  $\omega_3 = 1620 \text{ cm}^{-1}$  is caused by interference with a bleach feature that can be observed in the transient infrared absorption spectrum and appears in the  $t_2 < 0$  ps vibrational perturbed free induction decay. The intense, broad absorption feature is most likely related to the Chl C=O stretch modes on the electronic excited states. The  $\sim 100 \text{ cm}^{-1}$  width of this band is caused by the effect of the different protein environments experienced by each chlorophyll in the complex. It appears that the protein induced frequency shifts significantly broaden the electronic excited state features relative to the ground state bands. This is likely due to the greater polarizability and more diffuse character of electronic excited states, which would likely magnify the vibrational shifts due to nearby electrostatic interactions. The dynamics of different portions of this band, then, should provide specific information about the electronic populations of the different Chl moieties in the LHCII, and make it possible to track the flow of electronic excitation energy through the complex.[107]

### 6.2.2 Dynamics

The evolution of the LHCII 2DEV spectrum with respect to the waiting time  $t_2$  is illustrated in figure 6.3 (a-d). The time points that are easiest to understand are the early time spectrum shown in figure 6.3 (a), before most electronic energy transfer occurs, and the long time spectrum shown in figure 6.3 (d), at  $t_2 = 15$  ps. The latter, which is subsequent to the majority of the transient excitation transfer dynamics, shows a significant degree of symmetry between the two major electronic excitation bands. The structures in the spectra can be most readily interpreted in relation to theoretical simulations of the 2DEV spectra of an electronically coupled dimer.[107] The  $t_2 = 0$  ps spectrum is representative of the distribution of excited state population initially created by the visible excitation laser. For each excitation frequency  $\omega_1$ , the spectrum with respect to the detection frequency  $\omega_3$  is given by the vibrational spectrum of the sites which can be populated by a visible excitation at  $\omega_1$ . The weight in the spectrum of each individual site is provided by the participation of that site in the exciton states excited by that excitation energy. The loss of strong dependence on  $\omega_1$  at longer waiting times  $t_2$  indicates that the excitation energy in the complex has largely approached its equilibrium distribution with respect to the excited state manifold. It is believed to take  $\sim 50$  ps for excitation energy in LHCII to fully equilibrate.[124] The dependence of the spectral intensity on  $\omega_1$  depends primarily on the amount of population initially created with that energy, therefore this aspect of the structure is not expected to relax.[107] For LHCII at 77 K, when the electronic excited states have equilibrated, the majority of the population will be localized on the low energy trimer composed of the sites a610, a611 and a612.[124] This  $t_2 = 25$  ps spectrum, then, should be described reasonably well as the 2DEV spectrum of these three sites, with the ratio of each given by their relative population at equilibrium, independent of the excitation energy.

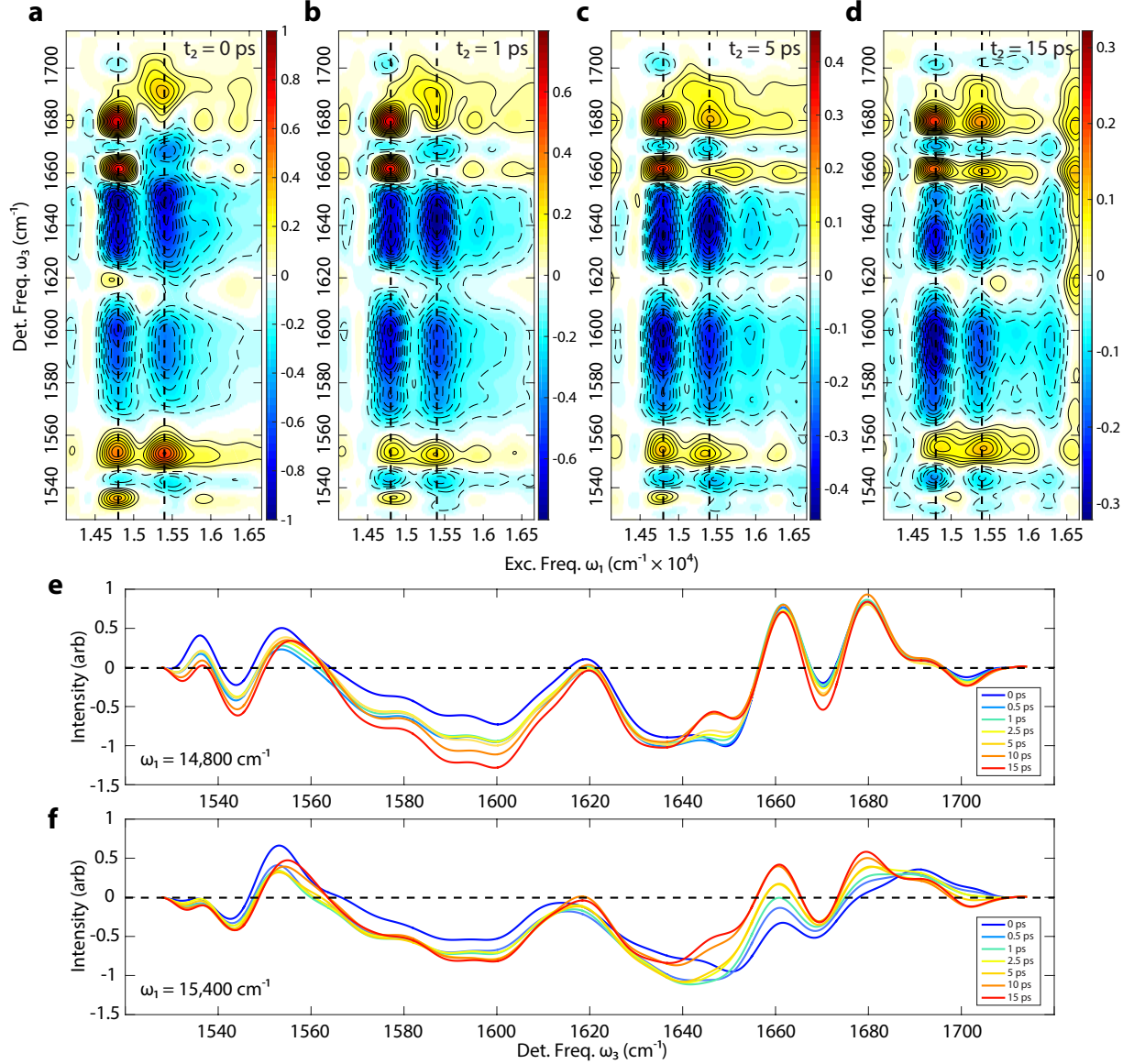


Figure 6.3: 2DEV spectra of LHCII at  $t_2 = 0$  ps (a),  $1$  ps (b),  $5$  ps (c) and  $15$  ps (d). Slices through these spectra at  $\omega_1 = 14800 \text{ cm}^{-1}$  and  $15400 \text{ cm}^{-1}$ , the positions marked by vertical dashed lines on (a-d), are shown in (e) and (f) normalized to their absolute maxima at  $t_2 = 0$ , where the dynamics have been normalized by the fit to the first right singular vector  $V_1$  to facilitate visualization of the excited state dynamics, with the overall relaxation removed.

Between the limiting cases of the initial excitation distribution observed in the  $t_2 = 0$  ps spectrum and the long time spectrum of the roughly equilibrium populations, 2DEV spectra at intermediate times contain the details of excited state energy transfer and relaxation. To facilitate the visualization of the effect of the excitation energy transfer between the various

chromophores in the complex, we plot slices through the two main electronic excitation bands at  $\omega_1 = 14800$  and  $15400 \text{ cm}^{-1}$  in figures 6.3 (e) and (f). Here, the dynamics have been normalized to the fit to the first right singular vector  $V_1(t)$ , which represents to overall relaxation of the spectrum, and will be discussed in greater detail in section 6.2.3.

The dynamics that are easiest to interpret are those of the bleach features related to Chl *b* at  $\omega_1 = 15400 \text{ cm}^{-1}$  and  $\omega_3 = 1690 \text{ cm}^{-1}$  which decays with increasing  $t_2$ . At the same time, the bleach associated with Chl *a* at  $\omega_1 = 15400 \text{ cm}^{-1}$  and  $\omega_3 = 1680$  and  $1660 \text{ cm}^{-1}$  grows in. These are clear, unambiguous indications of excited state population that was initially created in Chl *b* undergoing energy transfer to Chl *a*. The Chl *a* bleach features located at  $\omega_1 = 14800$  and  $15400 \text{ cm}^{-1}$  can be compared to separately track the population that originated on Chl *b* and other high energy excited states from that which originated on the lower energy Chl *a* states. Notably, there is a shoulder at  $\omega_3 = 1690 \text{ cm}^{-1}$  for all excitation frequencies that persists out to long time. This feature may be an indication of a long lived excited state population on Chl *b*, even when the lower energy electronic absorption band traditionally assigned as Chl *a* has been excited. According to the Novoderezhkin Hamiltonian for LHCII,[124] the lowest energy electronic eigenstate which contains at least 10% of its population on a Chl *b* lies  $310 \text{ cm}^{-1}$  above the overall lowest energy exciton. While this might be sufficient to explain the presence of this shoulder at  $\omega_1 = 14800 \text{ cm}^{-1}$  for early waiting times, it cannot explain its persistence with  $t_2$  – the thermal energy at 77 K is insufficient to populate this state subsequent to exciton relaxation. This observation of long-lived Chl *b* population, therefore, suggests that there may be a significant problem with the currently available Hamiltonians for LHCII, and that there are low energy states with significant Chl *b* character. Even if these observations are further substantiated, it seems unlikely that the overall connectivity of the current Hamiltonians is incorrect, as this is determined in large part by the crystal structure for LHCII. The models used to estimate the site energies and coupling strengths, however, will certainly have to be reevaluated.

In addition to the dynamics of these bleach features specifically associated with either Chl *a* or Chl *b*, the broad excited state absorption feature also of significant interest. They can be roughly separated into three regions, which display different kinetics: two narrower bands at  $\omega_3 \simeq 1650$  and  $1635 \text{ cm}^{-1}$ , and a broad region encompassing  $\sim 1560 - 1620 \text{ cm}^{-1}$  (centered near  $1590 \text{ cm}^{-1}$ ). The dynamics of these bands are somewhat different for the slices corresponding to excitation at  $\omega_1 = 14800$  or  $15400 \text{ cm}^{-1}$ , but they share some similar features. For both excitation regions the  $1650 \text{ cm}^{-1}$  band shows an overall decay, on the timescale of several ps. This is in sharp contrast with the neighboring band at  $1635 \text{ cm}^{-1}$ , which shows an initial increase in intensity on a sub ps timescale. For the lower energy excitation at  $\omega_1 = 14800 \text{ cm}^{-1}$ , this band then levels off and remains roughly constant for the remainder of the waiting time. For the higher energy excitation at  $\omega_1 = 15400 \text{ cm}^{-1}$ , however, following a similar initial rise, this vibrational band subsequently decays, after several ps. The  $1590$  band behaves differently, showing a monotonic increase in intensity for both excitation regions. Following an initial sub ps timescale shared between the two excitation bands, for the higher energy excitation this increase slows substantially, and the intensity remains roughly constant, whereas it continues to gain intensity for the lower energy

excitation region.

Together, the dynamics of these modes suggest a flow of excitation energy through the complex. Under this interpretation, the  $\omega_3 = 1650 \text{ cm}^{-1}$  band serves as a proxy for the population of some higher energy electronic excited states, which are most likely associated with Chl *b* moieties. As the excitation relaxes from these higher energy states, it flows through some transient intermediates, which contribute to the  $1660 \text{ cm}^{-1}$  band, and end up in the low energy states, manifesting in the broad  $1590 \text{ cm}^{-1}$  band. Because the dynamics are somewhat different for the higher and lower energy electronic bands, there must of course be a number of chromophores that contribute to each of these vibrational bands, and so the differing dynamics show that there are distinct energy transfer pathways from the regions of the protein in which lower energy Chl *a* states are located, separate from those regions containing the higher energy, predominantly Chl *b* states. Because of the similarities in the dynamics, however, there must also be common pathways through which a substantial amount of the excitation energy is transported.

### 6.2.3 Principal Component Analysis

The spectral structures and dynamics illustrated in figure 6.3 are quite complex. To perform a more quantitative analysis of these electronic excited states dynamics, the utilization of data reduction techniques, such as the singular value decomposition (SVD), becomes essential.[157, 80] In performing this decomposition, we consider the total spectrum  $S(\omega_1, t_2, \omega_3)$  as a mapping between a vector space composed of 2D spectral surfaces  $U_i(\omega_1, \omega_3)$  and their associated dynamics  $V_i(t_2)$  and linearly weighted by the singular values  $\Sigma_i$ , so that the spectrum can be written as a matrix product  $\mathbf{S} = \mathbf{U} \cdot \mathbf{\Sigma} \cdot \mathbf{V}^\dagger$ . This decomposition provides a set of basis spectra which, taken together with the singular values  $\Sigma_i$ , describe the overall 2DEV spectrum. The most straight-forward way to understand the SVD components is that the first component is the single spectrum and dynamics which best describe the total data. If this component is subtracted off, then the second component is the best spectrum and dynamics to describe the remainder, and so-forth. Upon performing the SVD, we find that there are four components which are not dominated by noise. These components are shown in figure 6.4, with the left singular vectors  $U_i$  (the spectral component) shown in panels (A-D) and the corresponding right singular vectors  $V_i$  (the dynamics component) shown in panel (E). To describe the kinetics of the right singular vectors, we have performed fits to biexponential decays of the form  $V_i(t_2) = A_1 \exp(-t_2/\tau_1) + A_2 \exp(-t_2/\tau_2) + A_3$  for the data from  $t_2 = 0 \text{ ps}$  onwards. The results of these fits, together with the singular values for the significant components, are provided in table 6.1.

The first spectral component  $U_1$  shows very similar structures to the spectrum at  $t_2 = 1 \text{ ps}$ , as seen in figure 6.3 (b). This is indicative of the fact that the overall changes to the spectrum with respect to  $t_2$  are relatively minor, with the major features remaining essentially unchanged. The dynamics in the first right singular vector  $V_1$  reflect the overall decay of the spectrum as the excited state population returns to the ground state. The kinetics are

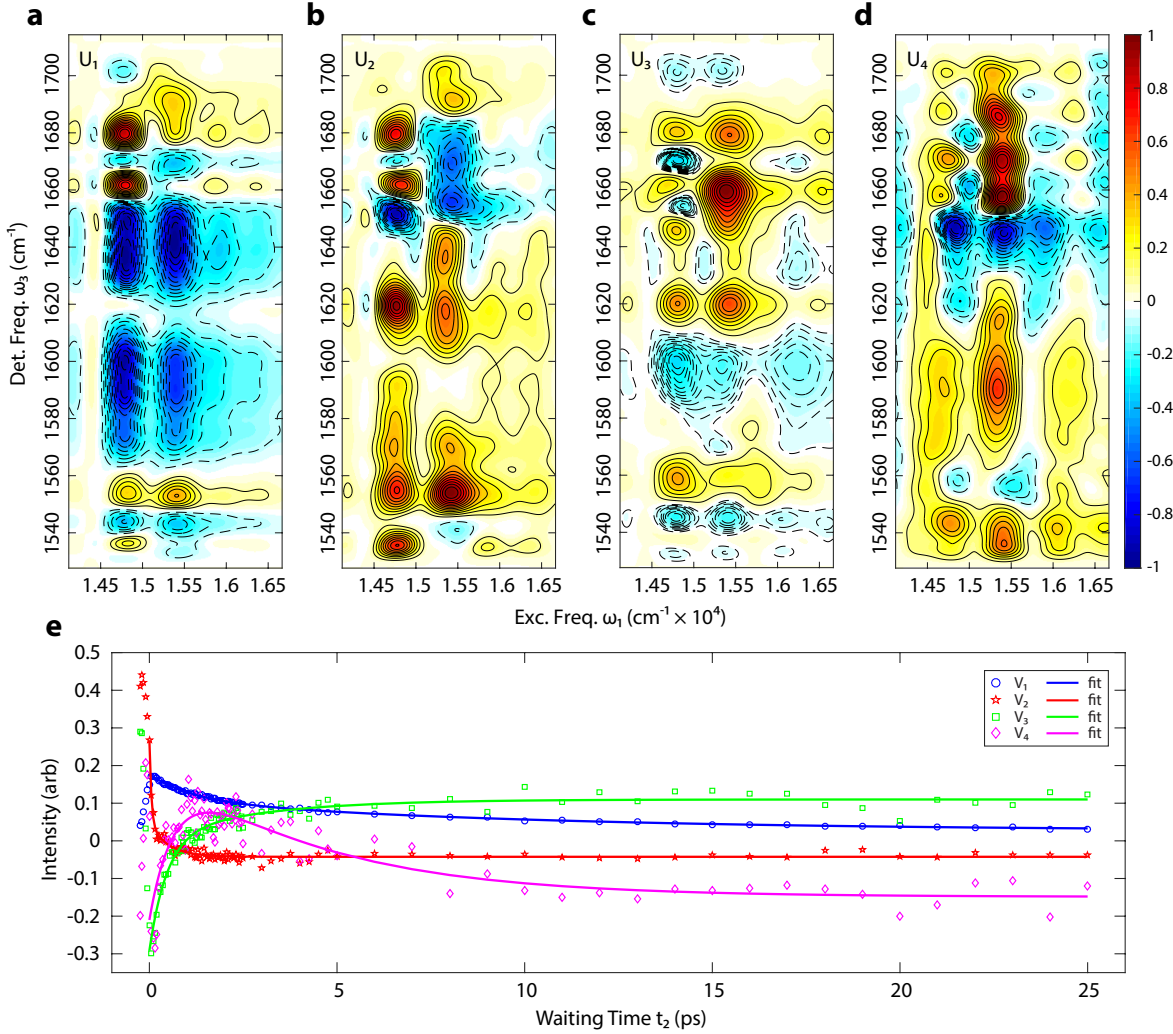


Figure 6.4: Singular value decomposition of the LHCII 2DEV spectrum. The first four left singular vectors (spectral component) are shown in (a-d), normalized to their individual absolute maxima. The corresponding right singular vectors (dynamics component) are shown in (e), with fits to biexponential decays from  $t_2 = 0$  onwards. The fit parameters are given in table 6.1.

described by two components with similar amplitudes, time constants of  $\tau_1 = 1.13$  ps and  $\tau_2 = 9.97$  ps, with the slower nanosecond scale relaxation captured by the constant offset.

The other three significant components can be most easily understood as describing the evolution of the spectrum with respect to the overall relaxation captured by  $U_1(\omega_1, \omega_3)$  and  $V_1(t_2)$ . The spectral components  $U_2$ ,  $U_3$  and  $U_4$  are rather complicated, but there are several features for which we have made the assignments, which aids in the interpretation of the associated dynamics.  $U_2$  is the only SVD component other than  $U_1$  which shows



Table 6.1: Fits to the significant right singular vectors following the biexponential form  $A_1 \exp(-t/\tau_1) + A_2 \exp(-t/\tau_2) + A_3$ 

	$V_i(t) = A_1 \exp(-t/\tau_1) + A_2 \exp(-t/\tau_2) + A_3$				
Singular Value $\Sigma_i$	$A_1$	$\tau_1$ (ps)	$A_2$	$\tau_2$ (ps)	$A_3$
29.25	0.07	1.13	0.08	9.97	0.03
4.46	0.22	0.05	0.09	0.50	-0.04
2.92	-0.30	0.46	-0.10	2.90	0.11
1.42	-0.45	0.67	0.39	4.21	-0.15

a significant peak at the position of the Chl *b* ground state C=O stretch at  $\omega_1 = 15400 \text{ cm}^{-1}$  and  $\omega_3 = 1690 \text{ cm}^{-1}$ . This indicates that a significant process represented by this component is the relaxation from Chl *b* to Chl *a*. The dynamics in  $V_2$  show a very fast 50 fs fit component, commensurate with the time resolution of the experiment, and a 0.5 ps fit component. The latter timescale is consistent with the typical timescale reported for the Chl *b* to Chl *a* energy transfer, which was first measured by fluorescence upconversion to occur with a time constant of 0.68 ps,[48] and has been measured more recently using transient absorption and 2DES to occur with two timescales of  $\sim 100 - 200 \text{ fs}$  and  $\lesssim 1 \text{ ps}$ . [149, 124, 46] The current experiment, however, has an advantage over these previous measurements, as it does not require any assumption that the excitation at the  $15400 \text{ cm}^{-1}$  band populates only Chl *b* states, or that there is no strong mixing between the Chl *a* and Chl *b* states – we can monitor vibrational bands which we know uniquely and unambiguously distinguishes population of Chl *b* and Chl *a*.

In addition to the readily assignable features associated with Chl *b*, the second, third and fourth SVD components show dynamics in the excited state absorption bands which can be related to our earlier qualitative discussion of the dynamics.  $U_2$ , which is associated with a very fast, sub ps decay, has a negative feature at  $\omega_1 = 15400 \text{ cm}^{-1}$  and  $\omega_3 = 1650 \text{ cm}^{-1}$ , as well as a positive feature at  $\omega_3 = 1640 \text{ cm}^{-1}$ . Together, these suggest a simultaneous decay of one excited state band, and rise of a separate band, showing the energy transfer between one set of Chls and another. Following the Novoderezhkin Hamiltonian, this could be a signature of either the stromal side relaxation from the b601'-b608-b609 cluster to the a602-a603 cluster and the a610-a611-a612 low energy trimer, or of the luminal side relaxation from the b606-b607 dimer to the a604-b605 dimer. The third SVD component shows a rise component with a timescale of 0.46 and 4.21 ps, and is associated with a negative spectral feature at  $\omega_3 = 1600 \text{ cm}^{-1}$ , which seems then to describe the long time rise of the excited state band in this region of the spectrum. Presumably, this band should be related to the low energy trimer a610-a611-a612 which contribute to the lowest energy electronic states, and perhaps the bottleneck sites a604, a613-a614 and a602-a603. The fourth SVD component shows a fast 0.45 ps rise followed by a 4.21 ps decay, and is associated with a negative band at  $\omega_3 = 1645 \text{ cm}^{-1}$ . This feature must be related to some short lived intermediates,



such as b605, which might act as an important intermediate in the Chl *b* to Chl *a* energy transfer. This seems reasonable, as it is also associated with a positive band near the Chl *b*  $1690\text{ cm}^{-1}$  ground state feature, but has its intensity peaked instead at  $\omega_3 = 1685\text{ cm}^{-1}$  and therefore may be a shifted Chl *b* bleach band. The Novoderezhkin Hamiltonian[124] predicts the population on b605 to decay to a604 on a 3.6 ps timescale, which is in good agreement with our observed kinetics. The details of these spectral components suggest that if it is possible to accurately assign the specific vibrational shifts of each Chl molecule in the LHCII complex, these data will reveal specific energy transfer pathways which would be very difficult to resolve with conventional time resolved electronic spectroscopies.

### 6.3 Conclusion

In this work we have presented and discussed the structures and dynamics observed in 2DEV spectra of the photosynthetic light harvesting complex LHCII. The major features of the spectrum are assigned by comparison to the 2DEV spectra of isolated Chl *a* and Chl *b*. However, there are some significant differences, the details of which are difficult to precisely assign. The substantial advantage of this method over traditional electronic spectroscopic techniques comes from the unambiguity with which it can be possible for molecular vibrational bands to be assigned to specific molecular species, as opposed to the broad, relatively structureless electronic transitions. The major difficulty for this system is in making the assignments in a large and complex system. An analysis of the vibrational shift induced by the protein, due to effects such as specific conformational distortions, hydrogen bonding, coordination state and shifts induced by the electrostatic fields of the protein environment will provide greater insight into the detailed assignments of the observed vibrational bands. Advances in quantum chemistry methods which would allow for the exploration of excited state potential surfaces of large and complex systems like LHCII would be of great value towards complete understanding of the photophysics of photosynthetic light harvesting.

We use the dynamics of the spectrum, coupled with a SVD spectral analysis, to demonstrate how 2DEV can be used to follow the flow of excitation energy through the complex. The distinct vibrational bands of the Chl *a* and Chl *b* allow us to directly track the energy transfer between these different species, with no ambiguities due to imprecise electronic Hamiltonians or broad electronic linewidths. For these vibrational bands which we can definitively assign to a specific molecular species, we can track the motion of the electronic excitation energy through the complex without relying on modeling and spectral fitting. For example, the spectral decomposition reveals signatures of a short lived ( $\sim 5\text{ ps}$ ) Chl *b* intermediate, which is most likely associated with the b605 site. The long lived shoulder at  $\omega_3 = 1690\text{ cm}^{-1}$  band provides evidence that we might even observe a completely unexpected Chl *b* population that survives for longer than 25 ps, which is not predicted by the currently available Hamiltonians. If this interpretation is correct, this would bring into question the quality of these Hamiltonians, and would suggest that the details of the exciton transfer dynamics through LHCII need to be substantially reconsidered.

The 2DEV experiments furthermore allow us to observe dynamics in the electronic excited state bands which provide more detailed information about the flow of excitation energy through the complex. We observe distinct bands which report on the different phases of the early relaxation of the excitation energy through the complex. Current computational techniques make it very difficult to provide these excited state vibrational bands with definitive assignments, due in large part to the importance of the environmentally induced shifts, and the cost of excited state quantum chemistry methods. If it becomes possible to determine precise assignments of the vibrational band on the electronic excited state for the different sites in the complex, then these experiments will provide us with unparalleled resolution of the early time flow of electronic excitation energy through the LHCII complex.

## 6.4 Experimental Methods

The waiting time  $t_2$  between the visible pump pair and the IR probe was controlled with a motorized delay stage. The relative polarization of the pump and probe lasers was set to either parallel (giving rise to the signal  $S_{\parallel}$ ), or perpendicular ( $S_{\perp}$ ), and the isotropic responses were calculated at  $S_{iso} = S_{\parallel} + 2S_{\perp}$ . The desired 2DEV signal was isolated by phase cycling the pump pulse pair in a  $4 \times 1$  scheme,[122, 181] and a Fourier transform was performed along  $t_1$  to produce the final electronic excitation frequency  $\omega_1$  vs. vibrational detection frequency  $\omega_3$  correlation spectra, parametrized by the waiting time  $t_2$ .

The LHCII sample was isolated from spinach, and dispersed in a buffer of 50 mM Tris-HCl (pH 7.8), 0.12 M NaCl, 0.3 M sucrose, and 0.03% *n*-dodecyl  $\beta$ -D-maltoside in D<sub>2</sub>O. This solution was mixed with glycerol-d<sub>8</sub> in a 70:30 (vol/vol) glycerol:LHCII ratio. The sample cell was constructed from two CaF<sub>2</sub> plates with a kapton spacer, and had a path-length of 100  $\mu$ m, and was placed in an optical cryostat (OptistatDN2, Oxford Instruments) at 77 K. The maximum optical density in the visible, shown in figure 6.1, was 0.8, and was  $\sim 0.4$  in the solvent subtracted infrared absorption (dominated by the protein amide bands). The Chl *a* and Chl *b* samples were dissolved in ethanol-d<sub>6</sub>, held at 77 K in the same type of sample cell. These samples had optical density of 2 at the absorption maximum in the visible, and of  $\sim 0.1$  in the solvent-subtracted infrared absorption.

## Chapter 7

# Future Directions for Two-Dimensional Electronic-Vibrational Spectroscopy

### 7.1 Introduction

Thus far in our efforts to formally describe the spectroscopy of 2DEV, we have made a series of simplifying approximations. Among these is the simplification of considering the elementary unit as effectively a four-level system, where we assume the electronic laser pulse excites the 0-0 transition and neglect the direct effect of other molecular vibrations which we are not directly probing. This is a good place to start in the analysis, as it results in some substantial simplifications, but it is important to then add the missing pieces back in and understand how more complicated effects might contribute to the spectrum, and how interesting and new information could be extracted with this technique. In this chapter I will describe several of the directions that seem most promising to develop.

### 7.2 Wavepacket Dynamics and Conical Intersections

The obvious first expansion of the model for the monomer is the inclusion of additional vibrational levels, either by growing the ladder for the mode being probed, or by adding in the important spectator vibrations. By expanding the system in this way, it becomes necessary to understand how anharmonicity and anharmonic coupling between modes can contribute to the spectra, and perhaps how these parameters could be measured on the electronic excited state. It also becomes natural to consider how coherent wavepackets might appear in the 2DEV spectrum, and how it might be possible to use this technique to gain new insight into the structural deformations that occur in a molecule upon excitation, or perhaps even as it passes through a conical intersection. This line of inquiry in particular seems to be of potential interest, as 2DEV could potentially provide a method for following these excited

state dynamics in a structurally sensitive way. The proliferation of femtosecond stimulated Raman spectroscopy (FSRS) for studying this type of problem[98, 84] indicates that there is substantial interest in this field. Because 2DEV provides similar information to FSRS, but in a more direct and potentially more detailed way, it seems that it could be a valuable tool for studying these processes.

To begin to understand how these types of excited state vibrational dynamics might appear in a 2DEV spectrum, we have performed several preliminary model calculations to gain an understanding of how different effects might contribute to the spectrum. The models are based on a simplified version of the model developed by Dong *et al.*[43] and discussed in detail in chapter 3, with the necessary additions include the additional vibronic structure.

The more straight forward case is where a FC active mode is directly probed. In this case we simply expand the system Hamiltonian to allow for a ladder of states in the discrete vibration, which introduces the necessity for two additional parameters in the model, the equilibrium displacement  $d_v$  of the mode being probed between the ground and excited electronic states, and the anharmonicity  $\Delta_v$ , which will generally be small, and we will assume to be the same for the ground and excited state manifolds, as this will not dramatically change the picture. The total Hamiltonian can then be written as

$$H = H_g^{sys} |g\rangle \langle g| + H_e^{sys} |e\rangle \langle e| + H^{bath} + H^{sys-bath} \quad (7.1)$$

where these terms are given by

$$H_g^{sys} = (\omega_v^g - \Delta_v a_v^\dagger a_v) a_v^\dagger a_v \quad (7.2)$$

$$H_e^{sys} = (\omega_v^e - \Delta_v a_v^\dagger a_v) a_v^\dagger a_v + \varepsilon_{eg} + (\omega_v^e - \Delta_v a_v^\dagger a_v) d_v (a_v^\dagger + a_v) \quad (7.3)$$

$$H^{bath} = \sum_i \nu_i^e b_i^{e\dagger} b_i^e + \sum_j \nu_j^v b_j^{v\dagger} b_j^v \quad (7.4)$$

$$H^{sys-bath} = \sum_i \nu_i d_i (b_i^{e\dagger} + b_i^e) |e\rangle \langle e| + \sum_j \nu_j^v h_j (b_j^{v\dagger} + b_j^v) a_v^\dagger a_v \quad (7.5)$$

where we have assumed a fully uncorrelated model for the harmonic baths to which the electronic and vibrational degrees of freedom couple, represented by  $H^{bath}$ , and the system bath couplings are taken as linear in both the system and the bath. The electronic energy gap is given by  $\varepsilon_{eg}$  and the coupling between the electronic excitation and the vibrational degree of freedom comes in the form of the change of the vibrational frequency from  $\omega_v^g$  to  $\omega_v^e$  and the displacement of the equilibrium coordinate by  $d_v$ .

The response functions can be derived for this Hamiltonian, which can be simplified using a short-time approximation to allow it to be calculated directly in the frequency domain. The pathways corresponding to each of the possible vibronic transitions will be weighted by the FC factor, which depends on both the change in frequency and the displacement, as well as by the relevant vibrational transition dipole moment. If we consider only small values for the anharmonicity  $\Delta_v$ , then we can approximate both of these quantities from

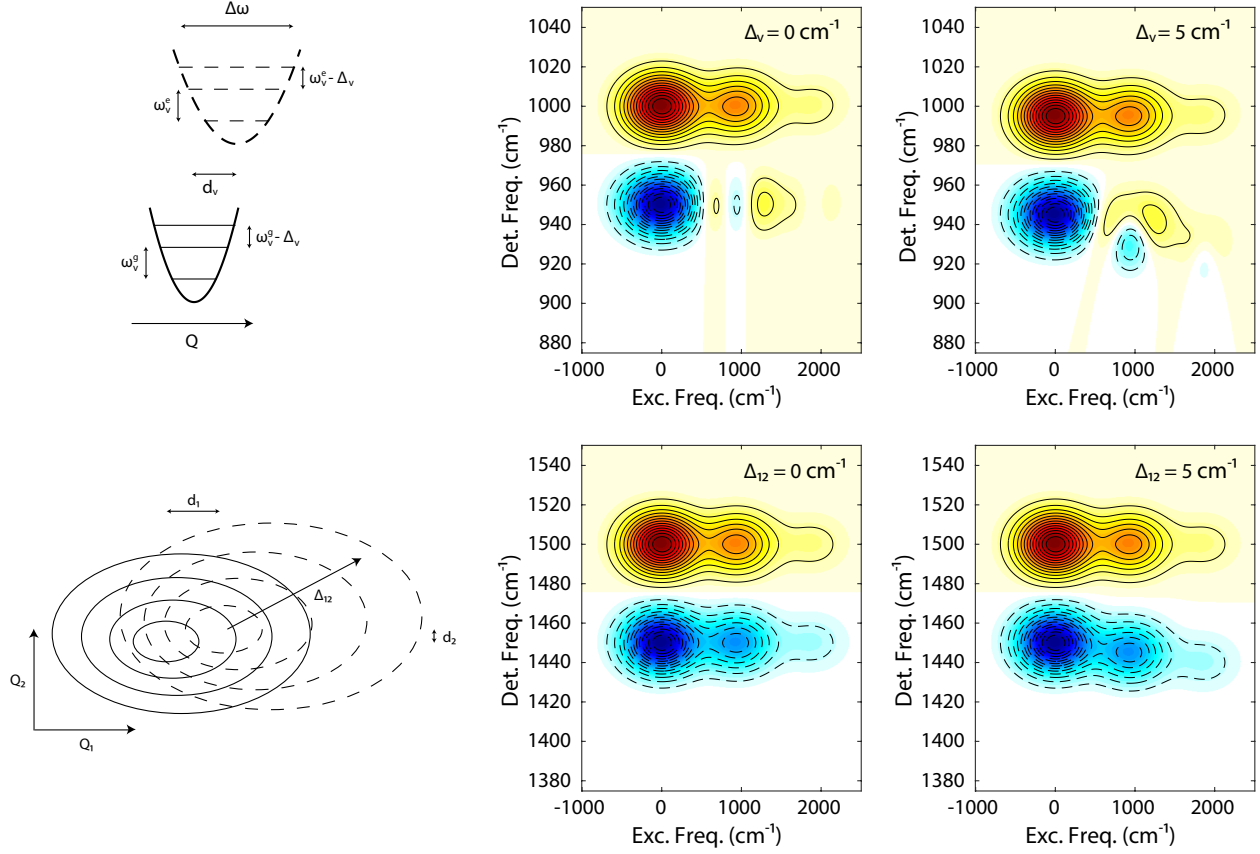


Figure 7.1: 2DEV spectra calculated for  $t_2 = 0$  ps for two different situations of vibronic excitation. The lineshape functions were calculated using a short time approximation. The top row shows the case where the mode being probed is itself Franck-Condon (FC) active, for the fully harmonic case and the case with small anharmonicity  $\Delta_v$ . The bottom row shows the case where the mode being probed is anharmonically coupled to a lower frequency FC active mode, for two different values of the anharmonic coupling  $\Delta_{12}$ . For both cases the FC active mode has a frequency of  $1000 \text{ cm}^{-1}$  on the ground electronic state,  $950 \text{ cm}^{-1}$  on the excited electronic state and a Huang-Rhys factor of 0.45. The FC inactive mode being probed in the spectra in the bottom row has a frequency of  $1500 \text{ cm}^{-1}$  on the electronic ground state and  $1450 \text{ cm}^{-1}$  on the excited electronic state. The excitation axes are referenced to the energy of the zero-phonon transition and the laser pulses are taken to be delta functions.

the formulas for harmonic oscillators. The FC factors for this situation have been derived previously,[9] and the transition dipole moment will scale as  $\mu_{n \rightarrow n+1} = \sqrt{n+1}\mu_{0 \rightarrow 1}$  and  $\mu_{n \rightarrow n-1} = \sqrt{n}\mu_{0 \rightarrow 1}$  for starting on the  $n$ th vibrational level. The 2DEV spectrum at  $t_2 = 0$  ps can then be computed by summing over the possible vibronic transitions, taken with the appropriate weights.

An example is shown in the top row of figure 7.1 for the harmonic case  $\Delta_v = 0 \text{ cm}^{-1}$  and

a slightly anharmonic case  $\Delta_v = 5 \text{ cm}^{-1}$ . The vibrational frequencies are given by  $\omega_v^g = 1000 \text{ cm}^{-1}$  and  $\omega_v^e = 950 \text{ cm}^{-1}$ , and the displacement is such that the Huang-Rhys factor  $S = 0.45$ , noting that this depends on the displacement  $d_v$ , the ground state vibrational frequency  $\omega_v^g$  and the vibrational effective mass  $M_v$  as  $S = \frac{1}{2}M_v\omega_v^g d_v^2$ . The band that arises from the ground electronic state appears at the detection frequency equal to  $\omega_v^g$ , with no meaningful contribution from the anharmonicity. The lineshape with respect to the excitation axis is essentially the same as the electronic linear absorption lineshape. For the excited electronic state bands, there is a greater complexity that arises from the possibility of exciting higher vibrational levels, and the presence then of both an induced vibrational absorption and a vibrational stimulated emission, which will occur with opposite sign and can interfere. The detection frequency at which these bands will occur will depend on the vibrational level  $n$  that was excited with the electronic transition, with the negative induced absorption bands appearing at the  $\omega_v^e - n^2\Delta_v$  for this model, while the positive stimulated emission bands will appear at  $\omega_v^e - (n-1)^2\Delta_v$ . This, together with the differences in the lineshapes for these different pathways, are the reason for the rather complicated interference patterns observed in the simulated spectra. As  $t_2$  is allowed to evolve, the excited state band should be indicative of the nuclear evolution on the electronic excited state, decaying eventually to be a near copy of the ground state band with opposite sign and centered at  $\omega_v^e$ , after the vibrational excitation has fully relaxed. It is not simple to incorporate the population dynamics during  $t_2$  in an accurate way, and this would be potentially a very interesting way to study excited state wavepackets. Inclusion of accurate vibrational dephasing and relaxation may be possible with the adaptation of a model developed for the ground electronic state by Ishizaki and Tanimura.[93]

We performed a similar scale of simulation for a simple model where the vibration being probed is not itself significantly FC active, but is anharmonically coupled to a separate low frequency mode that does have a significant displacement. The system parts of the Hamiltonian for this model can be written as

$$H_g^{sys} = \omega_1 a_1^\dagger a_1 + \left( \omega_2^g - \Delta_{12} \sum_n \left( a_1^\dagger a_1 \right) \right) a_2^\dagger a_2 \quad (7.6)$$

$$H_e^{sys} = \omega_1 a_1^\dagger a_1 + \left( \omega_2^e - \Delta_{12} \sum_n \left( a_1^\dagger a_1 \right) \right) a_2^\dagger a_2 + \varepsilon_{eg} + \omega_1 d_1 \left( a_1^\dagger + a_1 \right) \quad (7.7)$$

where we are considering mode 2 as the mode being probed, while mode 1 is the lower frequency FC active mode. A schematic of this model is shown in the bottom left of figure 7.1, and for simplicity we are assuming that  $d_2 = 0$ , the strength of the anharmonic coupling between the vibrational modes  $\Delta_{12}$  is the same for the ground and excited electronic states, and the modes are otherwise harmonic. The bath is considered in the same way as with the previous model, with each system degree of freedom assumed to be coupled to its own independent set of harmonic oscillators.

The 2DEV spectra for this model can be calculated in the same manner as the previous model, with some examples shown in the bottom row of figure 7.1. Again we have performed

a short time approximation and can only consider  $t_2 = 0$  ps. Two different values of the anharmonic coupling are shown here,  $\Delta_{12} = 0$  and  $5 \text{ cm}^{-1}$ . The major difference from the previous model comes from the absence of the stimulated emission pathways on the electronic excited state, as the vibronic progression in this case does not originate from the mode being probed. The effect of the anharmonic coupling is to cause a slanting down of the overall lineshape, stepping by  $\Delta_{12}$  for each quantum of the FC active mode that has been excited. Again the precise dynamics for this model will require a more sophisticated method to be calculated, but it is possible to take a different approach to the same type of scenario that can give us a good sense of the dynamics that could be observed.

Instead of considering the low frequency FC active mode directly as a system degree of freedom, we can instead include it in the manner traditional for the multimode Brownian oscillator approach to calculate electronic spectroscopies, by including it as a narrow peak in the spectral density, corresponding to an underdamped oscillator.[120] If we were to attempt to use this approach while additionally following the assumption of independent baths for the electronic and vibrational degrees of freedom, then the only effect of the underdamped mode would be to modulate the electronic absorption lineshape, in the manner discussed by Dong *et al.*[43] To allow the high frequency vibration to also be effected by the wavepacket oscillation, then, we instead consider a fully correlated bath, and the Hamiltonian can be simplified to a four level system

$$H_g^{sys} = \omega_v^g a_v^\dagger a_v \quad (7.8)$$

$$H_e^{sys} = \varepsilon_{eg} + \omega_v^e a_v^\dagger a_v \quad (7.9)$$

$$H^{bath} = \sum_i \nu_i b_i^\dagger b_i \quad (7.10)$$

$$H^{sys-bath} = \sum_i \nu_i (d_i |e\rangle \langle e| + h_i a_v^\dagger a_v) (b_i^\dagger + b_i) \quad (7.11)$$

where we only include a single set of harmonic oscillators, with frequencies  $\nu_i$ , as the bath. The system bath coupling for the electronic transition is given by the displacements  $d_i$ , while for the vibration it is given by the linear coupling parameters  $h_i$ .

The spectral densities for the transitions are determined by these coupling parameters as  $\mathcal{J}_e(\omega) = \sum_i d_i^2 \nu_i^2 \delta(\omega - \nu_i)$  and  $\mathcal{J}_v(\omega) = \sum_i h_i^2 \nu_i^2 \delta(\omega - \nu_i)$ . Because we now have only a single set of bath oscillators, there is also a correlation term to the overall spectral density to which both system degrees of freedom couple, given by the cross term  $\mathcal{J}_c(\omega) = \gamma_c \sum_i d_i h_i \nu_i^2 \delta(\omega - \nu_i)$ , where  $0 \leq \gamma_c \leq 1$  is an *ad hoc* correlation parameter that can be included to scale the strength of the correlation between the bath induced fluctuations. We will only consider  $\gamma_c = 1$  as the effect of varying it should be very predictable. The possibility for negative correlation is inherently included in  $\mathcal{J}_c$ , as there is no requirement for  $d_i \geq 0$  or  $h_i \geq 0$ . Therefore, if for any given bath mode  $i$ , if  $d_i$  and  $h_i$  carry the same sign, then the fluctuations induced by this bath mode will be correlated, whereas if they carry opposite sign they will be anti correlated. It is most typical that the excited electronic transitions will have positive displacements, so usually we should have  $d_i \geq 0$ . On the other hand, anharmonic coupling will generally

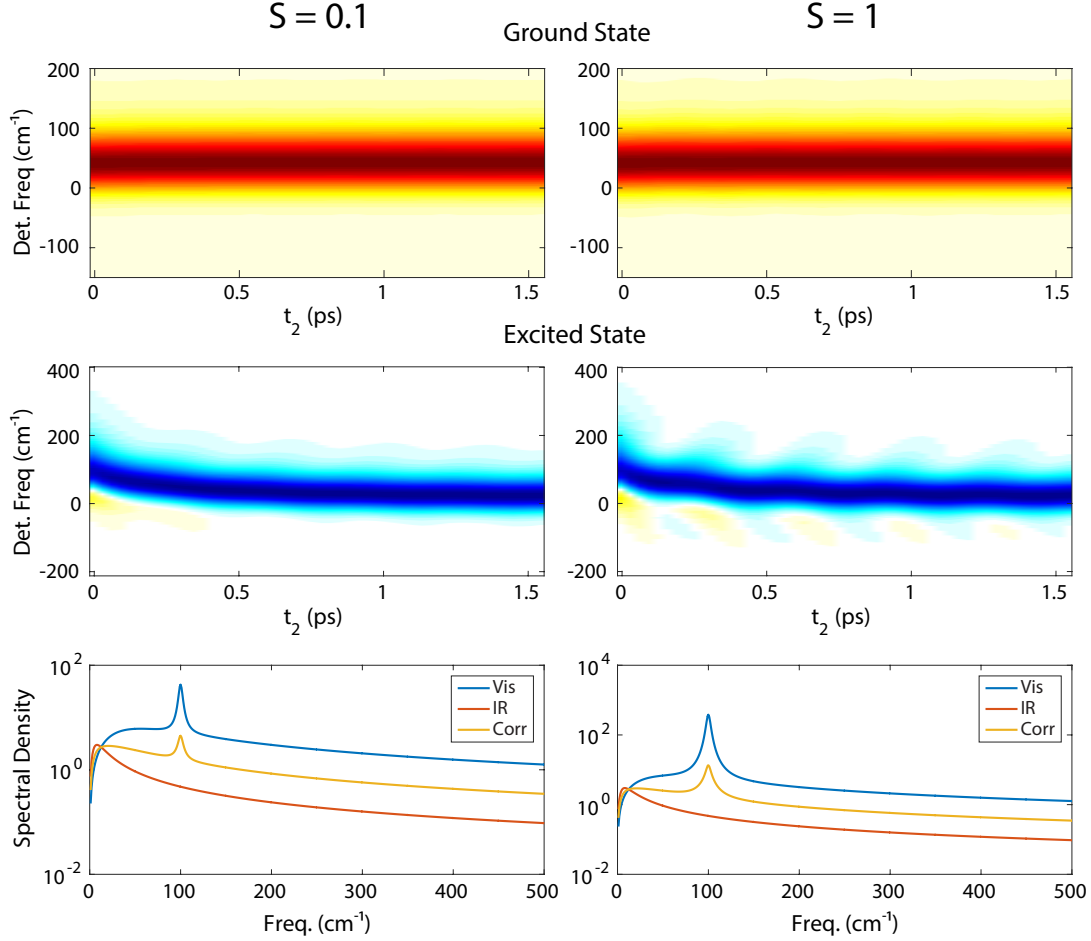


Figure 7.2: Transient IR absorption for the high frequency vibration on the electronic ground state (top), the electronic excited state (middle) and spectral densities (bottom) for the correlated bath model with two different values for the Huang-Rhys factor  $S$  for the underdamped bath mode. The signatures of the wavepacket dynamics only show up in the TA for the excited state band. The detection (probe) frequency is referenced to that of the high frequency vibration on the ground electronic state prior to renormalization by the bath.

decrease the vibrational transition frequency for higher levels, so it is probably more typical to have  $h_i \leq 0$ . This means that it would generally be expected to have anticorrelated fluctuations, though of course all other sign combinations will also occur, and it could be that certain bath modes induce correlated fluctuations while others induce anticorrelated fluctuations.

In practice we generally specify the spectral density by choosing some model form, such



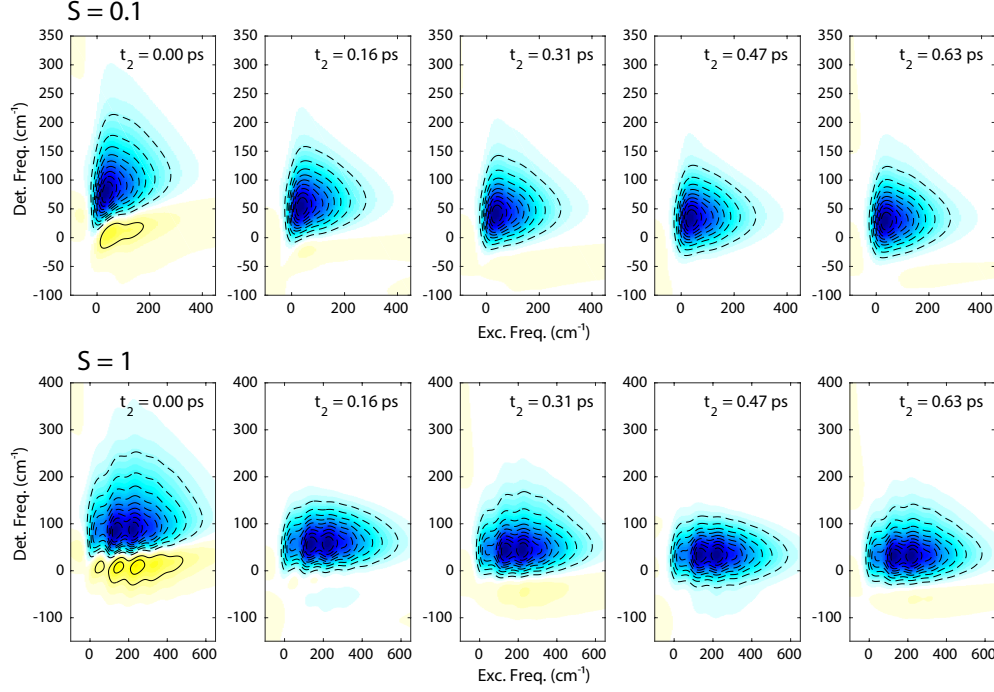


Figure 7.3: 2DEV spectra of the vibration on the electronic excited state for a series of waiting times roughly every half period for the underdamped mode for the correlated bath model with the same parameters as in figure 7.2. The excitation axis is referenced to the frequency of the zero-phonon transition and the detection axis is referenced to the frequency of the high frequency vibration on the ground electronic state, each prior to the renormalization by the bath.

as the general Brownian oscillator model, which is given by

$$\mathcal{J}_{BO}(\omega) = \frac{2S_j\omega_j}{\pi} \frac{\omega_j^2\gamma_j\omega}{(\omega_j^2 - \omega^2) + \omega^2\gamma_j^2} \quad (7.12)$$

where  $S_j$  is the Huang-Rhys factor,  $\omega_j$  is the natural frequency for the Brownian oscillator and  $\gamma_j$  is the damping of the oscillation. In the overdamped limit where  $\gamma_j \gg 2\omega_j$  this can be simplified to the Drude-Lorentz form

$$\mathcal{J}_{DL}(\omega) = \frac{2\lambda}{\pi} \frac{\gamma_j\omega}{1 + \gamma_j^2\omega^2} \quad (7.13)$$

where  $\lambda$  is the reorganization energy and  $\gamma$  is the timescale of the bath response. For the preliminary simulations here we will consider the high frequency vibration's spectral density as a Drude-Lorentz with  $\lambda_v = 50 \text{ cm}^{-1}$  and  $\gamma_v = 0.67 \text{ ps}$ . The electronic transition's spectral density will be given by the sum of a Drude-Lorentz with  $\lambda_e = 100 \text{ cm}^{-1}$  and  $\gamma_e = 0.1 \text{ ps}$  and an underdamped Brownian oscillator bath mode with frequency  $\omega_j = 100 \text{ cm}^{-1}$ , damping

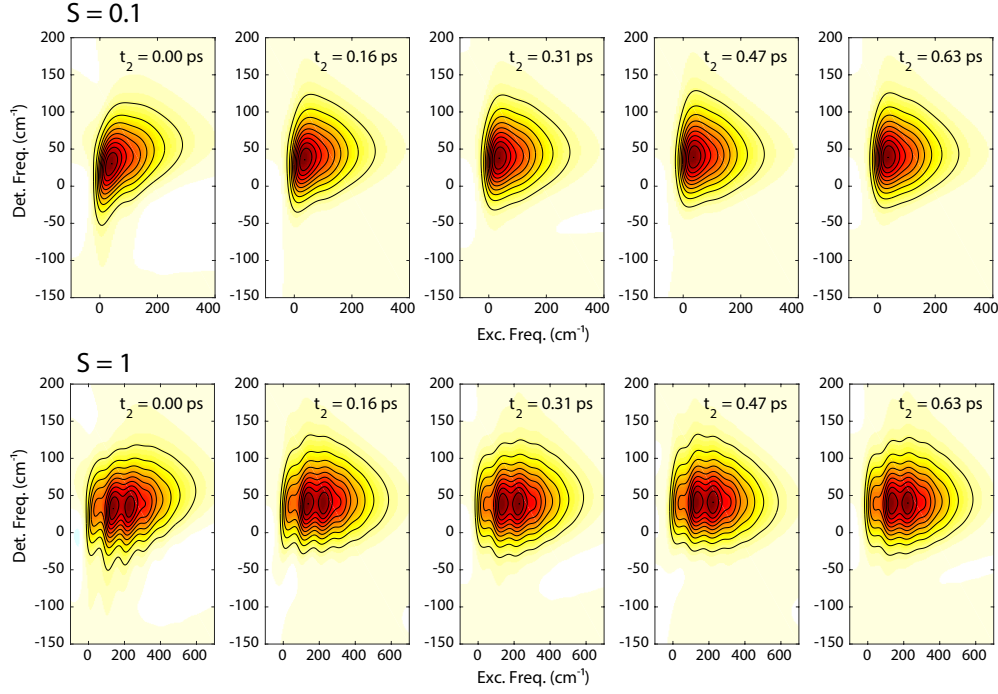


Figure 7.4: 2DEV spectra of the vibration on the electronic ground state for a series of waiting times roughly every half period for the underdamped mode for the correlated bath model with the same parameters as in figure 7.2. The excitation axis is referenced to the frequency of the zero-phonon transition and the detection axis is referenced to the frequency of the high frequency vibration on the ground electronic state, each prior to the renormalization by the bath.

$\gamma_j = 1$  ps and a variable Huang-Rhys factor. Several different calculations based on this model are shown in figures 7.2, 7.3 and 7.4.

The transient IR absorption calculated using this model are shown in figure 7.2, together with the relevant spectral densities. The spectral density for the correlated part of the fluctuations is taken to be  $\mathcal{J}_{corr}(\omega) = \pm \gamma_c \sqrt{\mathcal{J}_e(\omega) \mathcal{J}_v(\omega)}$ . By doing this, we are assuming that the relative signs for the system bath coupling parameters  $d_i$  and  $h_i$  are independent of the bath mode. This is not necessary, but it simplifies the treatment. If the relative sign does depend on the mode, this would introduce nodes into  $\mathcal{J}_{corr}$ . We additionally take the correlation factor  $\gamma_c = 1$ , and assume positive correlation. The change of this sign should have predictable results, reversing the signs for all of the spectral behaviors induced by this correlation. The effect of the correlation appears in the transient absorption in the primarily the dynamical change in the frequency of the vibration for the excited state band, which arises in precisely the same manner as the time dependent Stokes shift in electronic spectroscopies. This does not contribute at all to the band for the vibration on the electronic ground state. For the smaller value of  $S = 0.1$  this primarily comes in the form

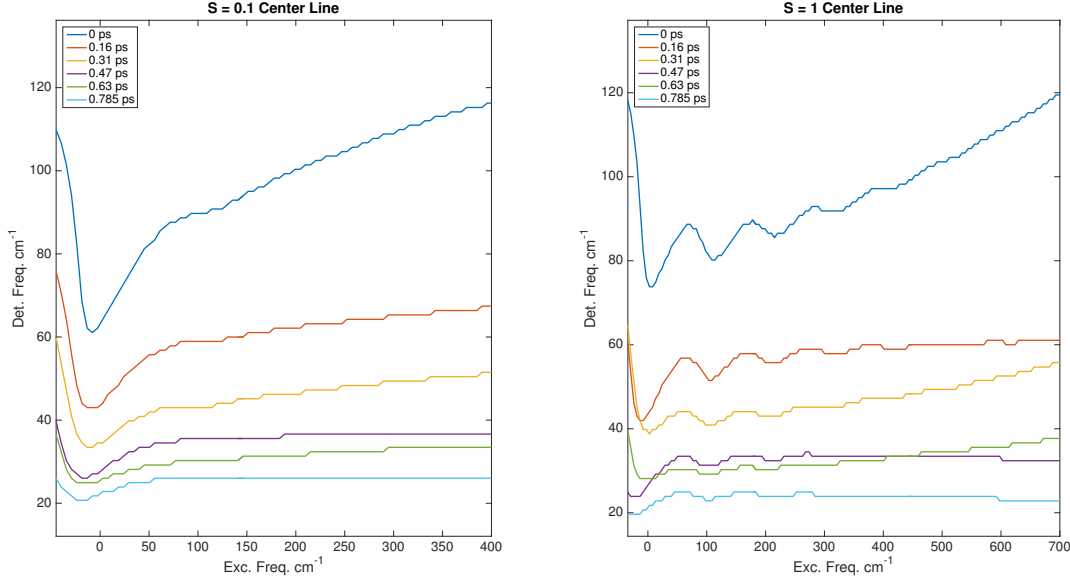


Figure 7.5: Center lines with respect to the excitation energy of the excited state band for a series of waiting times  $t_2$  for the excited state band of the correlated bath model with the same parameters as in figure 7.2. The excitation axis is referenced to the frequency of the zero-phonon transition and the detection axis is referenced to the frequency of the high frequency vibration on the ground electronic state, each prior to the renormalization by the bath.

of an overdamped relaxation with a small oscillation induced by the underdamped mode. For the  $S = 1$  case the underdamped oscillation is significantly increased in magnitude and becomes more clear. These dynamics in the vibrational frequency along the detection axis will not appear in the bands on the ground electronic state.

Several early  $t_2$  2DEV spectra of the excited state band with these parameters are shown in figure 7.3, while the 2DEV spectra for the ground state band are shown in figure 7.4. For the excited state band the dynamics observed in the transient absorption can be seen in the evolution of the lineshape in along the detection axis. Along the excitation axis, the vibronic structure of the electronic transition is visible, showing the effect of the underdamped bath mode on the absorption. For the case of  $S = 0.1$  this vibronic progression appears as a shoulder extending to higher excitation energies, while for the  $S = 1$  case a distinct progression of the bath mode is clear up to at least 3 quanta.

In addition to the static features of the lineshapes, there are noticeable dynamics in the center lines of the bands, illustrated more clearly in figures 7.5 and 7.6. The centerlines are clearly not linear with respect to the excitation axis over the entirety of the spectral band. This is because the approximations used in the derivation of the analytic equations for the center line slope in chapter 3 are not satisfied for the underdamped bath mode.[108]

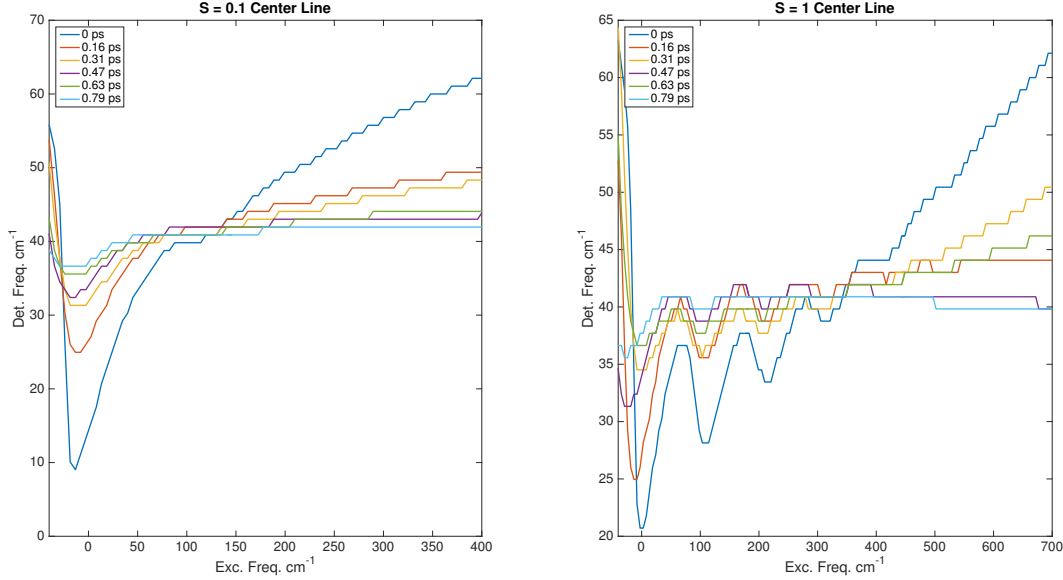


Figure 7.6: Center lines with respect to the excitation energy of the ground state band for a series of waiting times  $t_2$  for the excited state band of the correlated bath model with the same parameters as in figure 7.2. The excitation axis is referenced to the frequency of the zero-phonon transition and the detection axis is referenced to the frequency of the high frequency vibration on the ground electronic state, each prior to the renormalization by the bath.

Nevertheless, the results can still be used to gain a basic understanding of how the center line slope will behave. To first order, the center line slope with respect to the excitation frequency should be proportional to the correlation function describing the fluctuations induced by the correlated spectral density  $\mathcal{J}_{corr}(\omega)$ . This can be seen by the overall positive slope of the center line with respect to the excitation frequency at early times, which relaxes at  $t_2$  increases, with some small oscillations with respect to  $t_2$  noticeable in the case with the large Huang-Rhys factor.

The finer oscillatory structure with respect to the excitation frequency in the center lines is related to the vibronic progression of the underdamped mode, with, in this case, the positively sloped portions corresponding to the center lines for the individual vibronic transitions, with the negatively sloped portions coming in between. The differences in the slopes for each of the vibronic transitions observed in the  $S = 1$  case is caused by the differences in how strongly each of these transitions couples to the bath, showing that the degree of correlation decreases for the higher vibronic transitions. Interestingly, there also appears to be clear differences in how the center line behaves for the resolved vibronic bands, where it appears to be roughly linear, from the higher energy tail, where it is better described by a quadratic form for early  $t_2$ . In the absence of the vibronic transition (i.e.

$S = 0$ , not shown), the center lines fit reasonably well to a rational function of the form  $(a\omega_1^2 + b\omega_1 + c)/(\omega_1 + d)$ , considering only the main part of the band ( $\omega_1 \geq 0$ ). For the case of  $S = 0.1$ , the slope of the higher energy tail decays more quickly than that of the zero phonon band. This cannot be captured by the approximations used in chapter 3, and will require further theoretical analysis.

Other than the  $t_2$  dependent offset of the central frequency along the probe axis, which arises from the effective Stokes shift, the ground state bands show very similar dynamics in the center line, shown in figure 7.6. From this it is clear that the 2DEV spectra are capable of reporting on wavepacket dynamics through the center line, even when the transient IR absorption cannot. If there are differences in the spectral densities for the vibration on the ground and excited electronic states, such as discussed in chapter 3, these differences would manifest in different dynamics of the center lines for these bands. This might make it possible to separately track the vibrational evolution on the two electronic states, which in certain situations could be used to learn about the parameters of, for example, conical intersections.[51] In the case of anticorrelated fluctuations, the sign of all of these contributions, both of the center line slopes and of deviations of the central vibrational frequencies, will be reversed.

Due to the dependence of  $\mathcal{J}_{corr}(\omega)$  on the parameters for the electronic and vibrational degrees of freedom, it is straightforward to relate the effective Huang-Rhys factor which determines the magnitude of the oscillatory dynamics in the 2DEV spectra in terms of the usual parameters of the electronic and vibrational transition. Specifically, the effective Huang-Rhys factor will be given by

$$S_j^{eff} = \pm \gamma_c \sqrt{S_j \Delta_{vj}} \quad (7.14)$$

where  $\Delta_{vj} = \hbar^2/2$  is the anharmonic coupling between the mode being probed and the wavepacket coordinate and  $S_j = d_j^2/2$  is the usual Huang-Rhys factor for that mode. This potentially provides a method for directly measuring the anharmonic coupling between various vibrational modes in a system. It also means that it may require a very particular set of parameters for these effects to be significant.

These simple first modeling attempts are useful for understanding the spectral structures that are expected to arise when a wavepacket is excited in a simple bound, nearly harmonic potential. It is essentially consistent with the results observed in the dye DCM, which was determined to evolve along an overdamped wavepacket coordinate from the FC region to the charge separated state, as tracked by the shift in the frequency of a mode anharmonically coupled to the wavepacket coordinate.[127, 166] Many of the most interesting open questions involving small molecule photophysics involve the different mechanisms of fast reactive wavepackets, especially those which involve a conical intersection. Many studies have focused on attempting to unravel the detailed topology of conical intersections, but there are very few methods which can meaningfully report on the important properties, such as precisely identifying the important tuning and coupling vibrational coordinates. Even more so, it is very difficult to accurately measure the strengths of the nonadiabatic couplings which determine the overall shapes of the potential energy surfaces. Some proposals have been made

which utilize only structural information that can be inferred from techniques like 2DES and electronic linear absorption, but these still seem to require that the important modes have already been identified.[51] Because of the particularly direct and detailed manner in which 2DEV is capable of reporting on the coupling between the electronic and vibrational degrees of freedom of a molecule, it seems like a promising technique for learning about these details, which are otherwise difficult to access. It would be very interesting, then, to perform a systematic study of some simple conical intersection models with 2DEV, and to identify whether or not there are specific spectral signatures of the important parameters, such as identification of the coupling and tuning modes, how to distinguish these from unimportant spectator modes which happen to be coupled to the wavepacket coordinate, and whether or not the coupling parameters could be directly measured using this technique. Despite some early attempts at experimentally studying this type of system,[127, 126] this remains very much an open question, in need of systematic theoretical analysis.

### 7.3 Coherent Excitation Transfer

Other than the further development of 2DEV for the detailed study of small molecule photophysics, there are certain extensions which would be useful to perform to the understanding of its usefulness in studying excitation energy transfer in system like the photosynthetic light harvesting complexes. While we are certainly very interested in the possibility of using site specific vibrations as a tool for probing excitation energy transfer in these types of systems, it is clear that a number of limitations remain, both in its practical application as well as in our theoretical understanding.[107, 109]

The practical limitations are due to a long tradition of the method of indirect determination of these properties via the combination of electronic spectroscopies that operate in the excitonic basis and underdetermined modeling and the heavy development of this approach, while the tools necessary for the direct assignments we require are in their relative infancy. This is a major limitation, and it will likely require a substantial effort and investment of resources to develop the simulation techniques necessary for the fulfillment of the promise of using 2DEV for this purpose.

Specifically, we are in need of an accurate tool for predicting the vibrational frequencies of the chromophore and protein moieties on both the ground and excited electronic states, in the situation where the effects of the complex environment of the protein scaffold is of utmost importance. These tools are not completely undeveloped, as there has been a substantial effort by a number of groups into developing so-called ‘maps’ for how the vibrational frequencies of protein modes and experimentally important synthetic vibrational probes are shifted and how their lineshapes are affected by the specifics of the environment in the context of proteins.[27, 71, 31, 143] This research provides a crucial backbone to begin the specific extensions necessary for the analysis of the 2DEV site-specific mapping. It should be relatively straight-forward, though certainly non-trivial, to extend the approaches that have been used in these studies to the specific cases of the photosynthetic chromophores

embedded in the protein scaffold. So far, however, these tools have only been developed in the context of the electronic ground states, for obvious reasons. Electronic excited states are relatively unimportant in the study of protein structure and dynamics. The extension to include electronic excited states requires the consideration of nonequilibrium situations, which is inherently more complicated than equilibrium dynamics. It also necessitates the much greater expense of accurate excited state electronic structure calculations, which are still limited essentially to TD-DFT, and are plagued with numerous practical problems.

The overall result of these considerations is that the basic tools do not appear to be in place with the necessary accuracy for our needs. The most obvious approach would require expensive nonequilibrium QM:MM methods which are still a long way from being applicable to systems as complex as LHCII, for example. Until these tools have been further refined, it is difficult to imagine how the theoretical methods could be made to quickly catch up to the needs of the experimental tools we have developed. This problem will likely require a substantial amount of careful consideration and study, and it is not obvious what might be the most promising route.

A separate, perhaps less daunting missing theoretical piece is the extension of our highly simplified theoretical treatment of the dimer case to a more accurate dynamical model.[107] In our treatment we were concerned primarily with simplicity and ease of interpretation, so we made the standard approximations to the dimer system which make it possible to calculate closed forms for the response functions, but also neglect all of the energy transfer and other dynamical effects, which are precisely what we are actually interested in studying. We then had to reintroduce these dynamics during the waiting time  $t_2$  in an *ad hoc* manner where we assume a simple rate equation for population transfer that is equivalent to Redfield theory under the secular approximation. The result is an inconsistent calculation, where the lineshape functions and the population dynamics are calculated using different dynamical models, and therefore do not appropriately satisfy a number of important theoretical concepts, such as the fluctuation-dissipation theory that provides the link between these aspects of the spectroscopy.

There is an obvious way to improve on this first study, by implementing a 2DEV dimer model that can be solved using the exact quantum dynamics of by the Hierarchy Equations of Motion (HEOM) for both the electronic and vibrational degrees of freedom.[93, 91] This would allow for the extension of the model in several straight-forward ways, such as the consideration of a dynamical coherence between the electronic eigenstates, and the possibility of the type of oscillatory excitation dynamics which have been discussed many 2DES studies of photosynthetic light harvesting complexes.[103, 49, 88, 138, 133, 34, 132, 96, 168, 147, 62] Indeed, it is conceivable that this approach could make it clear how it might be possible for 2DEV to definitively answer the questions concerning the impact of these coherences on the excited state populations and the possibility of the significant role of nonsecular dynamics, where the coherences and populations directly and reversibly interchange.[132] Due to the limitations of the model we implemented to understand the structures that should appear in the 2DEV spectra of electronically couple systems, it remains an open question as to whether or not, and to what extent, this technique is suitable for answering these questions

about electronic coherences beyond the simple delocalization of the electronic eigenstates. Due to the apparent sensitivity of this technique to the electronic population as opposed to coherences, as evident from the major contributing Feynman diagrams, it seems possible that 2DEV might be able to help in determine the answer to some of the questions concerning the importance of the electronic coherences. The extension of the model and the use of the HEOM method in the calculation of the spectra and dynamics would be the clearest best method for continuing this inquiry.

Other than the questions concerning how electronic coherences might be expected to contribute to the 2DEV spectrum, it would also be very interesting to use a HEOM based model to study the potential usage of 2DEV in studying the questions of the role of discrete vibrations in these processes. A significant effort has recently been placed in understanding how to distinguish between electronic, vibrational and mixed coherences using 2DES.[26, 19, 62, 70, 60, 118] In a spectroscopic method like 2DES that only probes states addressable by electronic transitions, it is understandable that the role and precise assignments of vibrational and vibronic contributions could be rather complicated. By directly probing the vibrational transitions, 2DEV seems like a promising candidate for studying these phenomena. There are many questions, however, that must first be answered concerning how the different types of vibronic coherence might contribute to the spectrum, and would be the best way to identify them. There are at least two general categories of vibronic mixing that must be considered, the role of low frequency ( $\sim 10$ s -  $100$ s of  $\text{cm}^{-1}$ ) modes which cannot be directly excited with the IR transition, and that of the high frequencies that are addressable by 2DEV. Between these two situations, the low frequency case is probably of greater interest, as this appears to be more prevalent in light harvesting complexes, which often exhibit electronic energy gaps and oscillatory dynamics in the low  $100$ s of  $\text{cm}^{-1}$ . The hope in this case would be to use the 2DEV spectrum as a way of obtaining the information contained in the theoretical site probe response.[118]

The situation where high frequency modes ( $\simeq 1500 \text{ cm}^{-1}$ ) serving to strongly couple highly nondegenerate electronic states appears to be less prevalent in natural light harvesting complexes. It has, however, been suggested to play an important role in the electronic dynamics of the antenna complexes in certain cryptophyte algae.[96] While this situation is probably less prevalent than the case where the coupling is via a low frequency mode, it is also very unclear how it would contribute to the 2DEV spectra when the coupling mode is being directly probed. This is the type of situation where the model we developed for the simulation of the dimer 2DEV spectra would fail most dramatically, and so it is very difficult to know what to expect from the 2DEV calculated according to this model with accurate quantum dynamics. Due to some similarities with the role the coupling mode in the context of conical intersections, the study of these situations might become naturally interrelated, and could potentially allow 2DEV to become a standard method for studying nonadiabatic electronic dynamics.



# Bibliography

- [1] Julia Adolphs and Thomas Renger. “How Proteins Trigger Excitation Energy Transfer in the FMO Complex of Green Sulfur Bacteria”. In: *Biophysical Journal* 91.8 (Oct. 2006), pp. 2778–2797.
- [2] Ritesh Agarwal et al. “Ultrafast Energy Transfer in LHC-II Revealed by Three-Pulse Photon Echo Peak Shift Measurements”. In: *Journal of Physical Chemistry B* 104.13 (Apr. 2000), pp. 2908–2918.
- [3] Tae-Kyu Ahn et al. “Architecture of a charge-transfer state regulating light harvesting in a plant antenna protein.” In: *Science* 320.5877 (May 2008), pp. 794–797.
- [4] I. M. Alecu et al. “Computational thermochemistry: Scale factor databases and scale factors for vibrational frequencies obtained from electronic model chemistries”. In: *Journal of Chemical Theory and Computation* 6.9 (Sept. 2010), pp. 2872–2887.
- [5] Herbert van Amerongen, Leonas Valkunas, and Rienk van Grondelle. *Photosynthetic Excitons*. World Scientific, 2000.
- [6] Herbert van Amerongen et al. “Chapter 8. Structure and Function of Photosystem II Light-Harvesting Proteins (Lhcb) of Higher Plants”. In: *Primary Processes of Photosynthesis, Part 1*. Cambridge: Royal Society of Chemistry, 2007, pp. 329–367.
- [7] Jessica M Anna et al. “Two-Dimensional Electronic Spectroscopy Reveals Ultrafast Downhill Energy Transfer in Photosystem I Trimers of the Cyanobacterium *Thermosynechococcus Elongatus*”. In: *Journal of Physical Chemistry Letters* 3.24 (Dec. 2012), pp. 3677–3684.
- [8] Andreas Barth. “The infrared absorption of amino acid side chains”. In: *Progress in Biophysics and Molecular Biology* 74.3-5 (2000), pp. 141–173.
- [9] G. S. Beddard et al. “Internal conversion from vibrationally excited levels”. In: *Chemical Physics Letters* 18.4 (Feb. 1973), pp. 481–487.
- [10] Doran I G Bennett, Kapil Amarnath, and Graham R Fleming. “A Structure-Based Model of Energy Transfer Reveals the Principles of Light Harvesting in Photosystem II Supercomplexes”. In: *Journal of the American Chemical Society* 135.24 (June 2013), pp. 9164–9173.

- [11] Thomas Bittner et al. “Ultrafast Excitation-Energy Transfer and Exciton-Exciton Annihilation Processes in Isolated Light-Harvesting Complexes of Photosystem-II (Lhc-II) from Spinach”. In: *Journal of Physical Chemistry* 98.46 (Nov. 1994), pp. 11821–11826.
- [12] Robert E Blankenship. *Molecular Mechanisms of Photosynthesis*. Blackwell Publishing, 2002.
- [13] Oleksandr Isaienko Eric Borguet. “Pulse-front matching of ultrabroadband near-infrared noncollinear optical parametric amplified pulses”. In: *Journal of the Optical Society of America B* 26.5 (May 2009), pp. 965–972.
- [14] E. J. Bowen. “Fluorescence quenching in solution and in the vapour state”. In: *Transactions of the Faraday Society* 50 (1954), p. 97.
- [15] Jens Bredenbeck, Jan Helbing, and Peter Hamm. “Labeling Vibrations by Light: Ultrafast Transient 2D-IR Spectroscopy Tracks Vibrational Modes during Photoinduced Charge Transfer”. In: *Journal of the American Chemical Society* 126.4 (Jan. 2004), pp. 990–991.
- [16] William P Bricker et al. “Non-Radiative Relaxation of Photoexcited Chlorophylls: Theoretical and Experimental Study”. In: *Scientific Reports* 5 (Sept. 2015), p. 13625.
- [17] Tobias Brixner et al. “Phase-stabilized two-dimensional electronic spectroscopy”. In: *Journal of Chemical Physics* 121.9 (2004), p. 4221.
- [18] Tobias Brixner et al. “Two-dimensional spectroscopy of electronic couplings in photosynthesis”. In: *Nature* 434.7033 (Mar. 2005), pp. 625–628.
- [19] Vytautas Butkus, Leonas Valkunas, and Darius Abramavicius. “Vibronic phenomena and exciton-vibrational interference in two-dimensional spectra of molecular aggregates”. In: *Journal of Chemical Physics* 140.3 (Jan. 2014), p. 034306.
- [20] Vytautas Butkus et al. “Coherence and Population Dynamics of Chlorophyll Excitations in FCP Complex: Two-Dimensional Spectroscopy Study”. In: *Journal of Chemical Physics* 142.21 (June 2015), p. 212414.
- [21] Tessa R Calhoun et al. “Quantum Coherence Enabled Determination of the Energy Landscape in Light-Harvesting Complex II”. In: *Journal of Physical Chemistry B* 113.51 (Dec. 2009), pp. 16291–16295.
- [22] Justin R Caram, Andrew F Fidler, and Gregory S Engel. “Excited and ground state vibrational dynamics revealed by two-dimensional electronic spectroscopy”. In: *Journal of Chemical Physics* 137.2 (Jan. 2012), p. 024507.
- [23] Suryanarayanan Chandrasekaran et al. “Influence of Force Fields and Quantum Chemistry Approach on Spectral Densities of BChl a in Solution and in FMO Proteins”. In: *Journal of Physical Chemistry B* 119.31 (Aug. 2015), pp. 9995–10004.

- [24] Mary C Chang et al. "Spectroscopic characterization of the light-harvesting complex of *Rhodospirillum rubrum* and its structural subunit". In: *Biochemistry* 29.2 (May 2002), pp. 421–429.
- [25] Yuan-Chung Cheng and Graham R Fleming. "Dynamics of Light Harvesting in Photosynthesis". In: *Annual Review of Physical Chemistry* 60.1 (Mar. 2009), pp. 241–262.
- [26] Aurelia Chenu et al. "Enhancement of Vibronic and Ground-State Vibrational Coherences in 2D Spectra of Photosynthetic Complexes". In: *Scientific Reports* 3 (June 2013).
- [27] Minhaeng Cho. "Correlation between electronic and molecular structure distortions and vibrational properties. I. Adiabatic approximations". In: *Journal of Chemical Physics* 118.8 (Feb. 2003), pp. 3480–3490.
- [28] Minhaeng Cho. *Two-Dimensional Optical Spectroscopy*. CRC Press, 2009.
- [29] Minhaeng Cho. "Vibrational solvatochromism and electrochromism: Coarse-grained models and their relationships". In: *Journal of Chemical Physics* 130.9 (2009).
- [30] Minhaeng Cho et al. "Exciton Analysis in 2D Electronic Spectroscopy". In: *Journal of Physical Chemistry B* 109.21 (June 2005), pp. 10542–10556.
- [31] Jun Ho Choi and Minhaeng Cho. "Vibrational solvatochromism and electrochromism of infrared probe molecules containing  $C\equiv O$ ,  $C\equiv N$ ,  $C=O$ , or  $C-F$  vibrational chromophore". In: *Journal of Chemical Physics* 134.15 (2011).
- [32] Hoi Sung Chung et al. "Transient two-dimensional IR spectrometer for probing nanosecond temperature-jump kinetics". In: *Review of Scientific Instruments* 78.6 (2007), p. 063101.
- [33] Jeffrey A Cina and Philip A Kovac. "How Fissors Works: Observing Vibrationally Adiabatic Conformational Change through Femtosecond Stimulated Raman Spectroscopy". In: *Journal of Physical Chemistry A* 117.29 (July 2013), pp. 6084–6095.
- [34] Elisabetta Collini et al. "Coherently wired light-harvesting in photosynthetic marine algae at ambient temperature". In: *Nature* 463.7281 (Feb. 2010), pp. 644–647.
- [35] T M Cotton et al. "State of Chlorophyll a in vitro and in vivo from Electronic Transition Spectra, and the Nature of Antenna Chlorophyll". In: *Biochimica et Biophysica Acta (BBA) - Bioenergetics* 368.2 (Nov. 1974), pp. 181–198.
- [36] Therese M Cotton and Richard P Van Duyne. "Characterization of Bacteriochlorophyll Interactions in vitro by Resonance Raman Spectroscopy". In: *Journal of the American Chemical Society* 103.20 (Oct. 1981), pp. 6020–6026.
- [37] R Croce, S Weiss, and R Bassi. "Carotenoid-binding Sites of the Major Light-harvesting Complex II of Higher Plants". In: *Journal of Biological Chemistry* 274.42 (Oct. 1999), pp. 29613–29623.

- [38] Carles Curutchet and Benedetta Mennucci. “Quantum Chemical Studies of Light Harvesting”. In: *Chemical Reviews* (2016), acs.chemrev.5b00700.
- [39] Jahan M Dawlaty et al. “Mapping the spatial overlap of excitons in a photosynthetic complex via coherent nonlinear frequency generation”. In: *Journal of Chemical Physics* 135.4 (July 2011), p. 044201.
- [40] N Demirdöven et al. “Dispersion compensation with optical materials for compression of intense sub-100-fs mid-infrared pulses”. In: *Optics Letters* 27.6 (Jan. 2002), p. 433.
- [41] Mariangela Di Donato et al. “Cofactors Involved in Light-Driven Charge Separation in Photosystem I Identified by Subpicosecond Infrared Spectroscopy”. In: *Biochemistry* 50.4 (Feb. 2011), pp. 480–490.
- [42] Paul M Donaldson, Halina Strzalka, and Peter Hamm. “High sensitivity transient infrared spectroscopy: a UV/Visible transient grating spectrometer with a heterodyne detected infrared probe”. In: *Optics Express* 20.12 (June 2012), pp. 12761–12770.
- [43] Hui Dong et al. “Determining the static electronic and vibrational energy correlations via two-dimensional electronic-vibrational spectroscopy”. In: *Journal of Chemical Physics* 142.17 (May 2015), p. 174201.
- [44] Jakub Dostál et al. “2D Electronic Spectroscopy Reveals Excitonic Structure in the Baseplate of a Chlorosome”. In: *Journal of Physical Chemistry Letters* 5.10 (Apr. 2014), pp. 1743–1747.
- [45] Mei Du et al. “Direct Observation of Ultrafast Energy-Transfer Processes in Light Harvesting Complex II.” In: *Journal of Physical Chemistry* 98.17 (Apr. 1994), pp. 4736–4741.
- [46] Hong-Guang Duan et al. “Two-Dimensional Electronic Spectroscopy of Light-Harvesting Complex II at Ambient Temperature: A Joint Experimental and Theoretical Study”. In: *Journal of Physical Chemistry B* (Aug. 2015), pp. 12017–12027.
- [47] F Duschinsky. “On the Interpretation of Electronic Spectra of Polyatomic Molecules”. In: *Acta Physicochimica URSS* 7 (1937), pp. 551–566.
- [48] Daniel D. Eads et al. “Direct observation of energy transfer in a photosynthetic membrane: chlorophyll b to chlorophyll a transfer in LHC”. In: *The Journal of Physical Chemistry* 93.26 (Dec. 1989), pp. 8271–8275.
- [49] Gregory S Engel et al. “Evidence for wavelike energy transfer through quantum coherence in photosynthetic systems”. In: *Nature* 446.7137 (Apr. 2007), pp. 782–786.
- [50] Thomas A Evans and Joseph J Katz. “Evidence for 5- and 6-Coordinated Magnesium in Bacteriochlorophyll a from Visible Absorption Spectroscopy”. In: *Biochimica et Biophysica Acta (BBA) - Bioenergetics* 396.3 (Sept. 1975), pp. 414–426.
- [51] Marwa H. Farag, Thomas L. C. Jansen, and Jasper Knoester. “Probing the Interstate Coupling near a Conical Intersection by Optical Spectroscopy”. In: *Journal of Physical Chemistry Letters* (Aug. 2016), pp. 3328–3334.

- [52] M D Fayer. “Dynamics of Liquids, Molecules, and Proteins Measured with Ultrafast 2D IR Vibrational Echo Chemical Exchange Spectroscopy”. In: *Annual Review of Physical Chemistry* 60.1 (Mar. 2009), pp. 21–38.
- [53] Marco Ferretti et al. “The nature of coherences in the B820 bacteriochlorophyll dimer revealed by two-dimensional electronic spectroscopy ”. In: *Physical Chemistry Chemical Physics* 16.21 (2014), pp. 9930–9939.
- [54] Andrew F Fidler et al. “Probing Energy Transfer Events in the Light Harvesting Complex 2 (LH2) of Rhodobacter Sphaeroides with Two-Dimensional Spectroscopy”. In: *Journal of Chemical Physics* 139.15 (2013), p. 155101.
- [55] Harold N Fonda et al. “Normal-Mode Characteristics of Chlorophyll Models. Vibrational Analysis of Metallooctaethylchlorins and their Selectively Deuterated Analogs”. In: *Journal of the American Chemical Society* 112.26 (Dec. 1990), pp. 9497–9507.
- [56] Nicolas Forget, Vincent Crozatier, and Pierre Tournois. “Transmission Bragg-grating grisms for pulse compression”. In: *Applied Physics B* 109.1 (Oct. 2012), pp. 121–125.
- [57] Harry A Frank and Richard J Cogdell. “Carotenoids in Photosynthesis”. In: *Photochemistry and Photobiology* 63.3 (Mar. 1996), pp. 257–264.
- [58] Michael J Frisch et al. *Gaussian 09*. Gaussian Inc. Wallingford CT. 2009.
- [59] Marcel Fuciman et al. “The Role of Xanthophylls in Light-Harvesting in Green Plants: A Spectroscopic Investigation of Mutant LHCII and Lhcb Pigment-Proteins Complexes.” In: *Journal of Physical Chemistry B* 116.12 (2012), pp. 3834–49.
- [60] Yuta Fujihashi, Graham R Fleming, and Akihito Ishizaki. “Impact of environmentally induced fluctuations on quantum mechanically mixed electronic and vibrational pigment states in photosynthetic energy transfer and 2D electronic spectra”. In: *Journal of Chemical Physics* 142.21 (June 2015), p. 212403.
- [61] Masao Fujiwara and Mitsuo Tasumi. “Resonance Raman and Infrared Studies on Axial Coordination to Chlorophylls a and b in vitro”. In: *The Journal of Physical Chemistry* 90.2 (Jan. 1986), pp. 250–255.
- [62] Franklin D Fuller et al. “Vibronic coherence in oxygenic photosynthesis”. In: *Nature Chemistry* 6.8 (Aug. 2014), pp. 706–711.
- [63] N E Galanin, L A Yakubov, and G P Shaposhnikov. “Synthesis and spectral properties of sandwich meso-tetramethyltetrabenzoporphyrin-phthalocyanine complexes with lutetium, erbium, yttrium, and lanthanum”. In: *Russian Journal of Organic Chemistry* 44.6 (July 2008), pp. 921–926.
- [64] Sarah M Gallagher Faeder and David M Jonas. “Two-Dimensional Electronic Correlation and Relaxation Spectra: Theory and Model Calculations”. In: *Journal of Physical Chemistry A* 103.49 (Dec. 1999), pp. 10489–10505.

- [65] Naomi S Ginsberg, Yuan-Chung Cheng, and Graham R Fleming. “Two-Dimensional Electronic Spectroscopy of Molecular Aggregates”. In: *Accounts of Chemical Research* 42.9 (Aug. 2009), pp. 1352–1363.
- [66] Naomi S Ginsberg et al. “Solving structure in the CP29 light harvesting complex with polarization-phased 2D electronic spectroscopy”. In: *Proceedings of the National Academy of Sciences of the United States of America* 108.10 (Mar. 2011), pp. 3848–3853.
- [67] Rienk van Grondelle and Vladimir I. Novoderezhkin. “Energy transfer in photosynthesis: experimental insights and quantitative models”. In: *Physical Chemistry Chemical Physics* 8.7 (2006), pp. 793–807.
- [68] Marie Louise Groot et al. “Femtosecond Visible/Visible and Visible/Mid-IR Pump-Probe Study of the Photosystem II Core Antenna Complex CP47”. In: *Journal of Physical Chemistry B* 108.23 (June 2004), pp. 8001–8006.
- [69] Cesar A Guarin et al. “Dynamics of the Higher Lying Excited States of Cyanine Dyes. An Ultrafast Fluorescence Study”. In: *Journal of Physical Chemistry B* 117.24 (June 2013), pp. 7352–7362.
- [70] Alexei Halpin et al. “Two-dimensional spectroscopy of a molecular dimer unveils the effects of vibronic coupling on exciton coherences”. In: *Nature Chemistry* 6.3 (Mar. 2014), pp. 196–201.
- [71] Sihyun Ham et al. “Correlation between electronic and molecular structure distortions and vibrational properties. II. Amide I modes of NMA–nD<sub>2</sub>O complexes”. In: *Journal of Chemical Physics* 118.8 (Feb. 2003), pp. 3491–3498.
- [72] Peter Hamm. “Coherent effects in femtosecond infrared spectroscopy”. In: *Chemical Physics* 200.3 (1995), pp. 415–429.
- [73] Peter Hamm, Robert A Kaindl, and Jens Stenger. “Noise suppression in femtosecond mid-infrared light sources”. In: *Optics Letters* 25.24 (Jan. 2000), p. 1798.
- [74] Peter Hamm and Martin T Zanni. *Concepts and Methods of 2D Infrared Spectroscopy*. Cambridge University Press, Mar. 2011.
- [75] Peter Hamm et al. “The two-dimensional IR nonlinear spectroscopy of a cyclic pentapeptide in relation to its three-dimensional structure”. In: *Proceedings of the National Academy of Sciences of the United States of America* 96.5 (1999), pp. 2036–2041.
- [76] Michelle A Harris et al. “Integration of multiple chromophores with native photosynthetic antennas to enhance solar energy capture and delivery”. In: *Chemical Science* 4.10 (Aug. 2013), pp. 3924–3933.
- [77] Dugan Hayes and Gregory S Engel. “Extracting the Excitonic Hamiltonian of the Fenna-Matthews-Olson Complex Using Three-Dimensional Third-Order Electronic Spectroscopy”. In: *Biophysical Journal* 100.8 (Apr. 2011), pp. 2043–2052.

- [78] Dugan Hayes, Graham B Griffin, and Gregory S Engel. “Engineering coherence among excited states in synthetic heterodimer systems.” In: *Science* 340.6139 (June 2013), pp. 1431–1434.
- [79] Petra W. Hemelrijk et al. “Spectroscopic properties of LHC-II, the main light-harvesting chlorophyll a/b protein complex from chloroplast membranes”. In: *BBA - Bioenergetics* 1098.2 (Jan. 1992), pp. 159–166.
- [80] Richard W Hendler and Richard I Shrager. “Deconvolutions based on singular value decomposition and the pseudoinverse: a guide for beginners”. In: *Journal of Biochemical and Biophysical Methods* 28.1 (Jan. 1994), pp. 1–33.
- [81] Gerhard Herzberg. *Molecular Spectra and Molecular Structure*. Electronic Spectra and Electronic Structure of Polyatomic Molecules. D. Van Nostrand Company Inc., 1966.
- [82] Masahiro Higashi et al. “Theoretical study on excited states of bacteriochlorophyll a in solutions with density functional assessment”. In: *Journal of Physical Chemistry B* 118.37 (Sept. 2014), pp. 10906–10918.
- [83] Peter Hildebrandt and Thomas G Spiro. “Surface-Enhanced Resonance Raman Spectroscopy of Copper Chlorophyllin on Silver and Gold Colloids”. In: *The Journal of Physical Chemistry* 92.12 (June 1988), pp. 3355–3360.
- [84] David P. Hoffman and Richard A. Mathies. “Femtosecond Stimulated Raman Exposes the Role of Vibrational Coherence in Condensed-Phase Photoreactivity”. In: *Accounts of Chemical Research* 49.4 (Apr. 2016), pp. 616–625.
- [85] Nancy E Holt et al. “Carotenoid cation formation and the regulation of photosynthetic light harvesting.” In: *Science* 307.5708 (Jan. 2005), pp. 433–436.
- [86] William Humphrey, Andrew Dalke, and Klaus Schulten. “VMD – Visual Molecular Dynamics”. In: *Journal of Molecular Graphics* 14 (1996), pp. 33–38.
- [87] John D Hybl, Allison Albrecht Ferro, and David M Jonas. “Two-dimensional Fourier transform electronic spectroscopy”. In: *Journal of Chemical Physics* 115.14 (2001), p. 6606.
- [88] A Ishizaki and G R Fleming. “Theoretical examination of quantum coherence in a photosynthetic system at physiological temperature”. In: *Proceedings of the National Academy of Sciences of the United States of America* 106.41 (Oct. 2009), pp. 17255–17260.
- [89] Akihito Ishizaki and Graham R Fleming. “On the adequacy of the Redfield equation and related approaches to the study of quantum dynamics in electronic energy transfer”. In: *Journal of Chemical Physics* 130.23 (2009), p. 234110.
- [90] Akihito Ishizaki and Graham R Fleming. “Quantum Coherence in Photosynthetic Light Harvesting”. In: *Annual Review of Condensed Matter Physics* 3.1 (Feb. 2012), pp. 333–361.

- [91] Akihito Ishizaki and Graham R Fleming. “Unified treatment of quantum coherent and incoherent hopping dynamics in electronic energy transfer: Reduced hierarchy equation approach”. In: *Journal of Chemical Physics* 130.23 (Jan. 2009), p. 234111.
- [92] Akihito Ishizaki and Yoshitaka Tanimura. “Dynamics of a multimode system coupled to multiple heat baths probed by two-dimensional infrared spectroscopy”. In: *Journal of Physical Chemistry A* 111.38 (2007), pp. 9269–9276.
- [93] Akihito Ishizaki and Yoshitaka Tanimura. “Modeling vibrational dephasing and energy relaxation of intramolecular anharmonic modes for multidimensional infrared spectroscopies”. In: *Journal of Chemical Physics* 125.8 (Aug. 2006), p. 084501.
- [94] David M Jonas et al. “Pump-Probe Polarization Anisotropy Study of Femtosecond Energy Transfer within the Photosynthetic Reaction Center of Rhodospirillum rubrum R26”. In: *The Journal of Physical Chemistry* 100.30 (Jan. 1996), pp. 12660–12673.
- [95] M Khalil, N Demirdoven, and A Tokmakoff. “Coherent 2D IR Spectroscopy: Molecular Structure and Dynamics in Solution”. In: *Journal of Physical Chemistry A* 107.27 (July 2003), pp. 5258–5279.
- [96] Avinash Kolli et al. “The fundamental role of quantized vibrations in coherent light harvesting by cryptophyte algae”. In: *Journal of Chemical Physics* 137.17 (Nov. 2012), p. 174109.
- [97] Werner Kuhlbrandt, Da Neng Wang, and Yoshinori Fujiyoshi. “Atomic model of plant light-harvesting complex by electron crystallography”. In: *Nature* 367.6464 (Feb. 1994), pp. 614–621.
- [98] Philipp Kukura, David W McCamant, and Richard A Mathies. “Femtosecond Stimulated Raman Spectroscopy”. In: *Annual Review of Physical Chemistry* 58.1 (May 2007), pp. 461–488.
- [99] Kijeong Kwac and Minhaeng Cho. “Two-Color Pump-Probe Spectroscopies of Two- and Three-Level Systems: 2-Dimensional Line Shapes and Solvation Dynamics”. In: *Journal of Physical Chemistry A* 107.31 (July 2003), pp. 5903–5912.
- [100] Kyungwon Kwak, Daniel E Rosenfeld, and M D Fayer. “Taking apart the two-dimensional infrared vibrational echo spectra: More information and elimination of distortions”. In: *Journal of Chemical Physics* 128.20 (2008), p. 204505.
- [101] Kyungwon Kwak et al. “Frequency-frequency correlation functions and apodization in two-dimensional infrared vibrational echo spectroscopy: A new approach”. In: *Journal of Chemical Physics* 127.12 (2007), p. 124503.
- [102] Joseph R Lakowicz. *Principles of Fluorescence Spectroscopy*. Third. Springer, 2006.
- [103] Hohjai Lee, Yuan-Chung Cheng, and Graham R Fleming. “Coherence dynamics in photosynthesis: Protein protection of excitonic coherence”. In: *Science* 316.5830 (2007), pp. 1462–1465.



- [104] A Leggett et al. “Dynamics of the dissipative two-state system”. In: *Review of Modern Physics* 59.1 (Jan. 1987), pp. 1–85.
- [105] P G Lepage. “A new algorithm for adaptive multidimensional integration”. In: *Journal of Computational Physics* 27.2 (May 1978), pp. 192–203.
- [106] Nicholas H. C. Lewis and Graham R. Fleming. “Two-Dimensional Electronic-Vibrational Spectroscopy of Chlorophyll a and b”. In: *Journal of Physical Chemistry Letters* (2016), pp. 831–837.
- [107] Nicholas H C Lewis et al. “A Method for the Direct Measurement of Electronic Site Populations in a Molecular Aggregate using Two-Dimensional Electronic-Vibrational Spectroscopy”. In: *Journal of Chemical Physics* 143.12 (Sept. 2015), p. 124203.
- [108] Nicholas H C Lewis et al. “Measuring Correlated Electronic and Vibrational Spectral Dynamics using Line Shapes in Two-Dimensional Electronic-Vibrational Spectroscopy”. In: *Journal of Chemical Physics* 142.17 (May 2015), p. 174202.
- [109] Nicholas H. C. Lewis et al. “Observation of Electronic Excitation Transfer Through Light Harvesting Complex II Using Two-Dimensional Electronic-Vibrational Spectroscopy”. In: *Journal of Physical Chemistry Letters* (Oct. 2016), pp. 4197–4206.
- [110] Hebin Li et al. “Pulse Propagation Effects in Optical 2D Fourier-Transform Spectroscopy: Experiment”. In: *Journal of Physical Chemistry A* 117.29 (July 2013), pp. 6279–6287.
- [111] Pen Nan Liao et al. “Correlation of Car  $S_1 \rightarrow$  Chl with Chl  $\rightarrow$  Car  $S_1$  energy transfer supports the excitonic model in quenched light harvesting complex II”. In: *Journal of Physical Chemistry B* 114.47 (2010), pp. 15650–15655.
- [112] Y-S Lin et al. “On the Calculation of Rotational Anisotropy Decay, as Measured by Ultrafast Polarization-Resolved Vibrational Pump-Probe Experiments”. In: *Journal of Chemical Physics* 132.17 (2010), p. 174505.
- [113] Zhenfeng Liu et al. “Crystal structure of spinach major light-harvesting complex at 2.72 Å resolution.” In: *Nature* 428.6980 (2004), pp. 287–292.
- [114] Marc Lutz. “Resonance Raman Studies in Photosynthesis”. In: *Advances in Infrared and Raman Spectroscopy* 11 (1984). Ed. by R J H Clark and R E Hester, pp. 211–300.
- [115] Michael S Lynch et al. “Coherent Fifth-Order Visible–Infrared Spectroscopies: Ultrafast Nonequilibrium Vibrational Dynamics in Solution”. In: *Journal of Physical Chemistry A* 116.26 (July 2012), pp. 7023–7032.
- [116] Alexander Matro and Jeffrey A Cina. “Theoretical Study of Time-Resolved Fluorescence Anisotropy from Coupled Chromophore Pairs”. In: *Journal of Physical Chemistry* 99.9 (Mar. 1995), pp. 2568–2582.
- [117] F Milota et al. “Two-dimensional electronic spectroscopy of molecular excitons”. In: *Accounts of Chemical Research* 42.9 (2009), pp. 1364–1374.

- [118] Daniele M. Monahan et al. "Influence of weak vibrational-electronic couplings on 2D electronic spectra and inter-site coherence in weakly coupled photosynthetic complexes". In: *Journal of Chemical Physics* 143.6 (Aug. 2015), p. 65101.
- [119] G Mourou and M M Malley. "Molecular orientational relaxation times in liquids". In: *Optics Communications* 13.4 (Apr. 1975), pp. 412–417.
- [120] Shaul Mukamel. *Principles of Nonlinear Optical Spectroscopy*. Oxford University Press, 1995.
- [121] Robert S. Mulliken. "Iodine Revisited". In: *Journal of Chemical Physics* 55.288 (1971), p. 288.
- [122] Jeffrey A Myers et al. "Two-color two-dimensional Fourier transform electronic spectroscopy with a pulse-shaper". In: *Optics Express* 16.22 (2008), p. 17420.
- [123] Abraham Nitzan. *Chemical Dynamics in Condensed Phases*. Relaxation, Transfer, and Reactions in Condensed Molecular Systems. Oxford University Press, June 2006.
- [124] Vladimir I. Novoderezhkin, Alessandro Marin, and Rienk van Grondelle. "Intra- and inter-monomeric transfers in the light harvesting LHCII complex: the Redfield-Forster picture". In: *Physical Chemistry Chemical Physics* 13.38 (Sept. 2011), p. 17093.
- [125] T. Oksenhendler et al. "Self-referenced spectral interferometry". In: *Applied Physics B: Lasers and Optics* 99.1-2 (Apr. 2010), pp. 7–12.
- [126] Thomas A A Oliver and Graham R Fleming. "On the Role of Conical Intersections in the Ultrafast Relaxation of  $\beta$ -apo-8'-carotenal". In: *Journal of Physical Chemistry B* 119 (July 2015), pp. 11428–11441.
- [127] Thomas A A Oliver, Nicholas H C Lewis, and Graham R Fleming. "Correlating the motion of electrons and nuclei with two-dimensional electronic-vibrational spectroscopy". In: *Proceedings of the National Academy of Sciences of the United States of America* 111.28 (June 2014). also see corrections on Page 16628, pp. 10061–10066.
- [128] Evgeny E Ostroumov et al. "Broadband 2D Electronic Spectroscopy Reveals a Carotenoid Dark State in Purple Bacteria". In: *Science* 340.6128 (Apr. 2013), pp. 52–56.
- [129] Evgeny E Ostroumov et al. "Energy Transfer Pathways in Light-Harvesting Complexes of Purple Bacteria as Revealed by Global Kinetic Analysis of Two-Dimensional Transient Spectra". In: *Journal of Physical Chemistry B* 117.38 (Sept. 2013), pp. 11349–11362.
- [130] Atsuhiko Osuka and Kazuhiro Maruyama. "Synthesis of naphthalene-bridged porphyrin dimers and their orientation-dependent exciton coupling". In: *Journal of the American Chemical Society* 110.13 (June 1988), pp. 4454–4456.
- [131] Yoonsoo Pang et al. "Excited-State Dynamics of 8'-Apo- $\beta$ -caroten-8'-al and 7',7'-Dicyano-7'-apo- $\beta$ -carotene Studied by Femtosecond Time-Resolved Infrared Spectroscopy". In: *Journal of Physical Chemistry B* 113.39 (Sept. 2009), pp. 13086–13095.

- [132] Gitt Panitchayangkoon et al. “Direct evidence of quantum transport in photosynthetic light-harvesting complexes”. In: *Proceedings of the National Academy of Sciences of the United States of America* 108.52 (Dec. 2011), pp. 20908–20912.
- [133] Gitt Panitchayangkoon et al. “Long-lived quantum coherence in photosynthetic complexes at physiological temperature”. In: *Proceedings of the National Academy of Sciences of the United States of America* 107.29 (July 2010), pp. 12766–12770.
- [134] Eun Sun Park et al. “Vibrational Stark Spectroscopy in Proteins: A Probe and Calibration for Electrostatic Fields”. In: *Journal of Physical Chemistry B* 103.45 (Nov. 1999), pp. 9813–9817.
- [135] Sean A Passino et al. “Three-Pulse Echo Peak Shift Studies of Polar Solvation Dynamics”. In: *Journal of Physical Chemistry A* 101.4 (Jan. 1997), pp. 725–731.
- [136] Jorg Pieper et al. “Chromophore-chromophore and chromophore-protein interactions in monomeric light-harvesting complex II of green plants studied by spectral hole burning and fluorescence line narrowing”. In: *Journal of Physical Chemistry B* 113.31 (Aug. 2009), pp. 10870–10880.
- [137] A Piryatinski and J L Skinner. “Determining Vibrational Solvation-Correlation Functions from Three-Pulse Infrared Photon Echoes”. In: *Journal of Physical Chemistry B* 106.33 (July 2002), pp. 8055–8063.
- [138] Patrick Rebentrost et al. “Environment-assisted quantum transport”. In: *New Journal of Physics* 11.3 (Mar. 2009), p. 033003.
- [139] A G Redfield. “On the theory of relaxation processes”. In: *IBM Journal of Research and Development* 1 (1957), p. 19.
- [140] A G Redfield. “The Theory of Relaxation Processes”. In: *Advances in Magnetic and Optical Resonance* 1 (1965), pp. 1–32.
- [141] Jeffrey R Reimers et al. “Assignment of the Q-Bands of the Chlorophylls: Coherence Loss via Qx - Qy Mixing”. In: *Scientific Reports* 3 (Sept. 2013), p. 2761.
- [142] R. Remelli et al. “Chlorophyll Binding to Monomeric Light-harvesting Complex: A MUTATION ANALYSIS OF CHROMOPHORE-BINDING RESIDUES”. In: *Journal of Biological Chemistry* 274.47 (1999), pp. 33510–33521.
- [143] Mike Reppert and Andrei Tokmakoff. “Computational Amide I 2D IR Spectroscopy as a Probe of Protein Structure and Dynamics”. In: *Annual Review of Physical Chemistry* 67.1 (May 2016), pp. 359–386.
- [144] Gerhard Ritschel et al. “An efficient method to calculate excitation energy transfer in light-harvesting systems: Application to the Fenna-Matthews-Olson complex”. In: *New Journal of Physics* 13.11 (Nov. 2011), p. 113034.
- [145] Sean T Roberts, Joseph J Loparo, and Andrei Tokmakoff. “Characterization of spectral diffusion from two-dimensional line shapes”. In: *Journal of Chemical Physics* 125.8 (Aug. 2006), p. 084502.

- [146] Jan Roden et al. “Accounting for intra-molecular vibrational modes in open quantum system description of molecular systems”. In: *Journal of Chemical Physics* 137.20 (Nov. 2012), p. 204110.
- [147] Elisabet Romero et al. “Quantum coherence in photosynthesis for efficient solar-energy conversion”. In: *Nature Physics* 10.9 (Sept. 2014), pp. 676–682.
- [148] Alexander V. Ruban et al. “Identification of a mechanism of photoprotective energy dissipation in higher plants”. In: *Nature* 450.7169 (Nov. 2007), pp. 575–578.
- [149] Gabriela S Schlau-Cohen et al. “Pathways of Energy Flow in LHCII from Two-Dimensional Electronic Spectroscopy”. In: *Journal of Physical Chemistry B* 113.46 (Oct. 2009), pp. 15352–15363.
- [150] Gabriela S Schlau-Cohen et al. “Single-Molecule Identification of Quenched and Unquenched States of LHCII”. In: *Journal of Physical Chemistry Letters* 6.5 (Mar. 2015), pp. 860–867.
- [151] Gabriela S Schlau-Cohen et al. “Spectroscopic elucidation of uncoupled transition energies in the major photosynthetic light-harvesting complex, LHCII.” In: *Proceedings of the National Academy of Sciences of the United States of America* 107.30 (July 2010), pp. 13276–13281.
- [152] Gregory D Scholes et al. “Lessons from nature about solar light harvesting”. In: *Nature Chemistry* 3.10 (Oct. 2011), pp. 763–774.
- [153] Yihan Shao et al. “Advances in Molecular Quantum Chemistry Contained in the Q-Chem 4 Program Package”. In: *Molecular Physics* 113.2 (Dec. 2014), pp. 184–215.
- [154] Sang-Hee Shim and Martin T Zanni. “How to turn your pump-probe instrument into a multidimensional spectrometer: 2D IR and Vis spectroscopies via pulse shaping”. In: *Physical Chemistry Chemical Physics* 11.5 (Jan. 2009), p. 748.
- [155] Sangwoo Shim et al. “Atomistic Study of the Long-Lived Quantum Coherences in the Fenna-Matthews-Olson Complex”. In: *Biophysical Journal* 102.3 (Feb. 2012), pp. 649–660.
- [156] Akira Shirakawa, Isao Sakane, and Takayoshi Kobayashi. “Pulse-front-matched optical parametric amplification for sub-10-fs pulse generation tunable in the visible and near infrared”. In: *Optics Letters* 23.16 (Jan. 1998), p. 1292.
- [157] Richard I Shrager and Richard W Hendler. “Titration of individual components in a mixture with resolution of difference spectra, pKs, and redox transitions”. In: *Analytical Chemistry* 54.7 (June 1982), pp. 1147–1152.
- [158] G S Singhal and E Rabinowitch. “Measurement of the Fluorescence Lifetime of Chlorophyll a In Vivo”. In: *Biophysical Journal* 9.4 (Apr. 1969), pp. 586–591.

- [159] Aaron Sisto, David R Glowacki, and Todd J Martínez. “Ab Initio Nonadiabatic Dynamics of Multichromophore Complexes: A Scalable Graphical-Processing-Unit-Accelerated Exciton Framework”. In: *Accounts of Chemical Research* 47.9 (Sept. 2014), pp. 2857–2866.
- [160] Gerald J Small. “Herzberg–Teller Vibronic Coupling and the Duschinsky Effect”. In: *Journal of Chemical Physics* 54.8 (Sept. 2003), pp. 3300–3306.
- [161] Andreas D Stahl et al. “A Femtosecond Visible/Visible and Visible/Mid-Infrared Transient Absorption Study of the Light Harvesting Complex II”. In: *Biophysical Journal* 97.12 (Dec. 2009), pp. 3215–3223.
- [162] Ivo H M van Stokkum, Delmar S Larsen, and Rienk van Grondelle. “Global and target analysis of time-resolved spectra”. In: *BBA-Bioenergetics* 1657.2-3 (July 2004), pp. 82–104.
- [163] Alberto Suarez, Robert Silbey, and Irwin Oppenheim. “Memory effects in the relaxation of quantum open systems”. In: *Journal of Chemical Physics* 97.7 (Oct. 1992), pp. 5101–5107.
- [164] Yoshitaka Tanimura. “Stochastic Liouville, Langevin, Fokker–Planck, and Master Equation Approaches to Quantum Dissipative Systems”. In: *Journal of the Physical Society of Japan* 75.8 (Aug. 2006), p. 082001.
- [165] Yuichi Terazono et al. “Multiporphyrin Arrays with  $\pi$ – $\pi$  Interchromophore Interactions”. In: *Journal of the American Chemical Society* 137.1 (Dec. 2014), pp. 245–258.
- [166] Francesca Terenziani and Anna Painelli. “Two-dimensional electronic-vibrational spectra: modeling correlated electronic and nuclear motion”. In: *Physical Chemistry Chemical Physics* 17 (Apr. 2015), p. 1374.
- [167] Carsten Tietz et al. “Single molecule spectroscopy on the light-harvesting complex II of higher plants.” In: *Biophysical journal* 81.1 (2001), pp. 556–562.
- [168] V Tiwari, W K Peters, and D M Jonas. “Electronic resonance with anticorrelated pigment vibrations drives photosynthetic energy transfer outside the adiabatic framework”. In: *Proceedings of the National Academy of Sciences* 110.4 (Jan. 2013), pp. 1203–1208.
- [169] Aaron J. Van Tassle. “Excited State Structural Dynamics of Carotenoids and Charge Transfer Systems”. PhD thesis. University of California, Berkeley, 2006.
- [170] Aaron J. Van Tassle, Matthew A. Prantil, and Graham R. Fleming. “Investigation of the excited state structure of DCM via ultrafast electronic pump/vibrational probe”. In: *Journal of Physical Chemistry B* 110.38 (Sept. 2006), pp. 18989–18995.
- [171] F. Verluise et al. “Amplitude and phase control of ultrashort pulses by use of an acousto-optic programmable dispersive filter: pulse compression and shaping”. In: *Optics Letters* 25.8 (Apr. 2000), p. 575.

- [172] Peter J. Walla et al. “Two-Photon Excitation Spectrum of Light-Harvesting Complex II and Fluorescence Upconversion after One- and Two-Photon Excitation of the Carotenoids”. In: *Journal of Physical Chemistry B* 19 (May 2000), pp. 4799–4806.
- [173] William R Ware and Colin Lewis. “Wavelength Effects in Fluorescence Quenching. Aromatic Hydrocarbons Quenched by Carbon Tetrachloride”. In: *Journal of Chemical Physics* 57.8 (Oct. 1972), pp. 3546–3557.
- [174] Luuk J G W van Wilderen, Craig N Lincoln, and Jasper J van Thor. “Modelling Multi-Pulse Population Dynamics from Ultrafast Spectroscopy”. In: *PLOS ONE* 6.3 (Mar. 2011), e17373.
- [175] S Woutersen et al. “Hydrogen-Bond Lifetime Measured by Time-Resolved 2D-IR Spectroscopy: N-Methylacetamide in Methanol”. In: *Chemical Physics* 266.2-3 (May 2001), pp. 137–147.
- [176] Sunney Xie et al. “Femtosecond fluorescence depolarization study of photosynthetic antenna proteins: observation of ultrafast energy transfer in trimeric C-phycocyanin and allophycocyanin”. In: *Proceedings SPIE* 1640 (1992), pp. 690–706.
- [177] Wei Xiong et al. “Automated 2D IR spectrometer mitigates the influence of high optical densities”. In: *Vibrational Spectroscopy* 50.1 (May 2009), pp. 136–142.
- [178] Mino Yang and Graham R Fleming. “Third-order nonlinear optical response of energy transfer systems”. In: *Journal of Chemical Physics* 111.1 (July 1999), pp. 27–39.
- [179] Mino Yang, Kaoru Ohta, and Graham R Fleming. “Three-pulse photon echoes for model reactive systems”. In: *Journal of Chemical Physics* 110.21 (June 1999), pp. 10243–10252.
- [180] Michael K Yetzbacher et al. “Propagation, beam geometry, and detection distortions of peak shapes in two-dimensional Fourier transform spectra”. In: *Journal of Chemical Physics* 126.4 (2007), p. 044511.
- [181] Zhengyang Zhang et al. “Phase-cycling schemes for pump–probe beam geometry two-dimensional electronic spectroscopy”. In: *Chemical Physics Letters* 550 (Oct. 2012), pp. 156–161.
- [182] Junrong Zheng et al. “Ultrafast Dynamics of Solute-Solvent Complexation Observed at Thermal Equilibrium in Real Time.” In: *Science* 309.5739 (Aug. 2005), pp. 1338–1343.
- [183] F Zhu, C Galli, and R M Hochstrasser. “The real-time intramolecular electronic excitation transfer dynamics of 9',9-bifluorene and 2',2-binaphthyl in solution”. In: *Journal of Chemical Physics* 98.2 (Jan. 1993), pp. 1042–1057.